Compression Behavior of Smectitic vs. Illitic Mudrocks

by

Chunwei Ge

Bachelor of Engineering, University of Minnesota - Twin Cites (2012)
Master of Science, Massachusetts Institute of Technology (2016)

Submitted to the Department of Civil and Environmental Engineering
in partial fulfillment of the requirements for the degree of

Doctor of Philosophy in the field of Geotechnical and Geoenvironmental Engineering

at the

MASSACHUSETTS INSTITUTE OF TECHNOLOGY

February 2019

Author .....
Department of Civil and Environmental Engineering
September 14, 2018

Certified by .....
John T. Germaine
Research Professor, Tufts University
Thesis Supervisor

Accepted by .....
Heidi Nepf
Donald and Martha Harleman Professor of Civil and Environmental Engineering
Chair, Graduate Program Committee

Compression Behavior of Smectitic vs. Illitic Mudrocks

by

Chunwei Ge

Submitted to the Department of Civil and Environmental Engineering
on September 14, 2018, in partial fulfillment of the
requirements for the degree of
Doctor of Philosophy in the field of Geotechnical and Geoenvironmental Engineering

Abstract

Overpressure or fluid pressure in excess of hydrostatic pressure has been observed globally in many deep water sedimentary basins. One of the possible mechanisms for overpressure is the smectite-to-illite (S-I) transformation. During the transformation, the basal spacing of the smectite layer reduces. The interlayer water is released into pore space, causing an increase in pore pressure.

This thesis investigates the compression and permeability behavior change due to S-I transformation. Uniaxial compression testing was performed on smectitic and illitic mudrocks. The original Gulf of Mexico - Eugene Island (GoM-EI) mudrock sets the baseline for smectitic mudrock in order to compare with illitic mudrocks. Two methods were used to create illitic mudrock from the GoM-EI sediment. The illitic mudrock A was cooked in a high temperature constant rate of strain (CRS) device with effective stress applied (200 °C and 30 days); the illitic mudrock B was cooked in a hydrothermal cooker in a slurry state (250 °C and 18 days). The multi-functional high temperature CRS device was designed from scratch to tackle the challenge of measuring the mechanical properties of a mudrock and transforming the clay minerals.

Although the methods of inducing S-I transformation are different, similar degrees of illitization for the illitic mudrock A and B was achieved by selecting the right temperature and time combination. The mineral transformation does not greatly alter the compressibility of the mudrocks. However, both the illitic mudrock A and B sit higher in porosity space than the smectitic mudrock at low stress level. As effective stress increases, the illitic mudrock A converges with the smectitic mudrock, while the illitic mudrock B reverses order with the smectitic mudrock at 30 MPa. The permeability of the smectitic mudrock ranges over five orders from 10^{-16} to 10^{-20} m^2 from a porosity of 0.58 to 0.23. The permeability of the mudrocks are greatly increased by the mineral transformation. The permeability ratio of the illitic mudrocks over the smectitic mudrock increases from 2 to 12 as porosity decreases.

The creep rate (C_α) at room temperature and elevated temperature were measured during the transformation stage of the illitic mudrock A. C_α at elevated temperature increases by 50 % compared with that at room temperature. The increase in rate is

caused by mineral transformation. Using the difference in rate, a model is proposed to estimate the effective stress reduction or overpressure generation based on the degree of mineral transformation.

Thesis Supervisor: John T. Germaine
Title: Research Professor, Tufts University

Acknowledgments

There are a lot people I would like to thank.

I am extremely grateful to Dr.G. I appreciate the amount of time and energy he spent explaining thing in theory and fixing technical problem with me. The skills and knowledge learned from him and the entire research group will always be the valuable treasure for me. I would like to thank Professor Peter Flemings for teaching me the presentation skills and selling my research as a business pitch.

I would express my gratitude to Dr. Day-Stirrat from Shell for helping me analyzing mudrock samples and providing direction for how to conduct hydrothermal tests. Steve Rudolph for helping me with designing and fabricating the equipment.

I would like to gratefully acknowledge my other teachers of geotechnical engineering; Professor Herbert H. Einstein, and Professor Andrew J. Whittle. They have taught me a great amount of knowledge about geologic and geotechnical stuff.

I am sincerely thankful for my friends: Amanda, Bing, Hao, Omar, Mark, and Deniz. This list can go on and on, nevertheless, I would like to express my gratitude to the people who I met, who had shared experience with me at MIT. I would carry all the happy memory and game on.

THIS PAGE INTENTIONALLY LEFT BLANK

Contents

1 Introduction **19**

1.1 Problem Statement 19

1.2 Thesis Objectives and Scope 19

1.3 Organization of the Thesis 20

2 Background **23**

2.1 Introduction 23

2.2 Overpressure in the Gulf of Mexico Block 330 25

2.2.1 I/S Profile along A20-ST Well in the Gulf of Mexico Block 330 25

2.3 Stress Reduction due to Overpressure 27

2.4 Transformation Mechanism 27

2.4.1 Time Factor 28

2.5 Previous Experimental Study on Mineral Transformation 30

2.6 Effects of Mineral Transformation on Compression and Permeability Behavior 32

2.6.1 Mechanical Compression 32

2.6.2 Chemical Compression 33

2.6.3 Permeability Change Caused by Diagenesis 34

2.7 Texture and Fabric Study of Diagenetic Clay Minerals 35

2.8 Time Dependent Behavior— Creep or Secondary Consolidation . . . 37

2.8.1 The Time Effect 38

2.8.2 The Temperature Effect 38

2.8.3 The Stress Level Effect 39

2.8.4 Quasi-preconsolidation Effect 39

3 Test Materials **63**

3.1 Geological Setting 63

3.2 The mineralogy of the original GoM-EI source material 64

3.3 Leaching Process 67

3.4 Resedimentation Process 68

3.4.1 Mixing KCl Salt Solution 69

3.4.2 Salt Crystallization During Resedimentation 70

4 Methodology and Equipment **75**

4.1 Methodology for Comparing Material Behavior Change due to Mineral Transformation 76

4.2 Design Requirements for High Temperature CRS System 77

4.3 The High Temperature CRS Device 77

4.3.1 Temperature Control System 80

4.3.2 Load Frame and Hydraulic System 80

4.3.3 Control System and Data Acquisition System 81

4.3.4 Equipment Evaluation and Calibration 82

4.4 Hydrothermal Reactor 84

4.5 Equipment for Measuring SSA 84

5 Control Algorithm and Data Analysis for CRS Tests **93**

5.1 Control Algorithm 94

5.2 Data Analysis 96

5.2.1 Constant Rate of Strain Method 96

5.2.2 Controlled Gradient Consolidation Method 96

5.3 Reduction Code for Analyzing the Data 97

5.4 Symbol List 97

6 Results and Interpretation **105**

6.1 The Smectitic Mudrock 106

6.2 The K- saturated Smectitic Mudrock vs. the Na- saturated GoM-EI . 108
6.3 The Effect of Smectite-to-illite Transformation 109
6.3.1 Permeability Behavior Change 110
6.3.2 Compression Behavior Change 112
6.3.3 Mineral Composition 115
6.3.4 Specific Surface Area 117
6.3.5 Observation based on Fabric Analysis 118
6.4 Secondary Compression Evaluation 120
6.4.1 Secondary Compression of Protocol A 120

7 Overpressure Model **139**
7.1 Introduction 139
7.2 Components of Mudrock Transformation 139
7.3 Model Formulation 140
7.3.1 Free Draining System 140
7.3.2 Constant Volume System 142
7.3.3 Undrained System 143
7.4 Evaluation of Free Draining Case 144
7.4.1 Theoretical Released Bound Water 144
7.4.2 Analysis of Lab Test 145
7.5 Evaluation of Overpressure Cases 148

8 Conclusions and Recommendations **159**
8.1 Key Observations and Developments 159
8.2 Modeling the Impact of Illitization 161
8.3 Recommendations for Future Work 162

References **165**

A KCl Salt Mixing Guide **169**

B Reduction File **171**

THIS PAGE INTENTIONALLY LEFT BLANK

List of Figures

2-1 Generalized Overpressure Profile in Sedimentary Basins 41
2-2 Generalized Illite Profile vs Temperature 41
2-3 Location of Origin GoM-EI Source Material 42
2-4 Profile View of Well A-20ST and Well A-12 42
2-5 Pore Pressure Map of the Block 330 43
2-6 Vertical Effective Stress Contour Map of Block 330 44
2-7 Illite % in I/S Phase Increases as a Function of Depth in the Gulf of Mexico. 44
2-8 Illite Ratio of Well A-20ST 45
2-9 Modelled Temperature History at the A Fault Depth of Well A-20ST 45
2-10 Stress Reduction Due to Overpressure 46
2-11 Two Modes of Bulk Density vs. Effective Stress 46
2-12 Solid State Transformation: Illite Growth by Layer Addition 47
2-13 Dissolution and Precipitation Model of Smectite to Illite Transformation 48
2-14 Illite Ratio vs. Temperature. 49
2-15 Favored Reaction Conditions for Generating Illite 49
2-16 Test conditions for Comparing Chemical Compression and Mechanical Compression. 50
2-17 Interlayer Water inside smectite 51
2-18 Compression Curves for Smectite, illite and kaolinite 51
2-19 Compression Curves for Smectite, kaolinite, and smectite kaolinite mixture 52
2-20 Porosity Reduction Rate vs. Vertical Effective Stress 53

2-21 Fitted Compression Curve Accounting for Different Temperatures at Gulf of Mexico . . . 54
2-22 Fibrous Illite in Sandstone . . . 55
2-23 Three Basic Morphologies for Illite . . . 55
2-24 The Clay Layers (N) in a McEwan Structure increase with I in I/S% 56
2-25 Preferred Orientation of Clay Particles . . . 56
2-26 The Effect of Mineral Transformation on Preferred Orientation . . . 57
2-27 Void Ratio vs. Log Time for 1D Incremental Loading Test . . . 58
2-28 The Slopes of C_α and C_c in the compression Curve . . . 58
2-29 $C_{\alpha\eta}$ increases with time . . . 59
2-30 C_α as a function of stress level . . . 60
2-31 C_α vs. Vertical Effective Stress . . . 61
2-32 Secondary Compression Induced Quasi-preconsolidation Effect . . . 62

3-1 The Bath Water Conductivity Reading during the Leaching Process of GoM-EI . . . 72
3-2 Comparison of Compression Behavior between Intact Lab Samples and Resedimentation GoM-EI Specimens and Field Logs . . . 72
3-3 Basic Stages in Preparing Resedimentation Batch . . . 73
3-4 Crystallization of KCl Salt with $3mol/L$ pore fluid during Resedimentation with Acrylic Tubes . . . 74
3-5 Comparison of Salt Crystal Formation on PVC and Acrylic Tubes . . . 74

4-1 Experimental Procedures for Comparative Tests . . . 86
4-2 The High Temperature CRS Device Components . . . 86
4-3 Cross Section of the High Temperature Device . . . 87
4-4 Schematic Diagram for Temperature Control System . . . 87
4-5 Load Frame for 100 MPa CRS Devices . . . 88
4-6 Thermal Set of the O-ring . . . 88
4-7 Net Load vs. Piston Displacement . . . 89
4-8 Apparatus Compressibility Curve . . . 89

4-9 Cracked Porous Stone 90
4-10 Hydrothermal Reactor 90
4-11 Cross Section of Seal for Hydrothermal Reactor 91
4-12 Equipment for Measuring Total SSA 91
4-13 Aluminum Tares with Mixture of EGME and Clay 92

5-1 Combined Control Method Data from TCRS006 99
5-2 Strain Rate Changes with Control Method 100
5-3 Flow Chart of Vertical Load Control Algorithm 101
5-4 Results from CRS Test using a Cycle of Constant Load to Reduce Pore Pressure 102
5-5 Permeability Result from CRS1370 by Fahy (2014) 103

6-1 Summary of Hydrothermal Reaction Result from Author's Master Thesis. 123
6-2 Strain Rate for Smectitic Mudrock 123
6-3 Compression Curve for the Smectitic Mudrock 124
6-4 Permeability Data for the Smectitic Mudrock. The permeability line displays good linearity in n - $log(\sigma_v^{'}$ space. 125
6-5 Compression Curve for the K-Smectitic Mudrock and Na-Smectitic Mudrock (Fahy, 2014). 126
6-6 Permeability curve for the K-Smectitic Mudrock and Na-Smectitic Mudrock (Fahy, 2014). 127
6-7 Permeability Curve Comparison 127
6-8 Ratio of Permeability. r_k is the ratio of permeability of the illitic mudrock B over permeability of the smectitic mudrock. 128
6-9 Permeabilities of smectite, illite and kaolinite clay minerals (adapted from Mesri and Olson 1971) 128
6-10 Coefficient of Consolidation Comparison 129
6-11 Compression Curve for Illitic Mudrock A 129

6-12 Strain Energy Method to Determine the Preconsolidation Stress for Illitic Mudrock A. The $\sigma_p^{'}$ is determined to be 16 MPa. 130
6-13 Compression Curve Comparison for the Smectitic Mudrock and Illitic Mudrocks. 130
6-14 Compression Curve Comparison for the Smectitic Mudrock and Illitic Mudrocks from 10 to 100 MPa. 131
6-15 Compressibility Comparison for the Smectitic Mudrock and Illitic Mudrocks. 131
6-16 Compressibility Comparison Zoom In 132
6-17 Compressibility in Stress Space 132
6-18 Compressibility in Stress Space Zoom In 133
6-19 Mineral Composition of the three Mudrocks 133
6-20 SEM Images for the Smectitic Mudrock and Illitic Mudrock B at around 90 MPa and a Porosity of 0.21. The magnification is 100kx. 134
6-21 Illustration for the Smectite-to-illite Transformation (after Bowers 2011) 135
6-22 SEM Images for the Illitic Mudrock A and B. 136
6-23 Void Ratio Drop at Stage 2 & 3 due to Creep and Mineral Transformation. 137
6-24 Creep at Room Temperature. The zero time is from the time when excess pore pressure measured at the base of the high temperature CRS cell is zero. 137
6-25 Creep at Elevated Temperature. The zero time is from the time when the temperature of the high temperature CRS device starts to increase. 138
6-26 $C_{\alpha n}$ Value in This Study vs. Data from Karig et al. (2003) 138

7-1 General Model of Overpressure 151
7-2 The Compression Behavior of a mudrock going through S-I transition for a Free Draining System 152
7-3 The Proposed Overpressure Model for an Undrained System 152
7-4 Explanation for Volume Expansion Due to bound Water Release . . . 153

7-5 The D-spacing Change of the Smectite 154
7-6 Procedures for Calculating Void Ratios for Blue Dot and Red Dot . . 154
7-7 Schematics for Void Ratio Calculation 155
7-8 Overpressure Model: Porosity vs. Stress 155
7-9 Porosity vs. Overpressure Ratio with Different Degree of Illitization . 156
7-10 Overpressure Ratio vs. Rp with Different Degree of Illitization when $n = 0.388$. 156
7-11 Overpressure Ratio vs. C_{sn} to C_{cn} Ratio with Different Degree of Illitization at 5 MPa effective stress 157

THIS PAGE INTENTIONALLY LEFT BLANK

List of Tables

2.1 Kinetic Model of Mineral Reaction 29
2.2 Porosity Reduction in Test 7 and Test 8 32

3.1 Bulk Composition of Original GoM-EI 65
3.2 Mineral Composition of Clay Fraction ($< 2\mu m$) of Original GoM-EI . 66

4.1 Tensile Strength of Different Stainless Steel 79
4.2 Properties of Different O-rings 79

6.1 Reaction Conditions for Illitic Mudrocks 110
6.2 Summary of Smectitic vs. Illitic Tests 115
6.3 Mineral Composition for the Clay Fraction 116
6.4 SSA of GoM-EI with different Cations (Unit: m^2/g) 118
6.5 Summary of Total SSA 118

7.1 Summary Table 147

A.1 KCl Potatssium Chloride Solution Mixing Guide 169

THIS PAGE INTENTIONALLY LEFT BLANK

Chapter 1

Introduction

1.1 Problem Statement

In early 1960s, researcher found that the percentage of illite increases with depth in Gulf of Mexico basin due to smectite-to-illite (S-I) transformation. The ratio of illite to smectite is indicative of temperature and pressure condition in the basin. This ratio is used for oil reservoir characterization and overpressure prediction. During the transformation, the basal spacing of the smectite layer reduces. The interlayer water is released into pore space, causing an increase in pore pressure. Although there have been numerous studies on the mineralogical aspect of smectite-to-illite transformation, the mechanical effects of the clay transition are not fully understood. The goal of my research is to study the permeability, compressibility change due to mineral transformation, as well as to propose a model to estimate the overpressure generation based on the degree of mineral transformation.

1.2 Thesis Objectives and Scope

This thesis is the phase two of my research. Phase one study investigates the reaction conditions for smectite-to-illite transformation such as temperature, time and KCl concentration (Ge, 2016). Phase one study provides valuable knowledge of the kinetics of the reaction. Difference combinations of temperature and time were tested on the

Gulf of Mexico-Eugene Island (GoM-EI) mudrock using hydrothermal cooker. Phase one study also develops solid analytic method to characterize mineral composition for transformed GoM-EI material using x-ray diffraction (XRD).

Phase two study presented in this thesis has three main objectives.

The first objective is to develop a multi-functional high temperature CRS device to measure the mechanical properties of a mudrock up to 100 MPa and to transform the clay minerals with effective stress. The second objective of the research is to compare the compressibility and permeability change of a mudrock due to the mineral transformation. The third objective is to develop a model to estimate the effective stress reduction or overpressure generation based on the degree of mineral transformation.

This research is part of the UT Geofluids Consortium, a collaboration between Tufts University (formerly MIT) and UT Austin. This consortium provides a wide breadth of data on different mudrocks all around the world, with the focus on "evolution of pressure, stress, deformation and fluid migration through experiment, models and field study".

1.3 Organization of the Thesis

This thesis is organized into seven chapters and numerous appendices. The main chapters provide reader with entire investigation process from background, literature review to equipment design, data analysis process, and finally summary of result and interpretation. The appendices provide more detailed laboratory procedures, data sheets, and computer codes.

Chapter 2 provides a background summary of the smectite-to-illite transformation mechanism in the natural environment and the theoretical explanation for how this reaction causes overpressure. This chapter studies Gulf of Mexico Block 330 as an example for the overpressured basin. Extensive investigation into the literature is performed to validate the novelty of this research. Detail summary of effects of mineral transformation on compression and permeability behavior is given, followed

by a concise review of creep behavior of the mudrock.

Chapter 3 provides the geological information of the material used for the research as well as information about the material processing. Information about the geological setting, in situ temperature, mineralogy, pore pressure and vertical effective stress are recorded. This chapter also covers the leaching process, salt mixing procedures and resedimentation process.

Chapter 4 describes the method and equipment used in the research to measure the mudrock behavior change. Two different methods are used to induce the illitization. A detail description of control system for automating the tests is given. The method and equipment used for measuring the specific surface area is also provided.

Chapter 5 presents a solution for controlling the excess pore pressure when compressing a high plasticity specimen in a uniaxial compression test. The control algorithm switches from constant rate strain in stage I to constant pore pressure in stage II when pore pressure reaches certain value. This chapter also presents corresponding equations and theories for analyzing data collected in stage I and stage II.

Chapter 6 summarizes the experimental results. A comparison on the compression behavior, compressiblity and permeability between the smectitic mudrock and the illtic mudrocks are discussed. The creep rate in room temperature and elevated temperature is shown. The difference in open system and closed system for the stress reduction model is presented. Clay fabric analysis is done using the SEM images of the smectitic mudrock and the illitic mudrocks.

Chapter 7 is a summary of main results of this research. Recommendations for future work are provided as well.

THIS PAGE INTENTIONALLY LEFT BLANK

Chapter 2

Background

Nomenclature

This background section contains considerable amount of terminologies in the clay mineralogy and geology which is unfamiliar to most Civil Engineers. Readers should refer to Moore and Reynolds (1989) and Chapter 3 in Ge (2016). The specific definitions needs to be well-acquainted are: smectite, illite, mix-layered mineral, I/S and Reichweite ordering, fundamental particles, and MacEwan crystallite and fundamental particles. Geologists prefer terminologies like compaction and creep, whereas civil engineers more frequently use compression and secondary compression.

2.1 Introduction

Overpressure or fluid pressure in excess of hydrostatic pressure has been observed globally in different sedimentary basins. Tectonic stress, rapid deposition of low permeability sediments and clay mineral diagenesis are recognized as potential contributors to overpressure generation. In the petroleum industry, knowledge of the distribution of overpressure is critical in geophysical interpretation and deep borehole design. Figure 2-1a summarizes three examples of the overpressured profile (Nadeau, 2005)(P. Nadeau, 2005). The Basin A pore pressure profile is similar to that of the Gulf of Mexico, where the overpressure ramps at the shallowest depth starting at 2 km. Basin C is similar to Norwegian continental shelf, the overpressure kicks in at a

deeper stratum around 5 km. Although the pressure ramps start at different depths, they share the same temperature vs. pore pressure relation (Figure 2-1b). Pore pressure follows the hydrostatic line at low temperature, starts to ramp up from 80 °C to 120 °C, and almost reaches the lithostatic line when temperature is greater than 120 °C.

Nadeau (2005) observed the connection between the smectite-to-illite transformation and overpressure generation. The illitization vs. temperature relationship (Figure 2-2) coincides with the pore pressure vs. temperature relationship. The illite% ($I\%$) in the mixed-layer mineral (I/S) starts to increase from 60-80 °C, slowly ramps up from 80 °C to 120 °C, and increases at a sharp slope to unity when temperature is greater than 120 °C.

Studies by Lahann (2002) and Bowers also emphasize the connection between clay mineral diagenesis and overpressure. Bowers (2011) believes that density of interlayer water is denser than the pore water , when the interlayer water is released to pore space during the smectite-to-illite transformation, the volume of interlayer water expands. In a closed system or low permeability condition, the pore pressure will increase dramatically due to clay mineral diagenesis.

Studies by Osborne and Swarbrick (2001) and Hart et al. (1995) investigated the relationship between compaction disequilibrium and overpressure. If the sedimentation rate is slow, normal compaction occurs; this normal compaction generates hydrostatic pore pressure in the formation. If the sediments are unable to expel or partially expel their pore fluids in response to a rapid sedimentation rate or due to low permeability, compaction disequilibrium occurs. The remained fluid in the pores of the sediments must support all or part of the overburden, causing pore pressure to increase. It is observed in Gulf of Mexico that sediment′s permeability is low enough to significantly cause overpressure.

Both mechanisms, mineral transformation and compaction disequilibrium, are the major contributor to the overpressure generation, but there is no actual measured data to confirm the theory, this motives the current research to study the relationship between overpressure generation and smectite-to-illite transformation.

2.2 Overpressure in the Gulf of Mexico Block 330

Block 330 in the Gulf of Mexico provides a perfect case study for researchers to study an overpressurized basin. It is located off the coast of Louisiana shown in Figure 2-3. The geological environment in Block 330 was well studied and documented by Losh et al. (1999) and Hart et al. (1995). It was a major scientific endeavor to study and understand the geologic, chemical, and thermal conditions of a major growth fault (also termed the A fault in Figure 2-3 and Figure 2-4). The source material for this research is cored from well A-20ST and A-12. The properties of the source material are discussed in Chapter 3.

Losh et al. (1999) mapped the pore pressure for the cross section of Block 330 shown in Figure 2-5. Pore pressure profile is generated using fluid pressure measurements in the sand layers from over 30 borings. He observed that the entire basin is severely overpressured. In the upthrown side, the upper 1.5 km are hydrostatically pressured, followed by a moderately overpressured transition zone from 1.5 km to 2 km, and then severe overpressures, equaling up to 95% of the total lithostatic pressure occurring below 2 km. The pore pressure profiles differ significantly across the fault. The overpressure is much lower on the downthrown side than the upthrown side. In the downthrown side, the offset between the pore pressure measurement and hydrostatic line is about 2 MPa.

Figure 2-6 shows the vertical effective stress contour map. The effective stress is also generated based on the pore pressure map of the cross section. The upthrown side has significant reduction in vertical effective stress due to overpressure. Along the A fault, the effective stress can be as low as 1.1 MPa. The position of A20-ST well is illustrated in Figure 2-6.

2.2.1 I/S Profile along A20-ST Well in the Gulf of Mexico Block 330

Observed by numerous researchers, the illite percentage (I%) in the I/S increases with depth in sedimentary environment (Perry and Hower, 1970; Bethke and Altaner 1986,

Hower et al., 1976). Lahann et al.'s (2002) and Hower et al.'s (1976) data show very similar trend. Mineral transformation profile in Figure 2-7 is a typical clay diagenesis profile for the Gulf of Mexico Basin. From 1300 to 7600 ft, I% in I/S is below 50%; from 7600 to 11400 ft, the ratio increases to 68%; in the deeper section, the ratio increases and stops at 80 %. In the Gulf of Mexico, the depletion of potassium source is the major reason that prevents the ratio from approaching unity.

Following the discussion of overpressure in the Gulf of Mexico Block 330, the illitization profile in the well A20-ST (Figure 2-4) provides valuable data for understanding the mineral transformation process. Losh et al. (1999) found that the ratio is unusually high for Pliocene-Pleistocene sediments at 2.3 km burial depth. Similar high ratio is observed at shallower depth and lower temperature in A-20ST. I/(I+S) %, total layers of illite over the sum of total layers of smectite and illite ratio, increases with depth (Figure 2-8). The I/(I+S)% is calculated by

$$I/(I+S)\% = \frac{illite\% + (I\,in\,I/S) \times I/S\%}{illite\% + I/S\% + smectite\%} \tag{2.1}$$

If using Nadeau's (2005) generalized illite profile vs. temperature relation (Figure 2-2), with a in-situ temperature of 70 °C, there should be only negligible illite in the well. The measured I/(I+S) % is around 50 % at the fault depth. The reason for high illite content is not totally understood. There are two factors contributing to the illitilization: 1. high potassium content in the brine; 2. thermal pulse at a higher temperature than the ambient temperature in the present day.

Losh et al. (1999) claimed that K^+ exchange for Na^+ in smectite during early diagenesis leads to a potassium-enriched smectite. This K^+-smectite may transform to illite at a lower temperature. In addition, he also conducted thermal history modeling of the fault zone using information obtained from studying organic matter maturity. He found that the in situ temperature in the fault zone is around 70 °C, and an abnormal thermal pulse or thermal flow at 125 °C occurred for a period of 2500 years (Figure 2-9). The elevated temperature is believed to be the cause of higher degree of illitization.

2.3 Stress Reduction due to Overpressure

Lahann et al. (2002) studied an overpressurized well B in the Gulf of Mexico to investigate the effect of mineral transformation and compaction disequilibrium on overpressure generation . The illite profile vs. depth is shown in Figure 2-7.

Lahann et al. (2002) generated the crossplot of density vs. effective stress for the same well (Figure 2-10). The bulk density of shale is estimated from density logs, and effective stress from sonic logs. Under normal pressure conditions (no overpressure, <3600 ft), the effective stress increases monotonically with depth, and the sediments continually consolidate, the bulk density continually increases to a depth of 7600ft (the blue dots). Slight overpressure pore fluid is trapped by the low permeability of mudrock in the initial stage of illitization (the pink dots, 7600 - 11400 ft). Under the condition of compaction disequilibrium (7600 - 11400 ft), and when I in I/S is below 45%, the sediments continue to load with illitization; When I in I/S is greater than 45%, the sediments starts to unload with increasing degree of illitization, the density keeps constant with reduction of effective stress. Lahann et al. (2002) argued that with combination of undercompaction (low permeability) and higher degree of illitization that the shale starts to unload.

Lahann et al. (2002) further explained that there are two bulk density and stress relationships derived from illitic mudstone (Figure 2-11). In a closed system, the permeability of deep sediments are so low that the fluid is not able to drain, then the pore pressure builds up. The effective stress reduces dramatically while the density remains constant (isovolume). While in a open system, where fluid is able to drain, the density would increase at constant stress, which behaves similar to material undergoes secondary compression (isostress).

2.4 Transformation Mechanism

This section discusses the origin and creation of illite in a diagenetic environment. The knowledge of detrital illite is covered by Betard et al. (2009) and Meunier &

Velde (2013) in great detail.

The smectite-to-illite reaction pathway follows three stages in a shallow burial diagenesis environment like Gulf of Mexico. The transformation starts when the temperature is around 60-80 °C and reacts up to 120-140 °C. The first stage is a highly smectitic clay represented by randomly ordered I/S phase (R0). With increasing reaction, randomly ordered I/S are transformed into regularly interstratified structures (R≥1). The third stage is that the ordered I/S reacts to a final discrete illite.

In a micro scale, two models for illitization are particularly important: 1. layer by layer transformation or solid state transformation (Hower et al., 1976); 2. neoformation mechanism (Nadeau et al., 1985; Boles & Franks, 1979) .

Layer-by-layer transformation is the remodeling of a smectite 2:1 structure. The fixation of K^+ in the interlayer space leads to a non-reversible collapse of d-spacing from 15 Å (2 water layers smectite) to 10 Å (illite). As illitization progresses, the number of fundamental particles (N) increases with addition of illite or smectite layers. Figure 2-12 illustrates the process in which additional layers attach to a McEwan structure. (Boles & Franks, 1979). This solid state transformation theory was supported by Ferrage et al.(2011)'s study using X-ray Diffraction (XRD) method.

In Figure 2-13, Nadeau et al. (1985) further explains the origin of the additional illite layers. These layers are a result of dissolution-precipitation reactions under the condition of high K^+ concentration in the pore fluid. Firstly, smectite dissolves in the pore fluid, thin illite precipitates and adds to I/S lattice creating a larger crystal. With increasing degree of transformation, thin illite also dissolves in solution and precipitates as larger illite crystallites.

2.4.1 Time Factor

Boles and Franks (1979), Ferrage et al. (2011), Pytte and Reynolds (1989) and Ge (2016) have discovered that the smectite-to-illite transformation is temperature driven rather than depth or stress driven. The reaction rate increases with temperature. With ample supply of potassium, the reaction progresses much faster.

In addition to temperature and potassium concentration in the pore fluid, time is

another important element in the reaction.

One way to determine the age of illite is by the K-Ar dating method (Pevear, 1992). The K^+ cation, which is fixed in the interlayer space during transformation, is used to determine the age of illite. To get an accurate measurement of the diagenetic age, researchers need to differentiate source of the illite. In a sedimentary basin, illite are mostly formed diagenetically in a low temperature environment (< 150 °C), but illite derived from the host rocks as a weathering product are formed in a much higher temperature. The neoformed I/S or neoformed illite records the thermal history of a sediment, but detrital illite age does not reflect the age of the sedimentary basin.

A more robust way to estimate the age is to study the kinetic model. Huang (1993) and Pytte and Reynolds (1989) used equation 2.2 to study the diagenetic age.

$$\frac{-dS}{dt} = A \cdot exp(\frac{-E_a}{RT})[K^+]S^2 \tag{2.2}$$

where S is the smectite percentage in the I/S, t is time,A is the frequency factor, E_a is the activation energy, R is the gas constant, T is the temperature and $[K^+]$ is the potassium concentration.

In table 2.1, for three carefully studied shales in the Gulf of Mexico (Pytte and Reynolds, 1989), the time required to reach 80 % illite in I/S varies from 300 million years to 1 million years depending on the temperature. The K^+ concentration used is the average oil field brine, about 100-200 ppm or 0.1-0.2 g/L.

To summarize, in its natural condition, the reaction rate of a diagenetic illite is extremely slow.

Table 2.1: Kinetic Model of Mineral Reaction

Input			Output
I % in I/S	Temp. °C	K^+(ppm)	Time (my)
80	70	100-200	300
80	100	100-200	10
80	127	100-200	1

2.5 Previous Experimental Study on Mineral Transformation

In order to have better understanding of the smectite-to-illite transformation, numerous researchers conducted hydrothermal tests to reproduce the reaction in a laboratory environment (Huang et al., 1993; Ferrage et al., 2011; Eberl, 1980; Montoya & Hemley, 1975).

Hydrothermal reactions were conducted in high temperature and high potassium concentration to accelerate the transformation, so that the reaction could be completed in a reasonable time scale, due to the fact that diagenetic illite takes millions of years to form in low temperature and low potassium concentration environment. Ferrage et al. (2011) elevated the temperature range to 200-400 $°C$. Figure 2-14 summarizes data from Ferrage et al. (2011) and Ge (2016) for different combinations of time and temperature. Data from Ge (2016) are in the upper left box. Data from Ferrage et al. (2011) are in the lower right box. The source material for Ge is the Gulf of Mexico-Eugene (GoM-EI) mudrock, which has a I/(I+S)% ratio of 42 %. The source material for Ferrage is pure smectite. In the most extreme case, 400 $°C$ and 120 days, for a pure smectite starting material, the I/(I+S)% ratio increases to 82 %. The I/(I+S)% of GoM-EI increases by 50% in 18 days at 300 °C, while pure smectite only gained 32% in 30 days at the same temperature. The I/S phase in the GoM-EI provides a template for illite to grow and catalyze the reaction.

Montoya and Hemley (1975) studied the formation of illite from a different perspective. They investigated the thermal stability of illite within a system whose starting material is composed of K-feldspar, mica and silica. A phase diagram is generated using the data from thermal stability tests for K_2O-Al_2O_2-SiO_2-H_2O system (Figure 2-15). Illite forms under the conditions of high temperature and K^+ concentration. However, the cooking temperature should not be over 600 $°C$, otherwise the system is not favorable to form illite, but rather forms other type of minerals or simply bakes pottery.

The hydrothermal tests have not considered the effect of interparticle stress in the

progress of mineral transformation. These hydrothermally altered clay minerals are cooked in a slurry state with no effective stress, but mudrocks that undergo diagenetic reaction in the sedimentary basin are under vertical effective stress. To study the mineral transformation of a mudrock sample under more realistic condition, Duffy (2012) cooked the cored sample from North Sea Basin in a triaxial cell to simulated the in-situ stress field and temperature.

Duffy (2011)'s test procedures involved three stages: 1. consolidate the intact sample to a target vertical effective stress of 30 MPa; 2. keep the vertical effective stress constant for 300 hours. 3. increase vertical effective stress to 50 MPa and hold stress for another 300 hours. Figure 2-16 displays the axial pressure, radial pressure, p ore pressure and temperature for a heated test (test 7) and a room temperature test (test 8). The samples for test 7 and test 8 are hydrostatically consolidated in identical procedures except for the test temperature and pore fluid chemistry. Test 7 is heated to 150 °C while test 8 is conducted at 25 °C. The pore fluid chemistry is 3 mol/L KCl solution for test 7, and 3 mol/L NaCl solution for test 8.

Duffy compared the porosity reduction at the hold stress stage between test 7 at high temperature and test 8 with no heating (Table 2.2). At 30 MPa vertical effective stress (stage 2), the porosity reduction for a duration of 300 hours increased from 9% (test 8) to 19% (test 7). Then she increased the stress level to 50 MPa vertical effective stress (stage 3). The porosity reduction increases from 17% (test 8) to 27% (test 7). The porosity reduction increase is caused by combination effect of temperature effect and K^+-exchange. From XRD analysis, the heated sample of test 7 shows no sign of illitization but only cation exchange. This suggests the reaction rate at 150 °C is not fast enough to see mineral change in 25 days, but a higher reaction temperature challenges the performance of sealing material in the triaxial cell. In short summary, her tests failed to induce diagenetic reaction, but confirmed that at higher temperature, the creep rate increases; porosity of the hotter mudrock is of lower value.

Duffy expressed the difficulty of conducting mineral transformation tests with effective stress at higher temperature. Fitts and Brown's (1999) experimental design

Table 2.2: Porosity Reduction in Test 7 and Test 8

	Temperature, °C	Pore Fluid	Porosity Reduction, %	
			at 30 Mpa	at 50MPa
Test 7	150	3M KCl	19	27
Test 8	25	3M NaCl	9	17

avoided this challenge by studying the relationship between dehydration of smectite and overpressure generation. Using a modified 1D consolidometer, they found dehydration starts at 1.3 MPa effective stress and the three-water-layer smectite releases one interlayer water as effective stress increases (Figure 2-17). Smectite can take in water as zero, single, double or triple layers of water. Single, double, triple layers correspond to a d-spacing of around 12.5Å, 15.4Å, and 18.5Å respectively for sodium saturated smectite. According to Colten-Bradley (1987), three-water-layer smectite only exists at shallow depth. As depth increases, three-water-layer smectite becomes two-water-layer smectite, and is stable between 50 to 75 °C depth zone.

2.6 Effects of Mineral Transformation on Compression and Permeability Behavior

Compaction (geology term) or compression (geotechnical term) is both a function of stress, temperature and time.

Mechanical compression is a function of effective stress. The void ratio or porosity of a sediment reduces with increasing effective stress or depth of burial. Mechanical compression is dominant over chemical compression with in the low temperature zone ($<$ 80-100 °C). At higher temperatures, chemical compression becomes dominant (Goulty et al., 2016).

2.6.1 Mechanical Compression

Mechanical and chemical compression occur simultaneously in a diagenetic basin. It is difficult to investigate chemical compression in the laboratory due to the low kinetics.

Meade (1966, 1963) conducted 1D compression tests on reactant minerals —smectite and product mineral—illite individually to see the change in compression behavior due to mineral transformation. .

Meade(1966) found at any given effective stress, the porosity of smectite (montmorillonite in the figure), illite and kaolinite are in descending order (Figure 2-18). Mondol et al. (2007) conducted uniaxial compression tests on a mixture of smectite and kaolinite clay minerals. Figure 2-19 shows the same trend that pure smectite has the highest porosity, pure kaolinite the lowest. Meade's also calculated the compressibility, the relationship of three minerals over a stress level from 0.01 to 100 MPa are: smectite $>$ illite $>$ kaolinite, at all stress range.

However, Mondol et al. (2007)'s result does not totally agree with Meade (1966)'s. Mondal et al. (2007) used kaolinite instead of illite, because illite is the intermediate mineral in terms of compression behavior change, kaolinite provides more drastic differences in compressibility. He argues that the compressibility hierarchy of smectite and kaolinite has three stages. Only at low stress level ($<$1 MPa) and transition stage ($<$ 5 MPa) is Meade's statement valid. At higher stress level, the pure smectite is less compressible than pure kaolinite. In Figure 2-20 stage 1 and 2, the porosity reduction rate of 100% smectite is higher than 100% kaolinite. In stage 3 the higher stress level, the order reverses.

2.6.2 Chemical Compression

Chemical compression includes mineral transformation, clay mineral dissolution and precipitation, quartz dissolution and precipitation, and framework weakening due to temperature increase. In general, deeper, hotter mudrocks are more compressed at a given effective stress due to chemical compression.

Pinkston (2017) summarized the measured porosity, temperature, and vertical effective stress in Maconda well, Rigel well and well 562-1 in the Gulf of Mexico (Figure 2-21). In his fitted model, porosity reduces consistently with increasing temperature. He thinks that the porosity loss is mostly caused by expulsion of interlayer water during the illitization.

Smectite to illite transformation is often accompanied by quartz dissolution and cementation. In a sandstone reservoir or a shale reservoir filled with silica saturated pore fluid, Equation 2.3, 2.4, and 2.5 describe the diagenetic reactions with quartz dissolution and precipitation (Bjorlykke 1993).

$$K - feldspar + H^+ = Kaolinite + K^+ \tag{2.3}$$

$$K - feldspar + Kaolinite = illite + quartz \tag{2.4}$$

$$smectite + K - feldspar = illite + silica \tag{2.5}$$

Both pressure dissolution of quartz and clay mineral reactions lead to porosity reduction. With growth of quartz in the pore space, clay particles are cemented together with stronger shear resistance. In a macro scale, the stiffness of the material increases.

Framework weakening is caused by loss of shear strength between grain, or dissolution of load-bearing grains when temperature increases (Lahann and Swarbrick, 2011). Framework weakening due to shear strength reduction is discussed in Section 2.8. It explains why framework weakening due to temperature leads to porosity reduction and decrease in compressibility when the mudrock is further consolidated past yield point (quasi-preconsolidation effect).

2.6.3 Permeability Change Caused by Diagenesis

Section 2.4 describes the process of smectite to illite transformation. As a result of layer addition in the $00l$ direction and lattice growth in the x-y plane due to dissolution-precipitation, the volume of illite increases. When the volume of a clay mineral increases, its specific surface area reduces. According to Kozeny-Carman equation 2.6 (Carman, 1956), permeability (k) is a function of porosity (n), tortuosity (τ) and total specific surface area (TSSA) (S_a), G_s is the specific gravity. If

considering TSSA along and keeping the other variables constant, shale that goes through the transformation would have a greater permeability, because the specific surface area of neoformed illite is smaller than that of smectite. The TSSA will further reduces as the neoformed illite grows to well crystallized illite. However, in most observed sedimentary basin in the Gulf of Mexico where smectite-to-illite transformation is prevail, the shale permeability decreases.

$$k = \frac{n^3}{\tau^2(1-n)^2 G_s^2 S_a^2} \tag{2.6}$$

Nadeau (2005) and Bjolykke (1998) discovered that illite can occurs as a fibrous pore-filling mineral, in the sandstone or shale under a abnormal conditions where high pore fluid supersaturation, high pore fluid velocity, high temperature exist (Figure 2-22). The fibrous illite largely increases the tortuosity of the flow path, thus reducing the permeability significantly. At places where temperatures are above 100 °C, permeability in shale can be as low as 10^{-9} Darcy or 10^{-21} m^2 due to fibrous illitization (Nadeau, 2005). However, the fibrous illite is not commonly observed in natural basin.

2.7 Texture and Fabric Study of Diagenetic Clay Minerals

The study of clay mineral morphology replies heavily on the imaging technology. The advancement of Scanning Electron Microscopy (SEM) and Transmission Electron Microscopy (TEM) allow direct visual study of clay minearls down to the size of micron scale and nanometer scale.

Three basic morphologies—elongated hairy illite, illite lath, and platy illite flakes—are depicted in the Figure 2-23. The laths and plates are of common occurrence in a diagenetic basin compared to fibrous or hairy illite. The morphology of neoformed illite depends on the in-situ environment. According to Meunier and Velde (2004), the lathy illite formed from R0 to R1 stage, and platy illite mostly from R1 to more

ordered I/S. The lath shaped illite is most commonly observed in samples from a deep well in the Gulf of Mexico where S-I transition is from R0 to R1. As illite grows from I/S to lathy shape, and finally platy shape, the thickness of I/S mineral and illite crystal increases. Figure 2-24 shows the fundamental particle (N) thickness increases as the I % in I/S increases (Środoń & MaCarty, 2008). The thickness is measured by layer (N) counting from high resolution TEM lattice fringe images. Alternatively, Ferrage et al. (2011) obtained the N number from XRD profile fitting to estimate the thickness for each phases.

Nadeau (1985) use equation 2.7 to estimate the surface area of clay minerals using thickness of clay minerals.

$$S = \frac{800}{T} \tag{2.7}$$

where S is the total surface area in m^2/g, T is the thickness of a clay mineral in nm. Equation 2.7 suggests a inverse relationship between thickness of a clay mineral and surface area.

Day-Stirrat et al. (2011) investigated the orientation of clay minerals and effective stress. At low stress level (<1 MPa vertical effective stress) and at the same vertical effective stress, smectite has less preferred orientation than illite. With increasing stress level, the difference between different minerals become less obvious. The stress level becomes the dominant factor in controlling clay particle preferred orientation at greater stress level (2.4 MPa vertical effective stress), clay particles becomes perpendicular to the direction of the vertical stress (Figure 2-25).

Day-Stirrat et al. (2008) and Ho et al. (1999) observed increasing degree of alignment and porosity reduction with mineralogical changes. Figure 2-26 shows that mineral transformation has a greater influence than stress on preferred orientation. Figure 2-26a shows moderate alignment while b has well alignment. Samples in Figure 2-26a and Figure 2-26b are subjected to similar vertical effective stress level, but Sample b has a higher degree of transformation than a. The comparison of the two SEM images suggests that in the mineral transition zone, chemical compression is the dominant mode compared to mechanical compression.

Ho et al. (1999) also found that the degree of preferred orientation increases abruptly with the transition from R0 to R1 stage. The increase rate of preferred orientation drops in post-transition zone, the preferred orientation only increases slightly with increasing effective stress. This suggests chemical reactions including clay mineral transformation and quartz cementation have significantly stiffen the material.

Day-Stirat et al. (2008) also found that randomly oriented, curved smectitic particles are replaced by more rigid illite particles. The neoformed clay particles grow normal to the vertical effective stress, and the shape of those clay particles are platy. The effective stress does not affect the kinetics of the mineral transformation but only clay mineral morphology.

2.8 Time Dependent Behavior— Creep or Secondary Consolidation

In general, creep [1]or secondary compression is deformation without increase of effective stress. For soft clay or mudrocks, secondary compression occurs after the end of primary consolidation (EOP). Log time method is generally used to determine the EOP point on a consolidation curve in e-log(t) space or strain-log(t) plot. Void ratio (e) reduction or strain increment due to secondary compression is separated from primary consolidation by constructing two straight lines that intersects each other. The intersection point is EOP, the slope of the secondary compression in Figure 2-27 is C_α, and defined by Equation 2.8. Rate of secondary compression (C_α) is determined using 1D incremental loading test.

$$C_\alpha = \frac{\Delta e}{\Delta log t} \tag{2.8}$$

C_α is controlled by the viscous resistance of the material, it is a function of time, temperature, and stress level. It is a function of time, temperature and stress level.

[1]In the geotechnical world, creep is often referred to as secondary compression.

At low stress level, C_α decreases with time. At a stress level which is similar to the geologic scale, C_α increases with time. At elevated temperature, C_α increases comparing to that at room temperature. With increasing consolidation stress, C_α keeps increasing in the overconsolidated (OC) range, then remains approximately constant or reduces slightly in the normally consolidated (NC) range.

2.8.1 The Time Effect

Mesri and Castro (1987) found that C_α decreases with time. With longer time duration, C_α decreases ($C_{\alpha 1} > C_{\alpha 2} > C_{\alpha 3}$) in Figure 2-28.

Although C_α changes with time, the ratio of C_α over C_c stays rather constant (Mesri and Castro, 1987). At low stress levels (< 1 MPa), the $C_\alpha/C_c = 0.04 \pm 0.01$, for high plasticity soft clay, where C_c is defined as

$$C_c = \frac{\Delta e}{\Delta log \sigma'_v} \tag{2.9}$$

Karig et al.'s (2003) observed that C_α increases with time, which contradicts Mesri and Castro's result. In Figure 2-29, three disaggregated sediments from OPD site 897 were consolidated at different stress level (5 MPa, 8 MPa and 12 MPa) and then held stress to measure the rate of secondary compression. $C_{\alpha\eta}$ [2] has a sudden increase after 10^5 s. $C_{\alpha\eta}$ doubles or triples for C37 and C38 sample.

At high stress level, whether the rule for C_α/C_c ratio holds remains a question. Karig et al. (2003) points out that the well explained geotechnical concepts might not be valid under the geological conditions of high stress and very slow consolidation rates.

2.8.2 The Temperature Effect

According to Mitchell and Soga (2005), C_α increases with temperature. They explain that if sample is not heavily overconsolidated, with temperature increases, the shearing resistance between particles decreases, causing framework weakening. This

[2] $C_{\alpha\eta}$ is C_α in porosity space

reduction of shearing resistance leads to a reduction in the porosity until sufficient contact between grains are formed to regain shearing strength.

While the mechanism of increasing C_α with temperature is well explained, there is not much experimental data quantifying the magnitude of the increase. Duffy (2012) had measured the porosity reduction of a shale specimen at high temperature for 300 hours, but it was not fully consolidated to the end of primary consolidation, and it resulted inaccurate measurement of C_α.

2.8.3 The Stress Level Effect

According to Lambe & Whitman (1969), C_α increases in the OC range, and stays approximately constant or decreases with increasing stress level in NC region Figure 2-30. Karig et al. (2003) conducted 23 constant stress hold tests in the oedometers and found C_α increases with effective vertical stress in the OC range and then remains constant in the NC range (Figure 2-31). The modified $C_{\alpha\eta}$ of site 897 sample increases from a value of 0.001 at 1 MPa to 0.007 at 19 MPa. Although the data are scattered, the trend of increasing $C_{\alpha\eta}$ with increasing stress level in the OC range is clear.

2.8.4 Quasi-preconsolidation Effect

If a normally consolidated mudrock or soil sample undergoes extensive secondary compression, then continues to consolidate passing its present stress level, the stiffness of the material increases and it behaves like an overconsolidted sample. Once the vertical effective stress passes the maximum preconsolidation stress $\sigma_p^{'}$, the material behaves like a normally consolidated sample (Figure 2-32).

According to Mesri and Castro (1987), the overconsolidation ratio (OCR) increases as the time of secondary compression increases, the OCR ratio is defined by

$$OCR = \frac{\sigma_p^{'}}{\sigma_{vc}^{'}} = (\frac{t}{t_p})^{\frac{C_\alpha/C_c}{1-C_r/C_c}} \tag{2.10}$$

where $\sigma_p^{'}$ is the preconsolidation stress resulting from secondary compression; $\sigma_{vc}^{'}$ is

the consolidation stress at which secondary compression holds, t_p is the time to reach EOP, and C_r is the recompression index.

Not only samples that experiences secondary compression, but also samples with quartz cementation or mineral transformation, experienced thermal hardening, display this OCR effect or quasi-preconsolidation effect (Ladd, 1991; Mitchell et al., 2005). Combinations of several aspects often act together to create a overconsolidated sample.

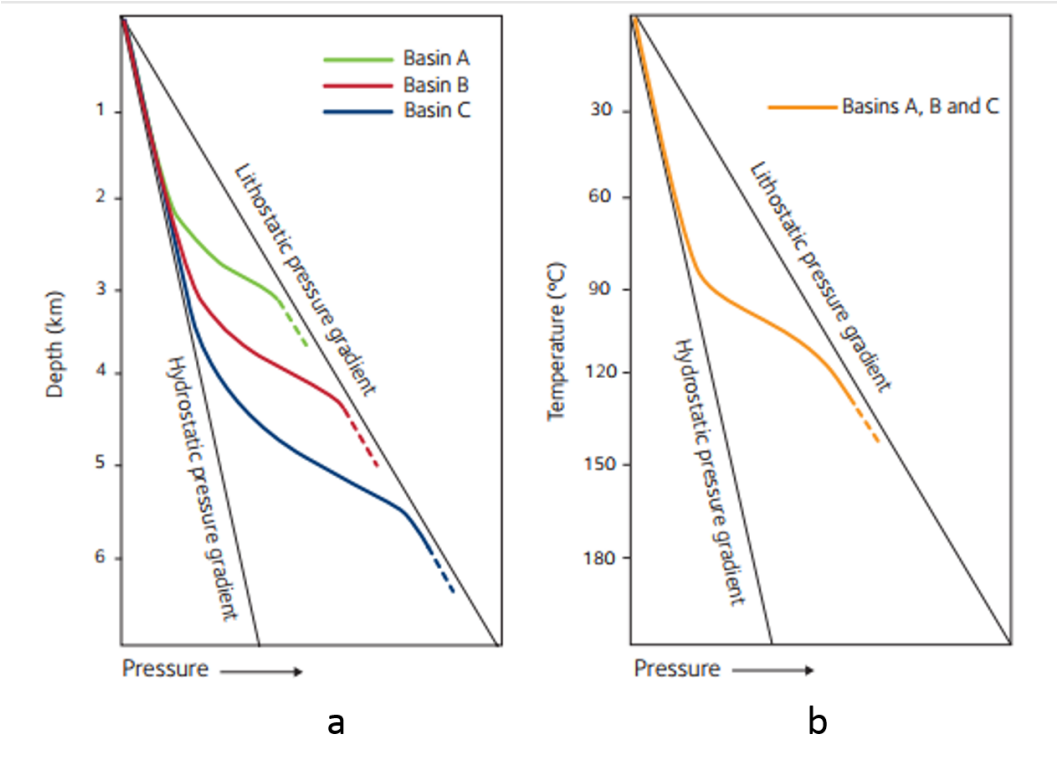

Figure 2-1: Generalized Overpressure Profile in Sedimentary Basins. (Nadeau, 2005)

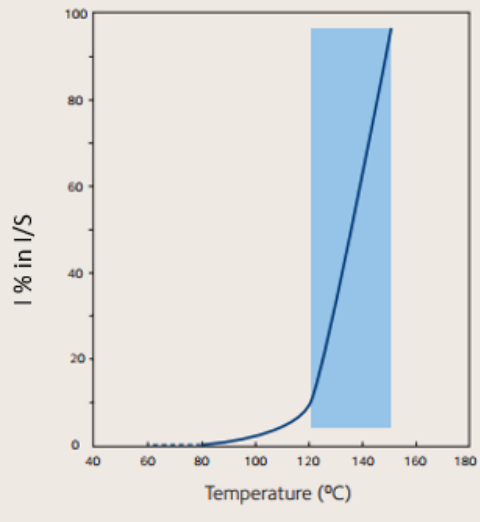

Figure 2-2: Generalized Illite Profile vs Temperature. (Nadeau, 2005)

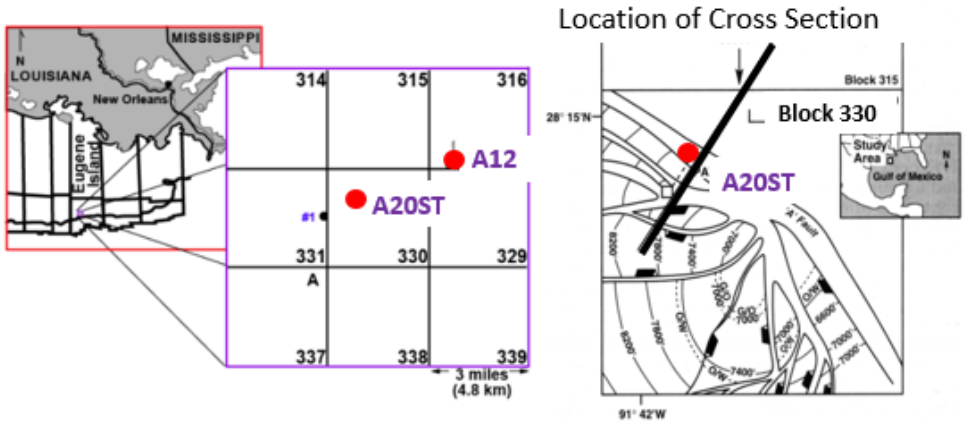

Figure 2-3: Location of Origin GoM-EI Source Material (Betts 2014). Material is cored from well A-12 at block 316 and well A-20ST - i.e., pathfinder well at block 330.

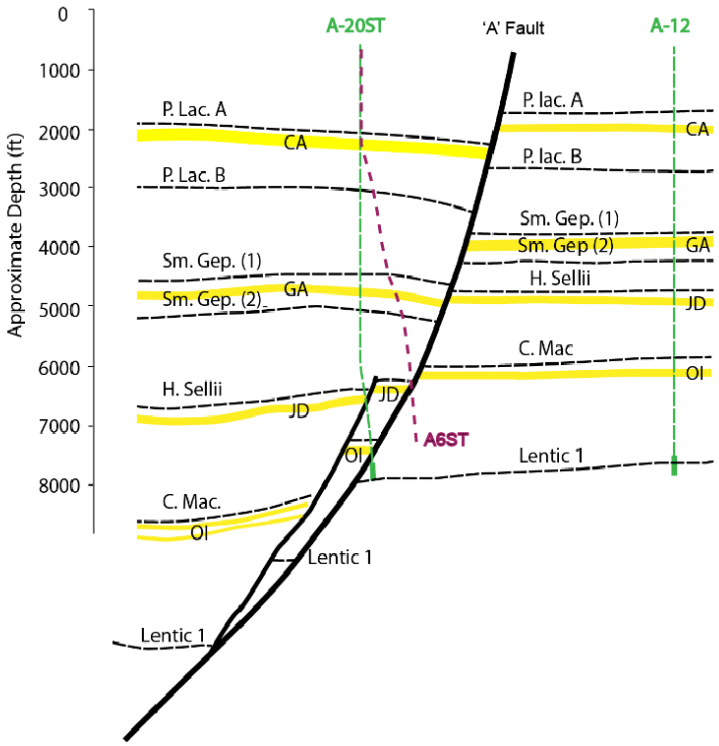

Figure 2-4: Profile View of Well A-20ST and Well A-12 (Alexander and Flemings, 1995). The GOM-EI sample used in my tests were cored from A-20ST and A-12 green enlarged section.

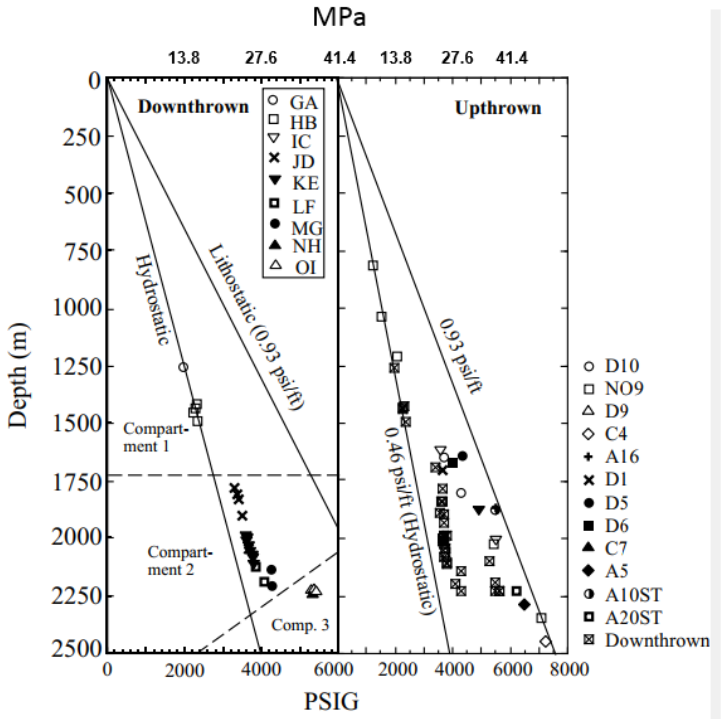

Figure 2-5: Pore Pressure Map of the Block 330 (Losh et al., 1999). The legend in downthrown stands for sand layer. The legend on the right side of the upthrown is bore hole number. The pore pressure data is collected from each well and sand layers.

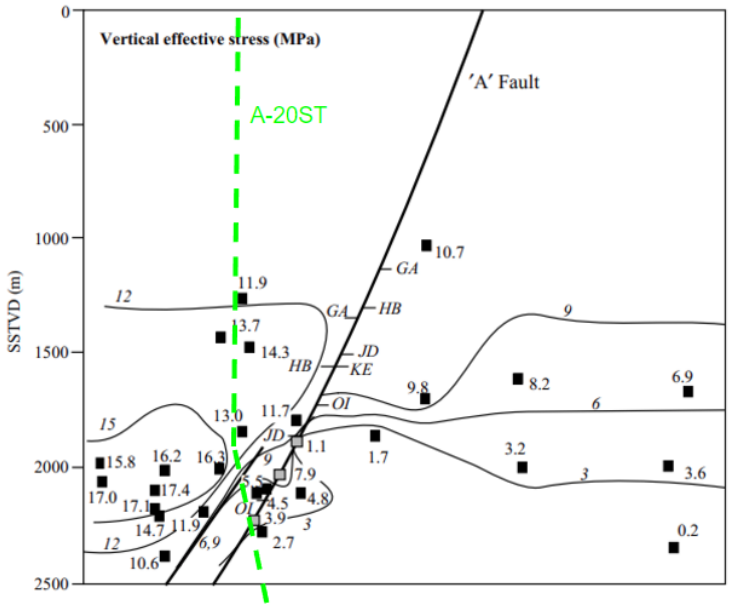

Figure 2-6: Vertical Effective Stress Contour Map of Block 330 (Losh et al., 1999). SSTVD stands for subsea true vertical depth. It is measured vertically from the sea floor.

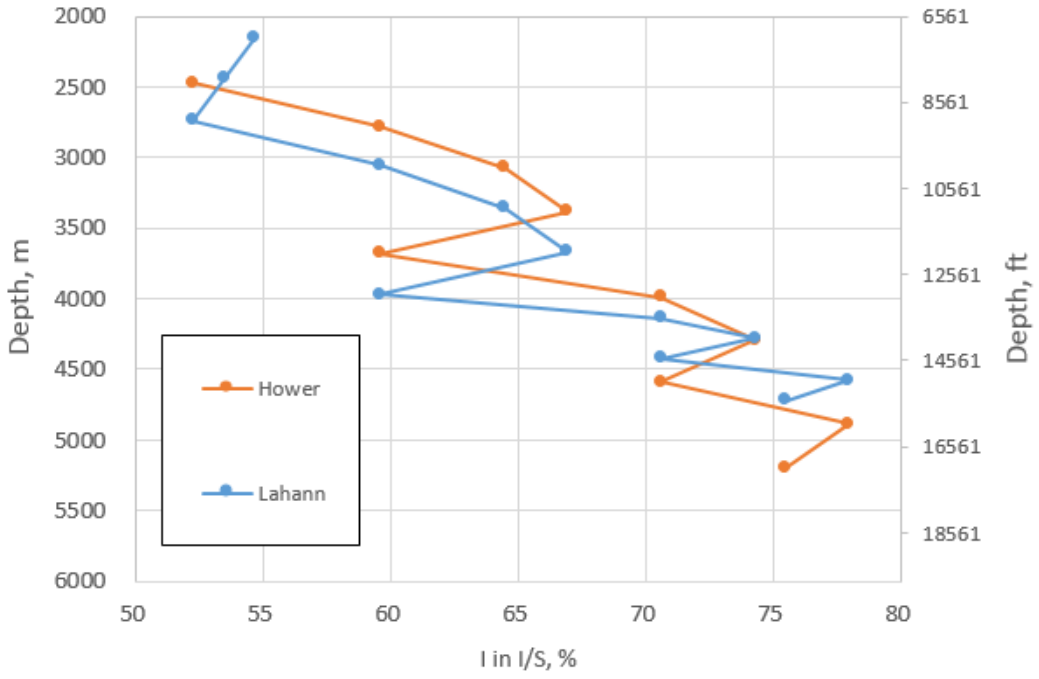

Figure 2-7: Illite % in I/S Phase Increases as a Function of Depth in the Gulf of Mexico. Orange curve is from Hower et al. 1976. Blue curve is from Lahann et al. 2001. Two curves show similar features in progression of S-I transition.

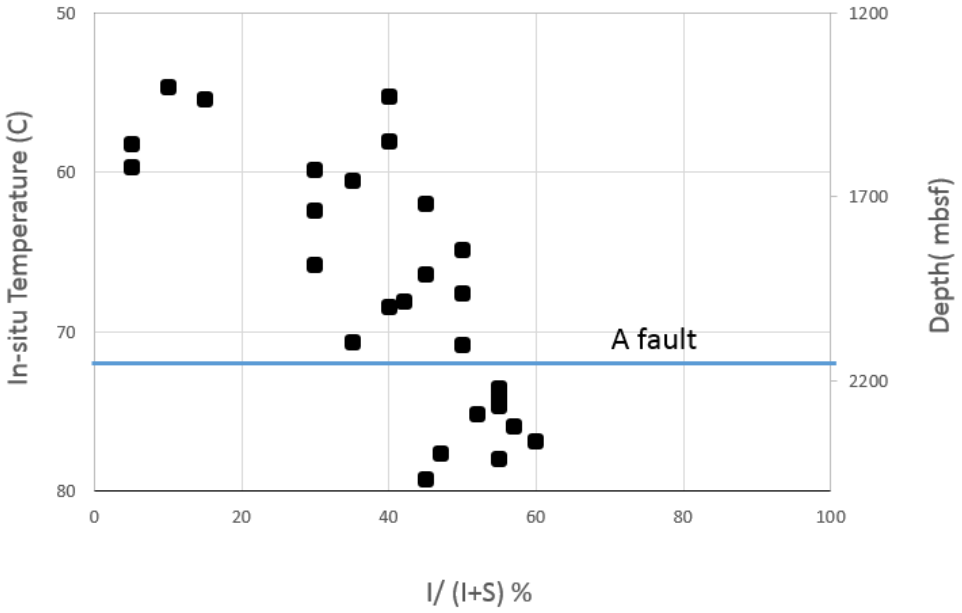

Figure 2-8: Illite Ratio of Well A-20ST (Losh,1999). The illite ratio increases with depth. The in-situ temperature at the fault zone is measured around 70°C. The location of the A fault is shown as the blue line.

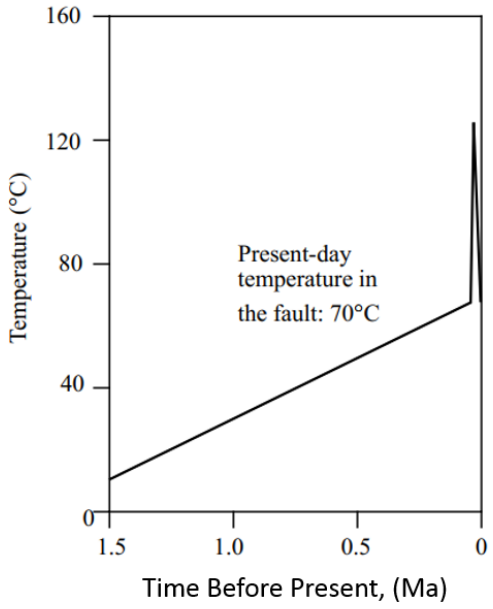

Figure 2-9: Modelled Temperature History at the A Fault Depth of Well A-20ST (Losh et al., 1999). A abnormal thermal pulse at 125 ° C occurred for a period of 2500 years. O in time axis is the present day.

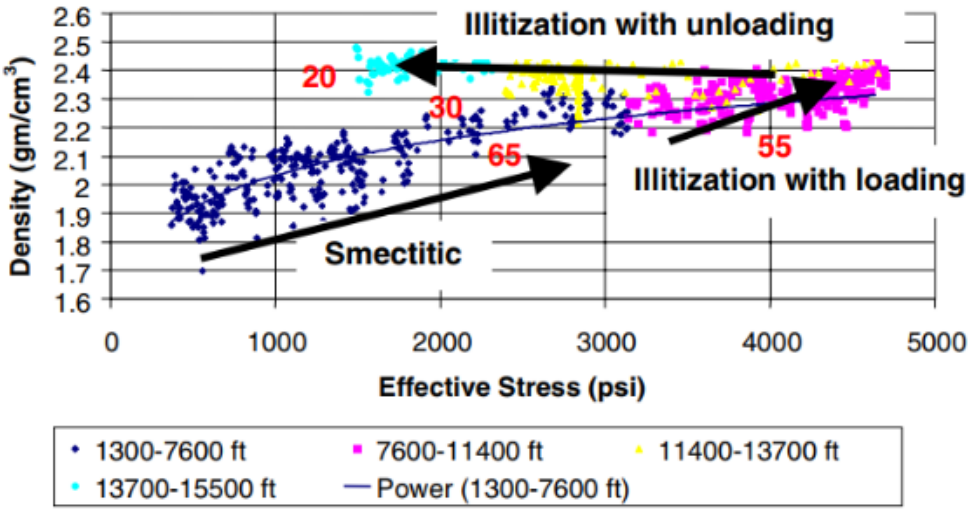

Figure 2-10: Stress Reduction due to Overpressure. (Lahann et al., 2001) Lahann relates the degree of illitization with density vs. stress profile. When I in I/S is below 45%, the sediments continue to load with illitization; but when I in I/S is greater than 45%, the density keeps constant with reduction of effective stress, the sediments unloads with increasing degree of illitization. The red number represents the smectite % in the I/S.

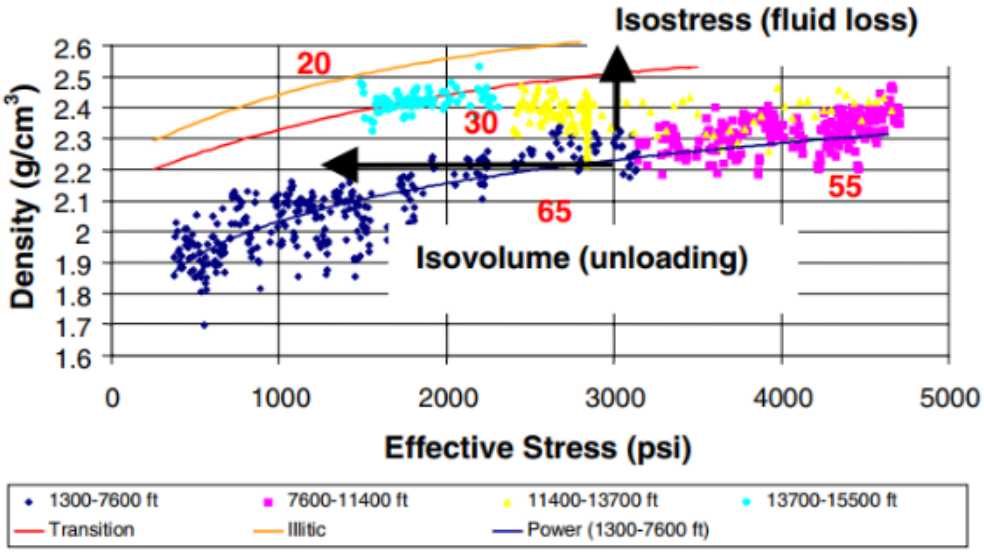

Figure 2-11: Two Modes of Bulk Density vs. Effective Stress. (Lahann et al., 2001). In a open system where the fluid is able to drain, the curve follows isostress path. In a low permeability system, the curve follows isovolume path.

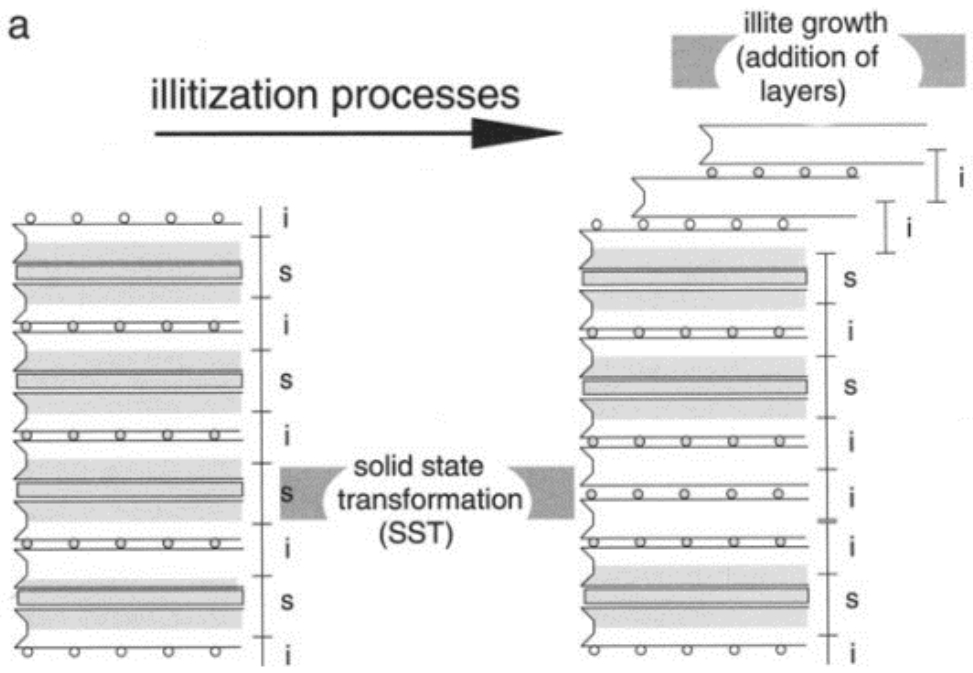

Figure 2-12: Solid State Transformation: Illite Growth by Layer Addition. (Boles and Franks, 1979)

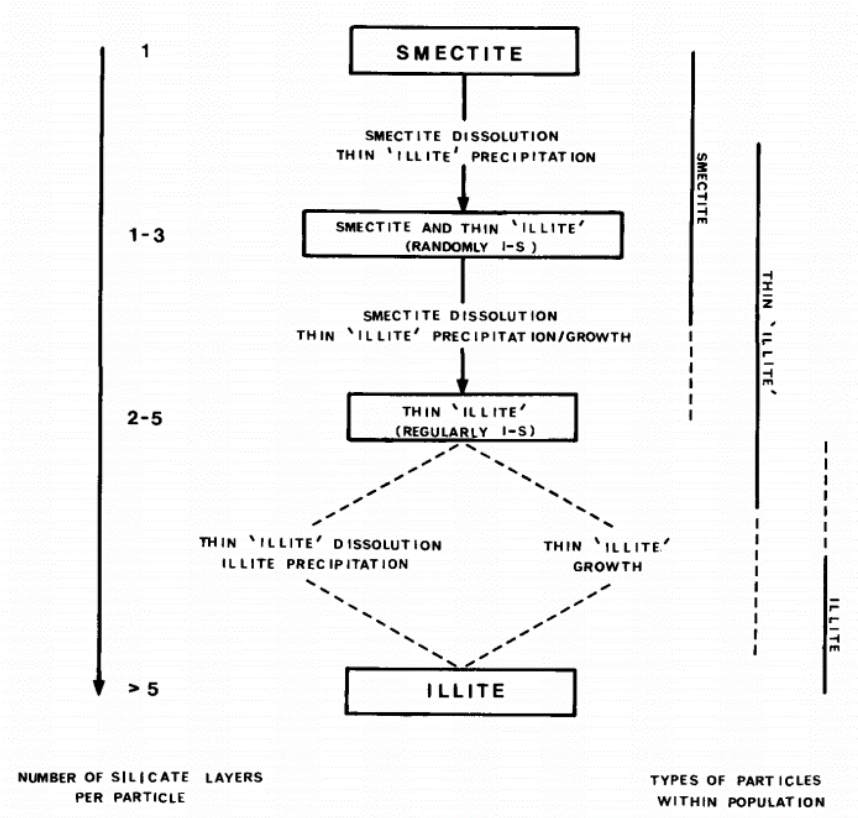

Figure 2-13: Dissolution and Precipitation Model of Smectite to Illite Transformation. (Nadeau et al., 1985)

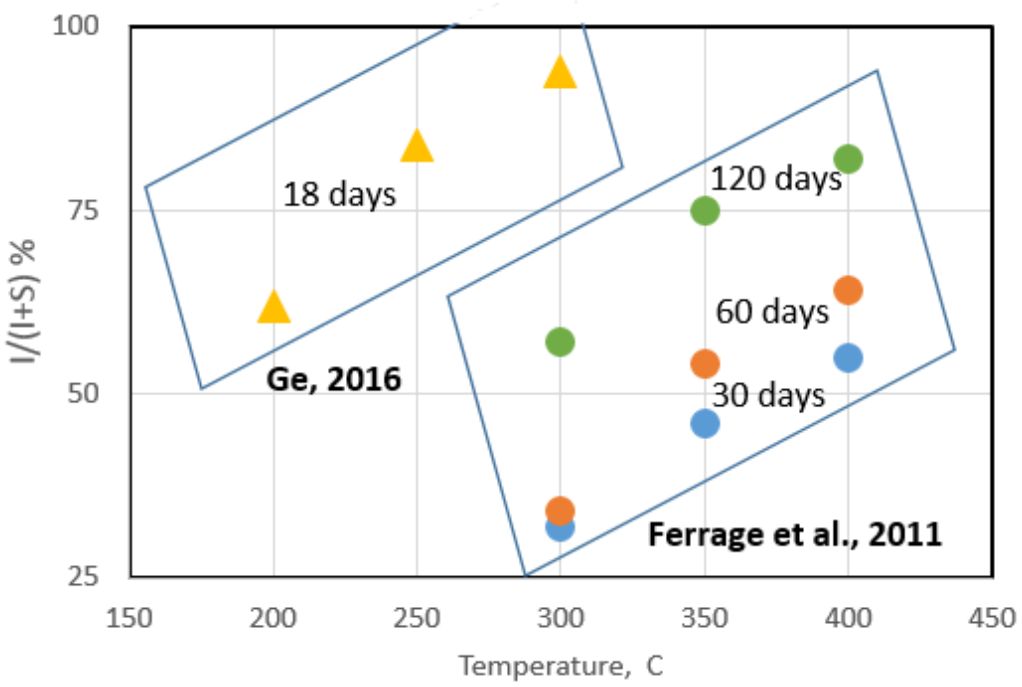

Figure 2-14: Illite Ratio vs. Temperature. The dots are from Ferrage et al. (2011). The triangles are from Ge (2016).

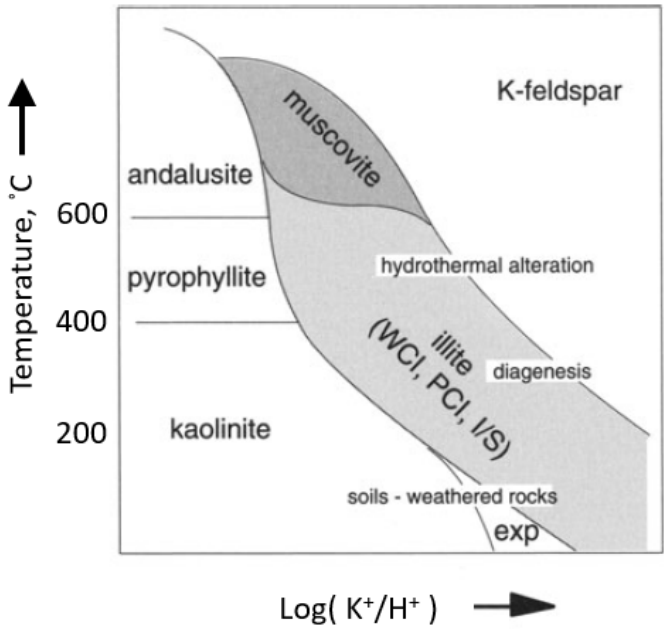

Figure 2-15: Favored Reaction Condition for Generating Illite (Montoya and Hemley, 1975). The y axis is the temperature, x axis is the ratio of K^+ to H^+. The formation of illite favours high K^+ and high temperature.

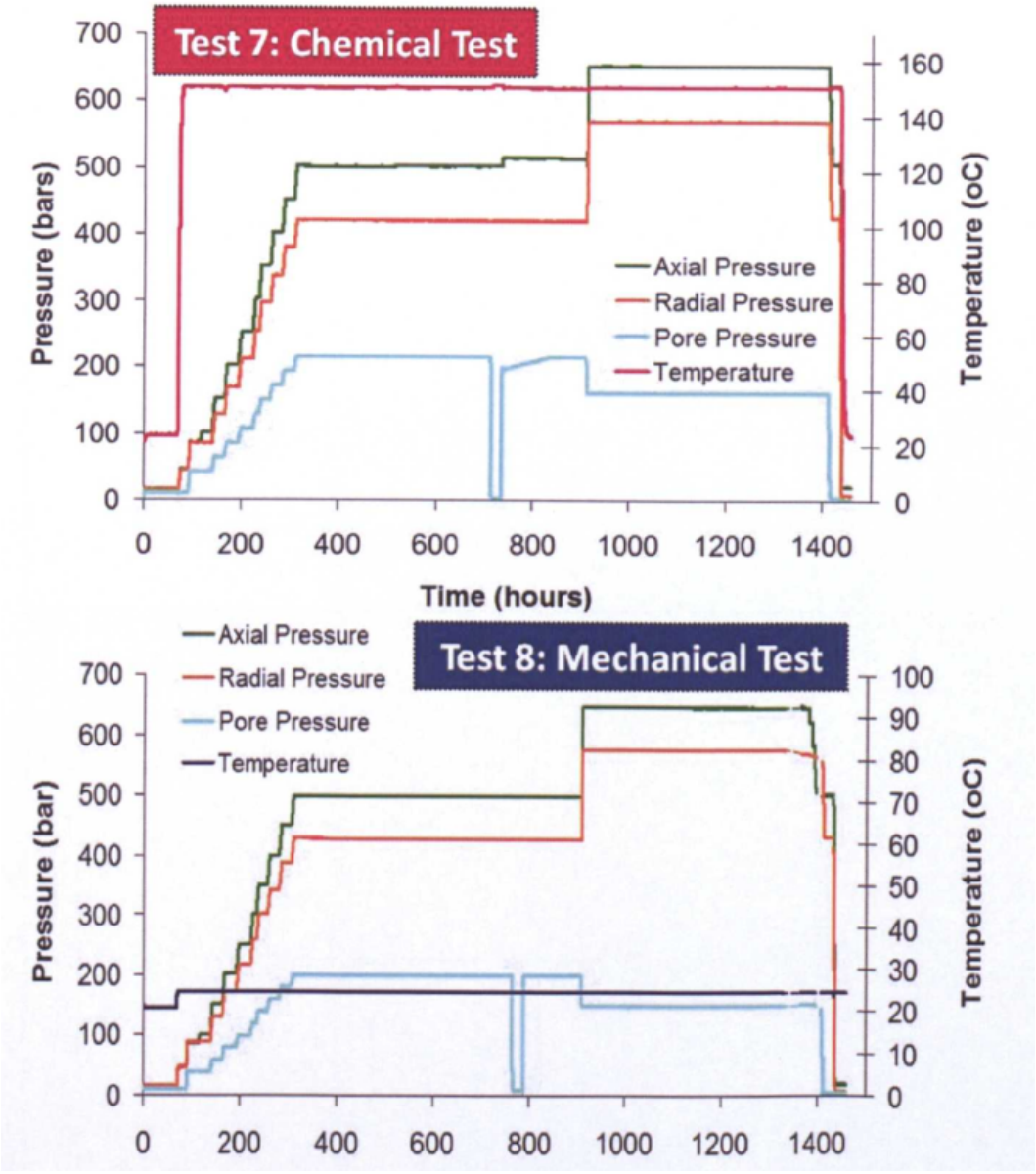

Figure 2-16: Test conditions for Comparing Chemical Compression and Mechanical Compression Duffy (2012). Test 7 is heated at 150 C, test 8 is at room temperature. The vertical effective stress level is at 30 MPa initially, then after 300 hours, increases to 50 MPa.

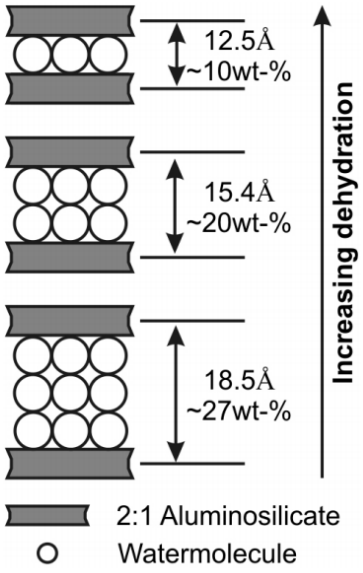

Figure 2-17: Interlayer Water inside smectite (Moore and Reynolds, 1997) Smectite can take in water as zero, single, double or triple layers of water. Single, double, triple layers correspond to a d-spacing of around 12.5Å, 15.4Å, and 18.5Å respectively for sodium saturated smectite

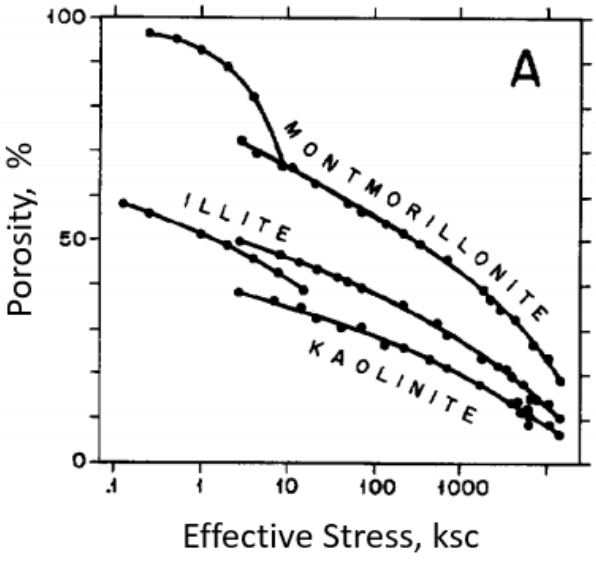

Figure 2-18: Compression Curves for Smectite, illite and kaolinite (Meade, 1966).

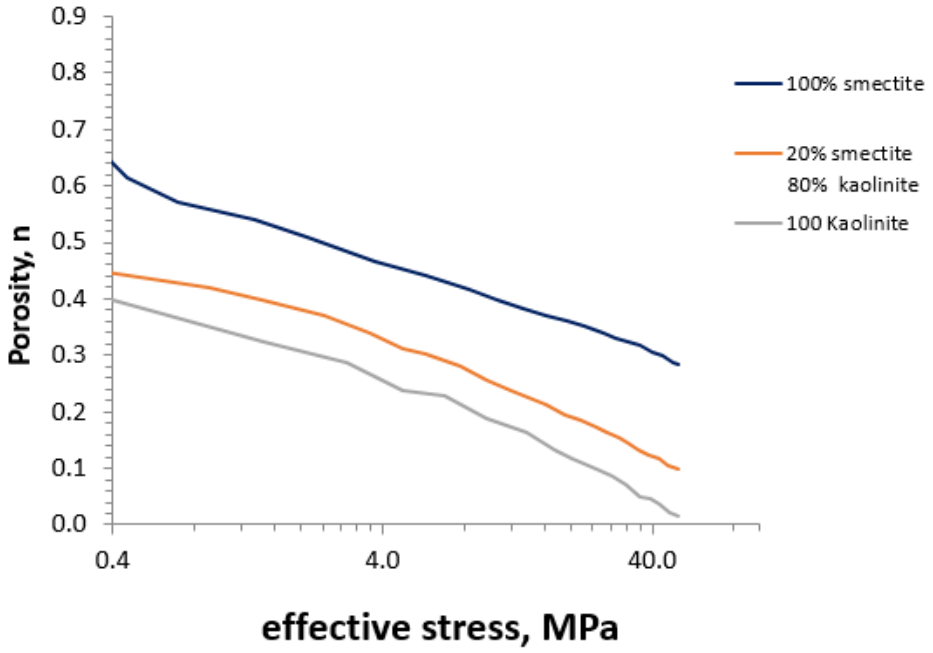

Figure 2-19: Compression Curves for Smectite, kaolinite, and smectite kaolinite mixture (Mondol et al., 2007). The pure smectite has the highest porosity at any given vertical effective stress, the pure kaolinite the lowest. The mixtures of smectite and kaolinite are between the pure smectite and kaolinite line, the 20 % smectite and 80 % kaolinite is shown in figure as an example.

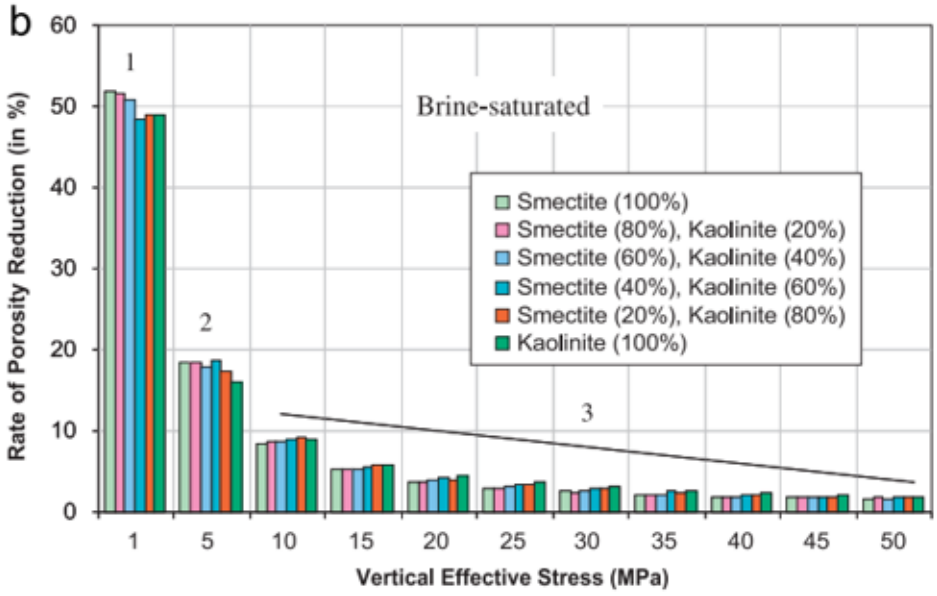

Figure 2-20: Porosity Reduction Rate vs. Vertical Effective Stress (Mondol et al., 2007). Stage 1 and 2, the porosity reduction rate of 100% smectite is higher than 100% kaolinite. In stage 3 the higher stress level, the order reverses.

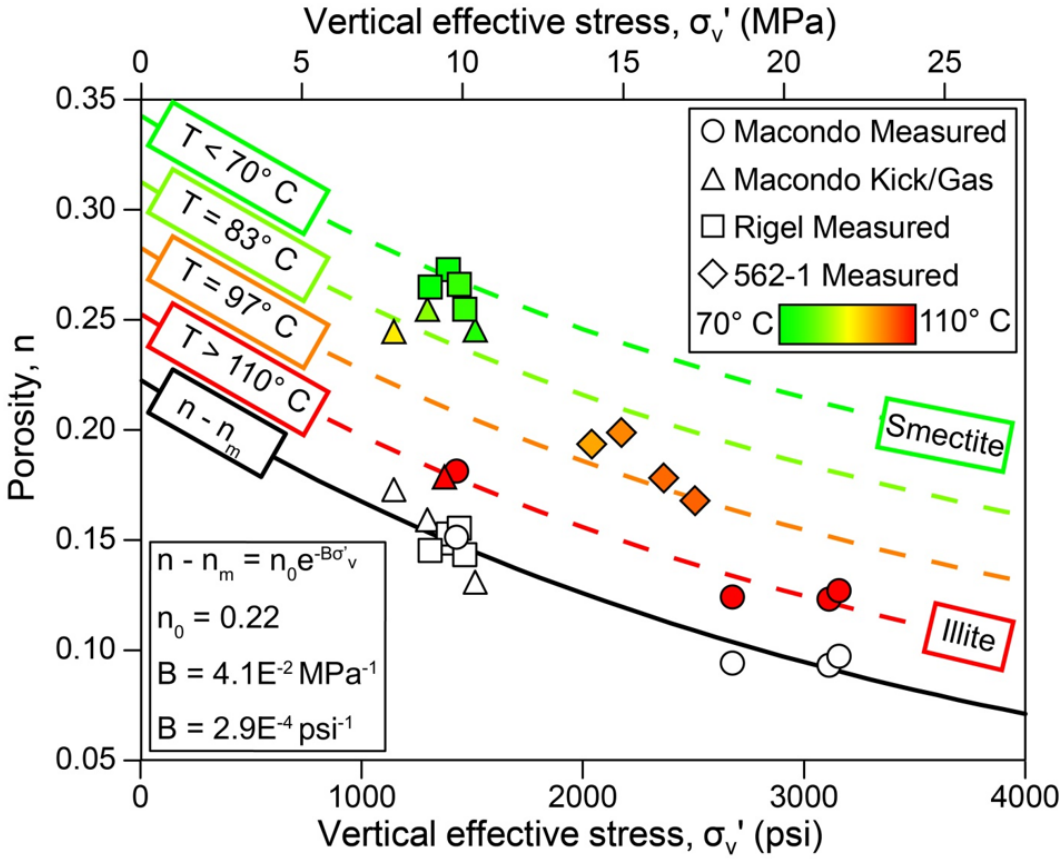

Figure 2-21: Fitted Compression Curve Accounting for Different Temperatures at Gulf of Mexico (Pinkston, 2017). Solid symbols represent measured data. Open symbols are fitted based on model of temperature effect.

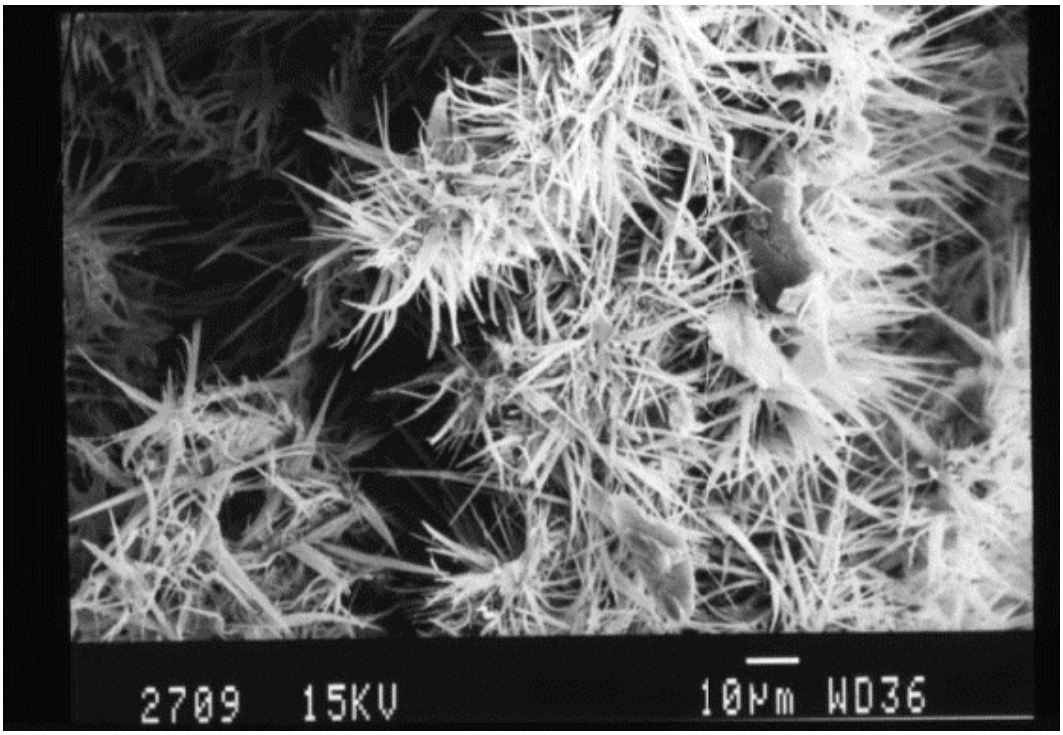

Figure 2-22: Fibrous Illite in Sandstone (Bjolykke, 1998). The Fibrous illite forms in abnormal conditions and significantly reduces permeability.

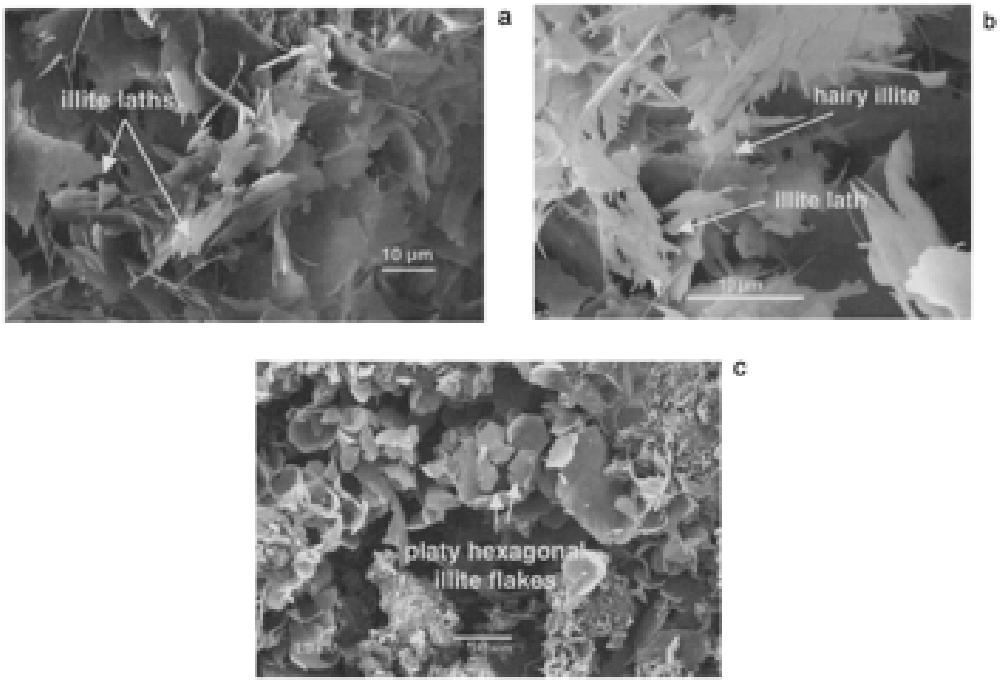

Figure 2-23: Three Basic Morphology for Illite (Meunier and Velde, 2004). a) illite laths b) hairy illite and illite lath c) illite flakes

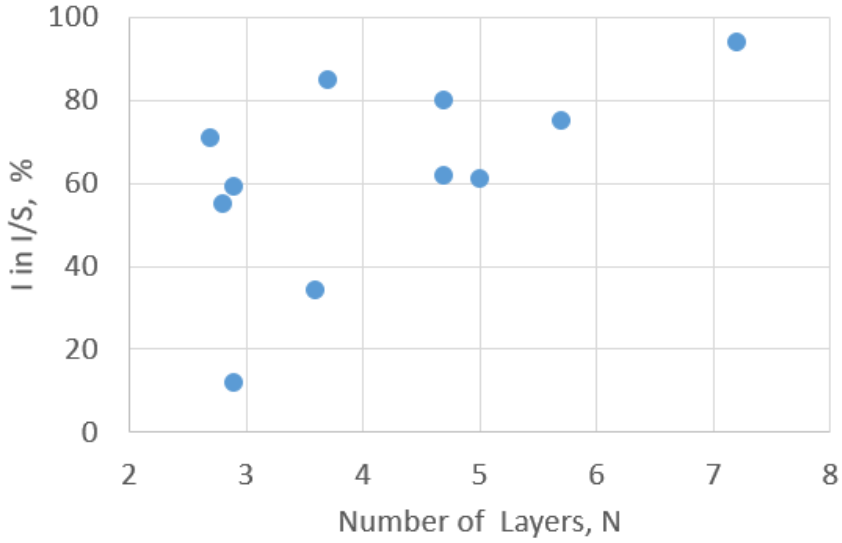

Figure 2-24: The Clay Layers (N) in a McEwan Structure increase with I in I/S% (Srodon et al., 1992). A pure smectite mineral has about 3 clay layers. When the transformation occurs, the N increases with addition of illite layers.

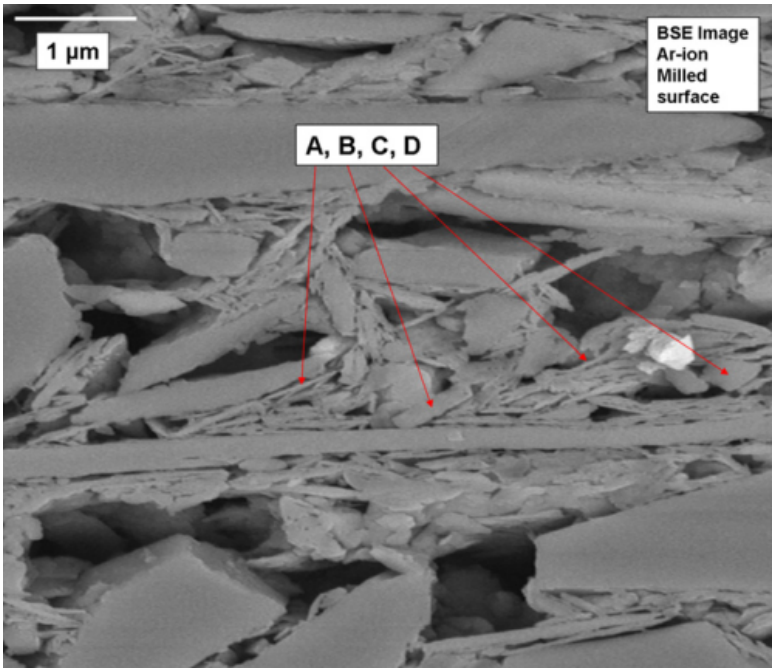

Figure 2-25: Clay Particles Lay Perpendicular to the Direction of the vertical stress (Day-Stirrat et al., 2011).

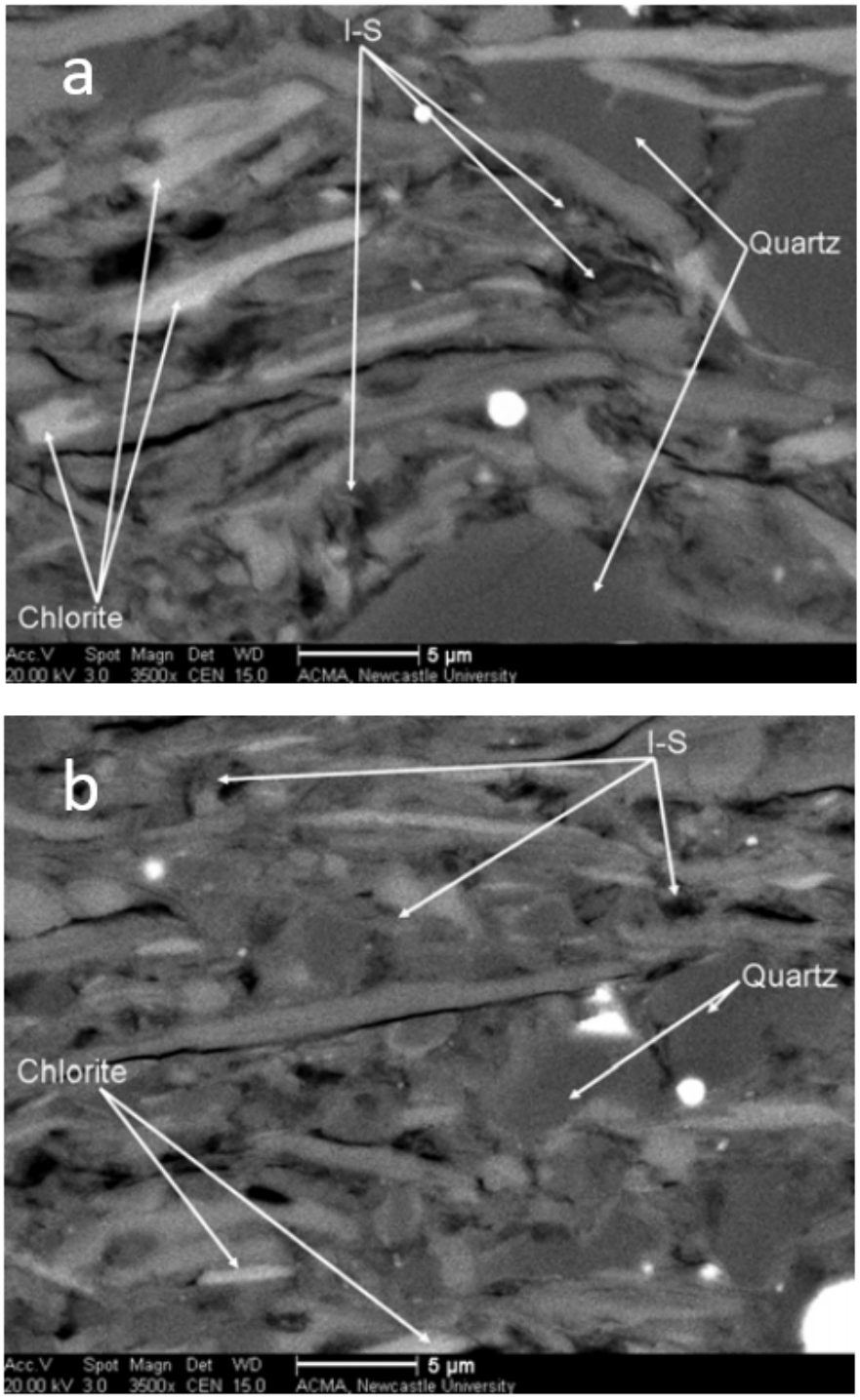

Figure 2-26: The Effect of Mineral Transformation on Preferred Orientation (Day-Stirrat et al., 2008). Samples in a) and b) are subjected to similar vertical effective stress level, but Sample b has a higher degree of preferred orientation as well as mineral transformation.

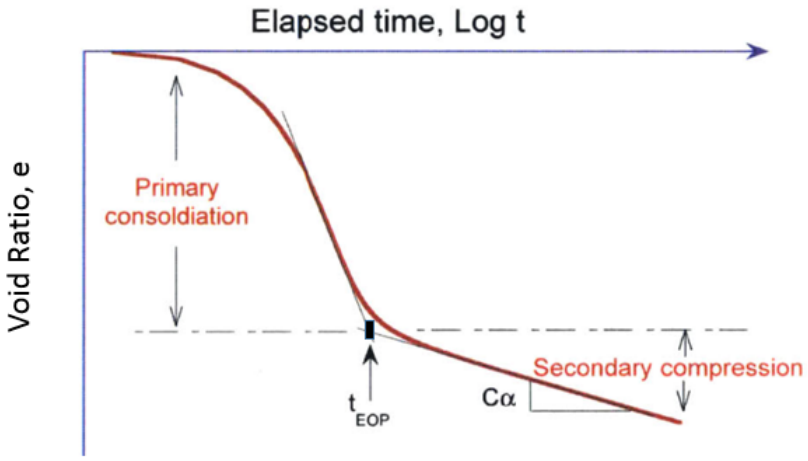

Figure 2-27: Void Ratio vs. Log Time for 1D Incremental Loading Test (1.32 Soil Behavior Lecture Note). The EOP point is determined by the intersection point of the primary consolidation slope line and secondary compression slope line. The slope of the secondary compression defines C_{alpha}

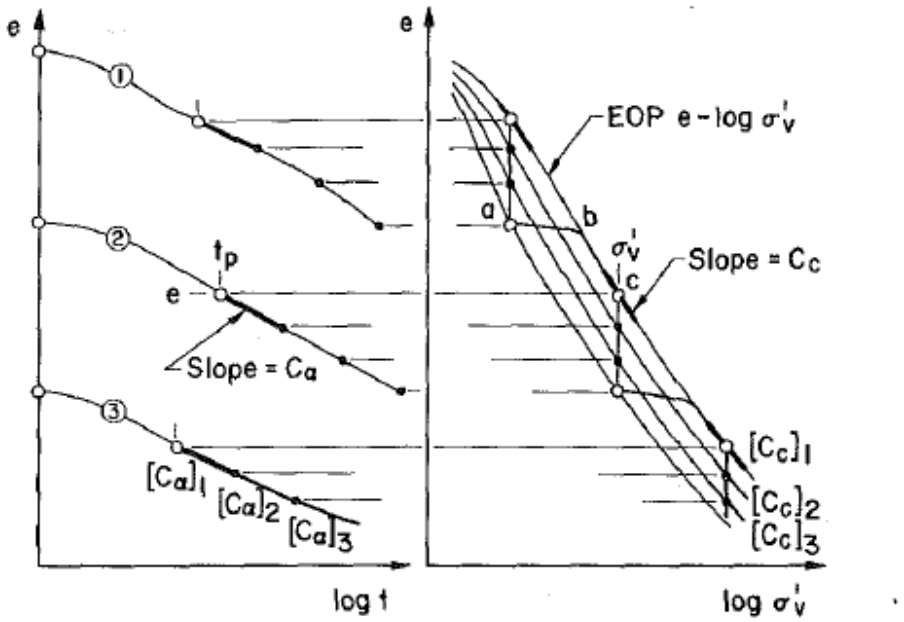

Figure 2-28: The Slopes of C_α and C_c in the compression Curve (Mesri and Castro, 1987). C_α decreases with time.

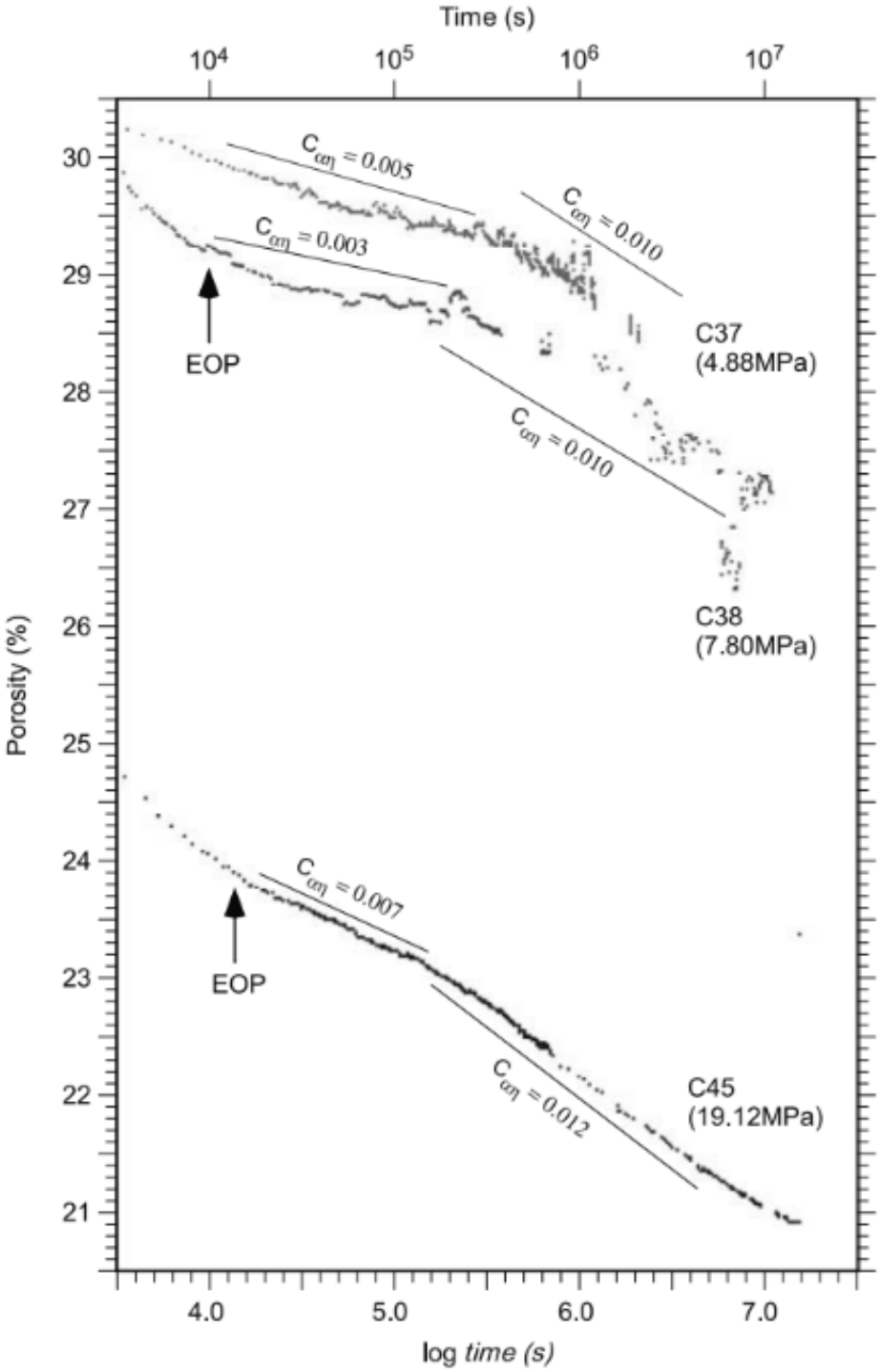

Figure 2-29: $C_{\alpha\eta}$ increases with time (Karig et al., 2003). $C_{\alpha\eta}$ doubles for C37, triples for C38, increases by 73 % for C45 after 10^5 seconds

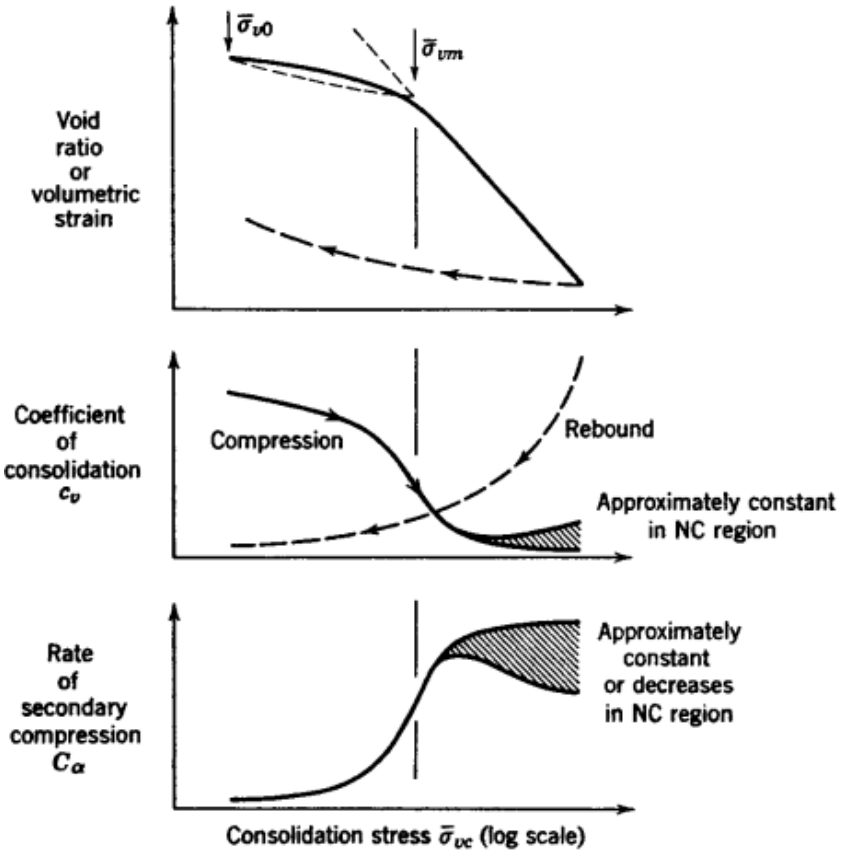

Figure 2-30: C_α as a function of stress level (Lambe & Whitman, 2008). The C_α shows increasing trend in the OC range, and keeps constant or decreasing trend in the NC region.

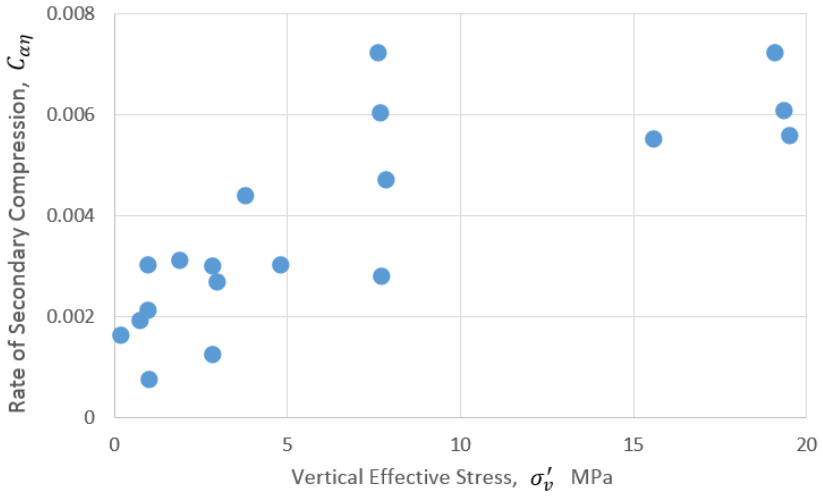

Figure 2-31: C_α vs. Vertical Effective Stress (Karig et al., 2003). The preconsolidation stress for ODP samples is around 7.5 MPa. C_α increases in the OC range, then remains approximately constant.

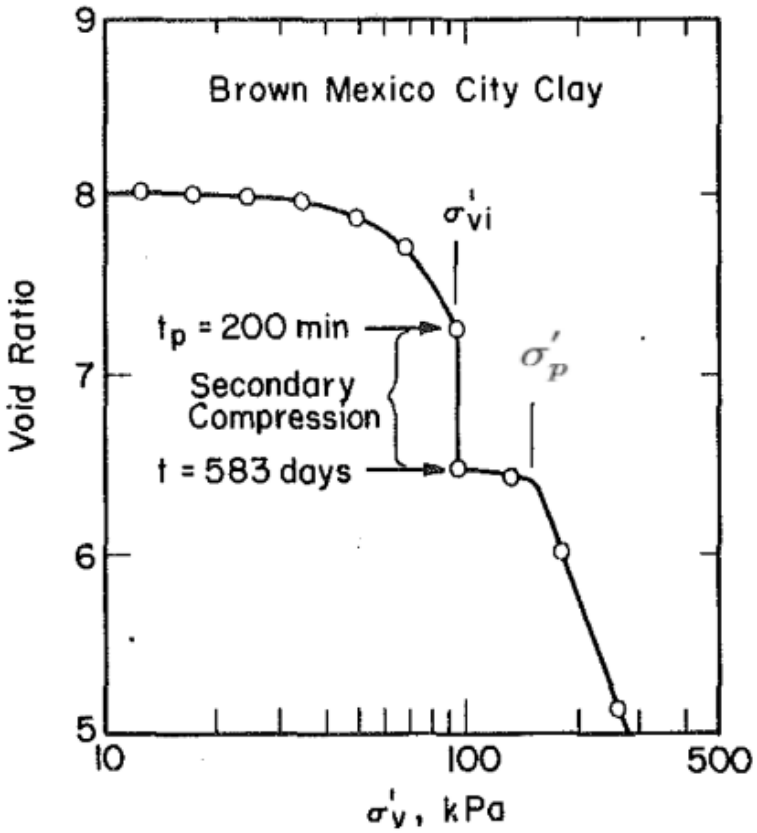

Figure 2-32: Secondary Compression Induced Quasi-preconsolidation Effect (Mesri and Castro, 1987). $\sigma_v^{'}$ is the consolidation stress, $\sigma_p^{'}$ is the preconlidation stress due to secondary compression.

Chapter 3

Test Materials

This chapter provides the geological information on the material used for the research as well as information about the material processing. Information about the geological setting, in situ temperature, mineralogy, pore pressure and vertical effective stress are recorded. This chapter also covers the leaching process, salt mixing procedures and resedimentation process.

3.1 Geological Setting

The Gulf of Mexico- Eugene Island(GoM-EI) source material was retrieved from the Eugene Island block located off the coast of Louisiana. It was extracted from two borings namely well A-20ST or pathfinder well in Block 330 and well A-12 in Block 316 (Figure 2-3). The cored section (the green enlarged section in Figure 2-4) was from the interval between elevation 6690'(2039m) and 7550'(2301m) below the sea floor. The sandy intervals were discarded; the fine grained material was air-dried, roller ground to a fine powder with 99 % passing the #100 sieve, and homogenized. The geological environment in Block 330 was well studied and documented by Losh et al.(1999) and Hart et al.(1995). The ODP expedition at the Northeastern Gulf of Mexico was a major scientific endeavor to study and understand the geologic, chemical and thermal conditions of a major growth fault (also termed the "A" fault in Figure 2-3 and Figure 2-4).

3.2 The mineralogy of the original GoM-EI source material

The original GoM-EI source material is a mixture of core samples from well A-20ST and well A12 (see section 3.1). A representative sample was sent to Shell for XRD measurements on both the bulk and the clay size fraction ($<2\ \mu m$). Dr. Day-Stirrat analyzed the XRD pattern and quantified the mineral composition. The procedures for analyzing the XRD pattern is explained in detail by Ferrage et al. (2011), who quotes the probability research on disordered lamerllar structures by Drits and Tchoubar (2012). This method generates a XRD pattern from a disordered lamerllar structure, and fits the theoretical XRD pattern to the measured XRD pattern by optimizing the structure parameters of each clay mineral phase and the weight fraction of each phase.

There is another mineralogy report analyzed by Macauley Institute in Aberdeen, Scotland. It is referred by Fahy(2014), Adams(2014) and Marjanovic (2016) as the mineral composition of GoM-EI. The method used by Macauley is described by Hiller (2003). The quantification was done by a normalized full pattern reference intensity ratios (RIR) method.

As emphasized by Moore and Reynolds (1997), there is no single correct way to quantify clay minerals. It depends on the analyzer's understanding of mineralogy and geology. There are heterogeneity, failures and complexity.

Table 3.1 presents the bulk composition of original GoM-EI. The majority of the sample is 2:1 clay minerals which are mainly illite and smectite. The results for 2:1 clay minerals and quartz from Shell and Macaulay are similar, $\sim$ 40% of 2:1 clay minerals and $\sim$ 25% quartz. Both Shell and Macualay have identified phases that are greater than 3 % being Kaolinite, K-feldspar, Plagioclase and Barite. The percentage of Muscovite has a discrepancy of $\sim$ 9% between Shell result and Macualay result.

Table 3.2 summarizes the mineral composition of the clay fraction. Both results are correct, but they differ in the their assumption on the discrete smectite phase. Macaulay's interpretation has 0 % of the discrete smectite and 87 % of I/S; Shell's

result shows 43 % of discrete smectite and 31 % of I/S. Since Macaulay assigns the discrete smectite to I/S phase, the smectite percentage in the I/S phase is interpreted as 70-80 % while Shell's data have only 24 % in the I/S phase.

Losh et al. (1999) presents the illite % increase along the depth of A-20ST well as I/(I+S)%. At the A fault postion (Figure 2-8), the I/(I+S) % of the in situ sample is about 50 %.

Using the Equation 2.1, the I/(I+S)% is calculated as 42% and 27-36% from Shell and Macaulay respectively. Both number are lower than the in situ value from Losh et al.(1999), because the source material is a mixture of A-20ST and A12.

Table 3.1: Bulk Composition of Original GoM-EI

Minerals	Shell	Macaulay
2:1 Clay minerals	42.3	44.4
Quartz	24.2	27.8
Muscovite	10.7	1.9
Kaolinitic	7	9.1
K-feldspar	5.4	4
Plagioclase	3	5.3
Barite	3	3.2
Choloritc	2.3	0.4
Calcite	0.9	1.2
Anatase	0.5	0.2
Ankerite	0.4	0.8
Rutile	0.3	0
Sylvite	0	0
Nahcolite	0	0
Siderite	0	1
Pyrite	0	0.7
Sum	100	100

Table 3.2: Mineral Composition of Clay Fraction ($< 2\mu m$) of Original GoM-EI

Minerals	Shell	Macaulay
Chlorite	4	1
Kaolinite	9	4
illite	13	8
discrete smectite	43	0
I/S	31	87
Sum	100	100

Smectite in I/S	24	70-80
I/(I+S)	42	27-36

3.3 Leaching Process

The original GoM-EI source material has approximately 8 g of natural salt (mostly NaCl) for every 1 kg of dry powder. Huang et. al (1993) pointed out that an excess amount of Na^+ cation slow down the smectite to illite transformation. One important step for the research is to leach out the excess Na^+ cation.

Adams (2014) and Fahy (2014) had standardized the procedures for leaching salt from mudstones. Sections 3.3.2 in Fahy (2014) and 3.1.4 in Adams (2014) provide detailed procedures. About 1 kg of GoM-EI was dispersed in 1200 mL water, then placed in dialysis tubes. Dialysis tubes were positioned evenly-spaced in a container filled with distilled water. The bath water was exchanged twice a day for approximately 30 days. Desalting process was considered finished when the conductivity of the bath water dropped below 35 $\mu S/cm$. In Fahy (2014) and Adams (2014), the bath water conductivity reading for a stop mark is set to 10-20 $\mu S/cm$ (Figure 3-1).

The stop mark for the leaching process is a relative number in terms of probe sensitivity. A good way to determine the stop value is to measure the conductivity of tap water and distilled water. The Fisher Accumet #13-620-102 probe used in this research measures tap water as $\sim 50\,\mu S/cm$, distilled water $\sim 20\,\mu S/cm$. The VWR probe used in previous studies is more sensitive and measures distilled water $\sim 5\,\mu S/cm$. In addition, the conductivity vs. time curve (Figure 3-1) gives a suggestion for the stop value. The conductivity of bath water was taken roughly every 24 hours, and started from 3500 $\mu S/cm$, dropped sharply in the first 100 hours, remained rather steady after 500 hours at a value of 45 $\mu S/cm$.

After the leaching process, the slurry was extracted from the dialysis tubes. The slurry was air dried to a consistency of tooth paste, then spread on several glass plates with a thickness of less than 1 cm to air dry completely. The completely dry clay chunk was then ground with hand grain mill from Wonder Mill to a fine powder with 99 % passing the #100 sieve .

Fahy (2014) found that dialysis tubes have a service life of about 15 days, and he had to transport the slurry to new tubes to finish the leaching process. This hustle

can be avoided by preventing dialysis tube from exposure to sunlight. Dialysis tubes become chemically unstable with long term exposure to UV light. If tubes are taken good care of and kept in a place without natural light, the dialysis tubing can survive up to 30 days.

3.4 Resedimentation Process

Intact offshore samples are formed by sedimentation processes. Sedimentation is a slow geological process where particles in suspension settle out of the fluid. The deposited sediments consolidate under their own weight on a time scale of millions of years depending on sedimentation rate. Testing intact specimen are therefore infeasible in terms of sample disturbance, the cost associated with extracting deep offshore samples, variability among the intact sample.

Resedimentation is a more reliable and reproducible method to produce specimens of identical composition from source material with controling on desired preconsolidation stress, porosity and pore fluid salt concentration. The resedimentation process was developed and modified by Germaine (1982), Seah (1990) and Abdulhadi (2009).

The resedimented specimens produce a reasonable analog for field intact samples. Betts (2014) demonstrated a good agreement between the compression behavior of resedimented GoM-EI specimens and intact samples (Figure 3-2). The green dots are CRS test data on a resedimented specimen, The red and orange dots are uniaxial consolidation tests data on two intact core specimens from well A-12 (2039 mbsl) and A20ST (2240 mbsl) respectively. The red dots are almost identical to the green dots. The orange dots are slightly stiffer than the green dots. The solid line is an experimentally derived compression curve representing the porosity vs. effective stress in the Ursa Basin in the Gulf of Mexico (Long et al. 2001). The solid line overlays the green dots at low stress level.

Both the sonic log and the density log have challenges to match with resedimented specimens. The pink dots are calculated based on sonic log using empirical correlation from Hart et al. (1995), they do not converge with resedimented specimen data until

an effective stress is greater than 7 MPa. The blue dots are calculated based on bulk density log, they sit higher in void ratio than the resedimented specimen.

The basic resedimentation procedures (shown in Figure 3-3) include: 1. mixing salt solution; 2. blending ingredients; 3. deairing; 3. tremieing; 4. consolidation.

Details of the resedimentation process are given by Marjanovic (2016), Nordquist (2015) and Fahy (2014), and are not repeated in this section. The differences between this research and the predecessors' are that: 1. the pore fluid used is 3 mol/L KCl solution rather than sea salt solution; 2.the water content for a stable yet workable slurry is about 75 %; 3. the fine powder used in the process has no sea salt.

3.4.1 Mixing KCl Salt Solution

Adams (2014) generated a look-up table for proportioning ingredients with sea salt solution at a specific salinity. If one needs to prepare 1 L of 80 g/L sea salt solution, he/she would need 80 g of sea salt and 976.25 g of distilled water. A common error is to mix 80 g of salt with 1 L of water, because salt also occupies volume.

The density of the salt solution changes non linearly as a function of salinity. When the salt molecules dissolve in the water, the two different molecules pack closer together than in their pure phases, resulting in a reduction of volume and a increase of solution density.

Equation 3.1 is used to calculate the density of the KCl solution. In order to make the equation work, the effective salt density ρ_{salt} is treated as a function changing with salinity.

$$\rho = \frac{M_{salt} + M_w}{V_{salt} + V_w} = \frac{M_{salt} + M_w}{\frac{M_{salt}}{\rho_{salt}} + \frac{M_w}{\rho_w^T}} \tag{3.1}$$

where ρ is the density of the salt solution in g/cm^3, ρ_w^T is the density of water as a function of temperature, M_i are the masses in g and ρ_{salt} is the effective density as a function of salinity in g/cm^3.

Wolf et al. (1975)'s look-up table lists KCl solution density (ρ_{wolf}) with corresponding salinity over a range of $5g/L$ to $279g/L$, but the tabled values are discrete and with huge steps. In order to generate a continuous function, the coefficients A,

B and D of the polyfit function in Equation 3.2 need to be determined by minimizing the objective function Equation 3.3. The objective function sums the square of difference between the tabled KCl solution density and calculated KCl solution density at discrete salinity using Equation 3.1.

$$\rho_{salt} = Ac^2 + Bc + D \tag{3.2}$$

where c is the salinity of solution in g/L,

$$SSE = \Sigma(\rho_{wolf} - \rho)^2 \tag{3.3}$$

The value for coefficients in Equation 3.2 are $A = -4.542 \times 10^{-6}$, $B = 9.83 \times 10^{-4}$, $D = 2.49$.

Using Equation 3.2, a table for KCl mixing is provided in Appendix A. For instance, to prepare a 3 mol/L or 223.5 g/L KCl solution, the water needed is not 997.3 g (1L volume), assuming 24 ° and a density of 0.9973 g/cm^3, but 907.53 g.

The KCl salt used in the research is ACS grade with a purity of 99%-100%, and has a dry density of 1.98 g/cm^3 at 20°C.

3.4.2 Salt Crystallization During Resedimentation

Serious salt crystallization problems occured in the early stage of the resedimentation. For high salinity ($223.5g/L$ or 3 mol/L) samples, the salt builds up on the surface of the acrylic tube (Figure 3-4). The salinity of the pore fluid reduces as a result of salt crystallization, causing uncertainty when calculating the initial void ratio of the specimens.

To solve this problem, a comparative experiment between PVC tubes and acrylic tubes was conducted. Three tubes were half submerged in a high salinity solution. After 15 days of sitting at room temperature, there was significant salt build up on the acrylic tube, while there was no salt crystallization on the PVC tube. So the PVC tubes were chosen over acrylic tubes, when resedimenting high salinity specimens.

There are two dimensions of the 1.5 inches clear PVC pipes: schedule 40 and schedule 80. PVC tubes used in this research are 1.5 inches schedule 40 clear PVC pipes. The actual inner diameter measured is 1.59 inches. It leaves a gap of ~ 0.2 inches to trim a 1.4 inches diameter CRS sample with bigger tolerance.

For triaxial specimens, 1.5 inches schedule 80 PVC pipes were used. The wall thickness of schedule 80 pipe is greater than schedule 40 pipe, so that triaxial specimens can be resedimented to a higher stress level.

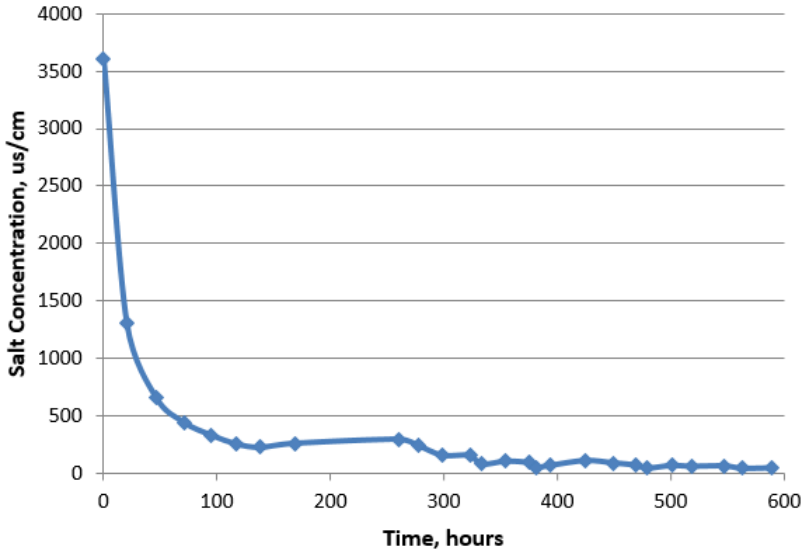

Figure 3-1: The Bath Water Conductivity Reading during the Leaching Process of GoM-EI. The salinity shows an exponential decay as a function time.

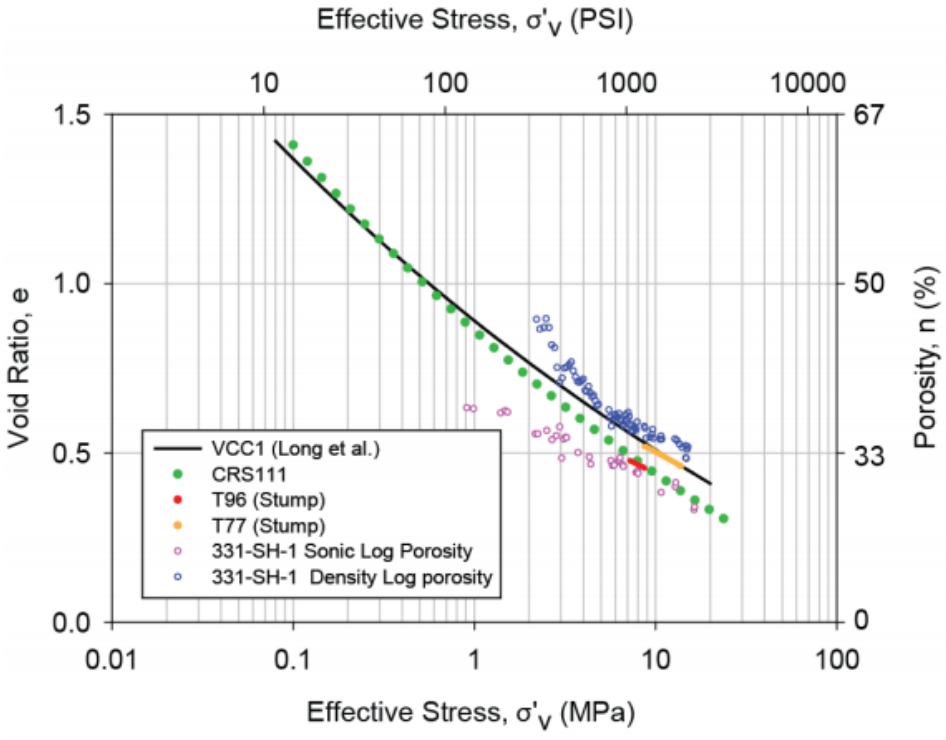

Figure 3-2: Comparison of Compression Behavior between Intact Lab Samples and Resedimentation GoM-EI Specimens and Field Logs (Betts 2014)

Figure 3-3: Basic Stages in Preparing Resedimentation Batch

Figure 3-4: Crystallization of KCl Salt with $3mol/L$ pore fluid during Resedimentation with Acrylic Tubes

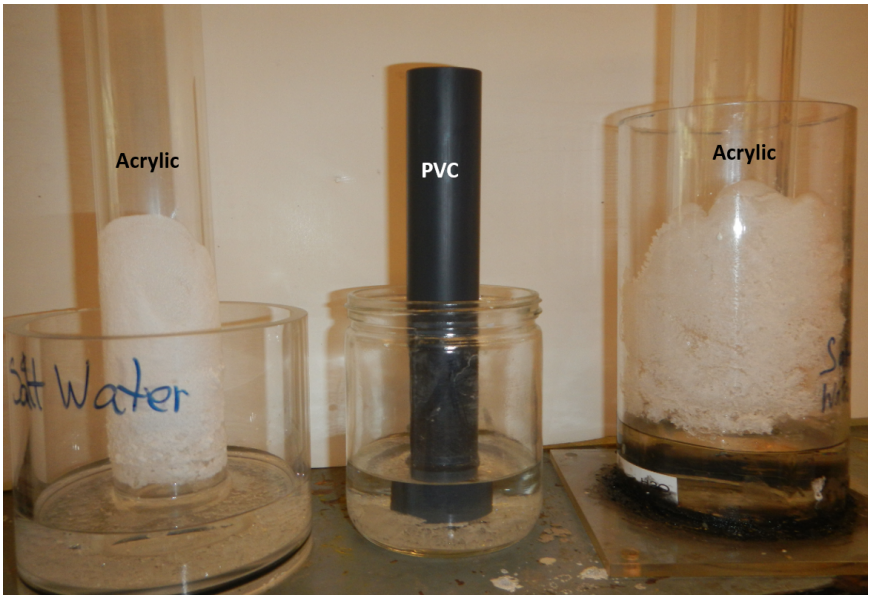

Figure 3-5: Comparison of Salt Crystal Formation on PVC and Acrylic Tubes

Chapter 4

Methodology and Equipment

This chapter describes the method and equipment used in the research to measure the mudrock behavior change including the permeability and compressibility change due to mineral transformation.

In this research, a multi-functional high temperature CRS device is designed from scratch to tackle the challenge of measuring the mechanical properties of a mudrock and transforming the clay minerals with effective stress.

The high temperature CRS system consists of: the CRS cell, the temperature control system to adjust the temperature of a specimen inside the CRS device, the load frame and hydraulic system to apply the cell pressure and axial load , the control system and data acquisition system to automate the entire testing process.

Additionally, the hydrothermal reactor is the alternative equipment to induce mineral transformation, the difference is that the sample is cooked in a slurry state. The hydrothermal reactor system is also described in this chapter.

A smectitic material has high total Specific Surface Area (SSA), while an illitic material has a much lower total SSA. The value of total SSA provides indication of the degree of the smectite-to-illite transformation. The method and equipment for measuring SSA is described in this chapter.

4.1 Methodology for Comparing Material Behavior Change due to Mineral Transformation

The goal of this research is to compare the changes in the behavior of the mudrock due to the smectite-to-illite (S-I) transition. A comparative experiment is designed as shown in Figure 4-1. The loaded test (the top row in the Figure 4-1) set the baseline for a smectitic mudrock. The loaded test is a standard CRS test conducted at room temperature.

To produce an illitic mudrock, two protocols are used: A. cooking the specimen with effective stress (the second row in the Figure 4-1) B. cooking the leached GoM-EI source material in slurry state without effective stress applied (the bottom row in the Figure 4-1).

Protocol A compresses the resedimented leached GoM-EI to 5 MPa vertical effective stress in the high temperature CRS device; then holds vertical effective stress at 5 MPa; heats the smectitic specimen to 200 °C for 30 days to facilitate S-I transition; cools down the specimen to room temperature; loads cooked specimen to 100 MPa.

Protocol B transforms the original leached GoM-EI mudrock in a slurry state at 250 °C for 18 days using a hydrothermal cooker. The illitic slurry is then transferred into a resedimentation column to prepare the specimen for testing. The illitic specimen is later resedimented to 0.1 MPa and tested in a CRS device to see the change.

The starting strain rate for all three tests is the same, 0.6 $\%/hr$. In test protocol A, when compressing the specimen after the thermal cycle, the strain rate is reduced to 0.3 $\%/hr$. All specimens are resedimented to 0.1 MPa then unload to a OCR ratio of 4 in 3 mol/L KCl solution. During the CRS tests, the cell fluid is also KCl solution.

The protocol A procedure is designed with the following logic. Referring to Lahann et al. (2002), Figure 2-11 illustrates two modes of compression behavior that a mudrock can experience when material go through S-I transition. The first mode is isovolume, which happens in a low permeability closed system; another mode is isostress, which occurs in a high permeability open system. In this study, the drainage

height of a CRS specimen (12.7 mm thick) is short, and the top drainage surface is open, therefore the simulated laboratory environment is similar to the condition of isostress in geologic state.

4.2 Design Requirements for High Temperature CRS System

The high temperature CRS device is designed with the objective of transforming a smectitic mudrock to an illitic mudrock with effective stress applied, and testing the compression and permeability behavior change due to the mineral transformation.

In order to achieve the goals, this device needs to meet the following four requirements :

1. able to compress mudrock up to a stress level of 100 MPa
2. able to heat and maintain the device up to a temperature of 200 °C
3. able to seal the cell fluid at a temperature of 200 °C
4. able to record the transducer voltages at high temperature.

4.3 The High Temperature CRS Device

The body of high temperature CRS device is made of 17-4 PH stainless steel. The piston bearing is made of bronze. The design process was in collaboration with Stephen Rudolph and Prof. Germaine. The machining of the device was completed by Stephen Rudolph at the MIT Civil Engineering Department Machine Shop. The main parts are piston, chamber, cutting shoe, and base (Figure 4-2). The specimen is sandwiched between two ceramic based porous stone and sited inside the cutting shoe (Figure 4-3). The cutting shoe or the trimming ring serves two functions: constraining radial strain to allow uniaxial compression only and trimming the specimen into the confining ring with minimum disturbance. The piston contacts the top porous stone to apply a vertical load to the specimen. The specimen for high temperature CRS device is 35.6 mm (1.4 in.) in diameter and 12.7 mm in thickness.

The elevated area of the base directly goes into the center hole of the cutting shoe. The O-ring inside the recess of the elevated area forms a seal against the inside of the CRS cutting shoe, isolating the excess pore pressure at the base. The pore pressure hole at the center of the base is connected to a Omega® PX102 pressure transducer.

The entire cutting shoe and partial of the chamber is covered by a 500 w mica heating band. The temperature is measured at the base through a 1.6 mm (1/16 in.) diameter tunnel beneath the specimen by a Omega® Type K thermocouple (Figure 4-3). Two heat break discs, that are made of furnace brick, prevent heat transfer to the load cell and hydraulic jack.

The axial deformation is measured by two LVDTs attached to the piston by LVDT holder. The fluid is seal by three 0-rings. The top one seals the gap between piston and chamber, the middle one chamber and cutting shoe, the bottom one chamber and base.

Main Body Material Selection

Stainless steel is the material of choice when the device has to endure high salinity and high temperature environment. 17-4 HP (H1150) was chosen over 316 and 304 stainless steel as the material for the device, because it provides excellent mechanical properties and its tensile yield strength is over three times that of 316 or 304 stainless steel (Table 4.1).

In the loading stage, the cutting shoe experiences radial expansion, the piston experiences compression. The strength of the 17-4 HP stainless steel must be greater than the stresses.

Hook stress of the cutting ring due to the radial expansion is calculated by Equation 4.1.

$$\sigma_H = P[\frac{(R_2/r)^2 + 1}{(R_2/R_1)^2 - 1}] = 140\ MPa \tag{4.1}$$

$$P = \sigma_v \times K_0 = 90\ MPa \tag{4.2}$$

Where P is the radial stress, R_2 is the outer radius of the ring, R_1 is the inner radius of the ring. P is calculated as 90 MPa, assuming K0 ratio of 0.9 at 100 MPa vertical effective stress (Casey, 2014), when $r = R_1$, the hoop stress σ_H reaches the maximum value of 140 MPa.

In the vertical direction, the piston stress is calculated by Equation 4.3. The piston diameter (31.75 mm / 1.25 in.) is designed to be close to the diameter of specimen (35.56 mm/ 1.4 in.) to accommodate the high stress level, so that the steel in the vertical loading direction does not yield. The highest compressive stress, the piston can experience, is 125 MPa.

$$\sigma_{piston} = 100\ MPa \times [\frac{R_{specimen}}{R_{piston}}]^2 = 125\ MPa \tag{4.3}$$

Table 4.1: Tensile Strength of Different Stainless Steel

Type of Stainless Steel	17-4 PH	304	316
Tensile Strength, 0.2 % Yield (MPa)	1034	215	290

In summary, both the σ_{piston} and the σ_H are below the tensile strength of the 17-4 PH stainless steel.

Seal Material Selection

The most common material for O-rings used in the CRS and triaxial tests are neoprene rubber. The maximum service temperature is 121 °C. Both Viton and Karlrez O-ring have a temperature rating that is higher than the target temperature 200 °C. Karlrez has a better performance in chemical resistance. The performance of the Viton and Karlrez O-rings is discussed in the Chapter 4.3.4

Table 4.2: Properties of Different O-rings

Material	Neoprene	Viton	Karlrez 4079
Max Service Temp. (°C)	121	260	316
Linear Coefficient of Thermal Expansion, (/°C)	1.39E-04	1.30E-04	3.61E-04

Insulation Material

The insulation material at the top and the bottom of the high temperature CRS device are made of furnace brick, the thickness of the insulation disk is 12.7 mm (0.5 inch). It is able to prevent heating of the electronics. The load cell temperature is the same as the atmosphere temperature during heating stage.

4.3.1 Temperature Control System

The circuits diagram of the heating control system is in Figure 4-4. The thermocouple is connected to MYPIN TD4 microcontroller (MCU). This MCU is programmed to drive the low DC voltage side of the solid state relay to regulate the high AC voltage that powers the heating element.

The MCU was calibrated to maintain the temperature of the high temperature CRS device within ± 3 °C.

4.3.2 Load Frame and Hydraulic System

The load frame is designed and custom-made for the 100 MPa stress level CRS devices. It consists of a top and a bottom 7.62 cm (3 in.) thick steel plates connected with four 3.81 cm (1.5 in.) diameter threaded steel bolts, a Enerpac® (model RCS-1002) hydraulic jack sitting on the bottom plate and a Sentran® (model PG3) low profile load cell mounted on the top plate (Figure 4-5). Both load cell and hydraulic jack have a capacity of 222 kN (50 kip), which can measure and provide up to 280 MPa total vertical stress for a 35.6 mm diameter specimen.

The hydraulic jack in the load frame is driven by a computer controlled pressure volume actuator (PVA). The vertical stress PVA accommodates Duff-Norton® inverted ball screw jack driven by a ElectroCraft® servomotor. The cell pressure is controlled by the same type of mechanism but has a smaller capacity PVA.

4.3.3 Control System and Data Acquisition System

Autonomous control of stress path and strain rate as well as autonomous digitization and recording of transducer voltage is a necessity for soil and rock testing. Autonomous control relieves researchers of physical operation once the test is fully set up. The data acquisition system converts the analog voltage to digital signal and stores the data for post processing. It saves researchers from manually reading the numbers.

The control hardware used in this research consists of: 1. a computer that has the ability to do analog-to-digital conversion (ADC) and the ability to send analog control signals; 2. motor controller to regulate the RPM of the DC motors; 3. relays to turn on and off the motors; 4. transducers that provide instant readings.

The control software is programmed using QBasic language. The software was first developed by Sheahan (1991) and Germaine for controlling triaxial testing, then modified by Germaine and author for CRS application. Chapter 5.1 covers the detail of the control algorithm.

The hardware and software form a closed loop feedback control system. The process follows: an ADC installed inside the PC converts the analogue voltage output of the transducers to digital signal; the control software makes judgment or mathematical logic by comparing the measured engineering values with the target values, then sends out an analog signal to motor controller to regulate the speed of the motor. The motors drive the shaft of the PVAs to control cell pressure and axial load precisely.

In terms of data storage, the build-in ADC does not store the transducer signals in a hard drive but only monitor them. The transducer signals are collected for post processing by Hewlett Packard HP3497A data acquisition unit. The HP data acquisition system is configured to simultaneously monitor and collect data from up to 200 channels at a speed of up to 1 Hz.

4.3.4 Equipment Evaluation and Calibration

The performance of the high temperature CRS device is evaluated to see if it meets the design requirements described in Chapter 4.2.

Seal Material

According to the specification from manufacturer (Table 4.2), both Viton and Karlrez will seal KCl fluid and hold pressure at 200 °C. In fact, Viton O-ring leaks after 18 days of high temperature and high salinity test. The Viton rubber degrades when exposes to KCl solution for long duration and no longer preserves its elasticity. The Viton rubber is not suitable for a test that lasts for a month.

Karlrez O-ring survives the 30-day heating period, but leakage is observed when temperature drops down to room temperature. Any rubber O-ring is designed to deform and to fill gap between flat surfaces, thus to block the fluid leakage. The deformation is quantitatively defined by a squeeze ratio (Equation 4.4). A recommend value is between 15% to 20% depending on the application (static or dynamic; rotational or linear movement) and the O-ring material. The center and bottom O-rings in Figure 4-3 are for static application. The squeeze ratio is about 18 %. The piston O-ring seal is for dynamic application, the squeeze ratio is about 12 % to reduce piston friction. The heating-cooling cycle thermally sets the O-ring to the geometry of the groove. The geometry of circular cross section becomes rectangular, thus the squeeze ratio becomes zero, the O-ring can no longer perform its duty (Figure 4-6). So after the cooling stage, before the reload stage, the high temperature CRS device is disassembled and new Karlez O-rings are installed to replace the "square ring". Care must be taken while replacing the O-rings to avoid specimen disturbance.

$$squeeze\% = \frac{Oring\ diameter - grove\ width}{grove\ width} \tag{4.4}$$

Piston Seal Dynamic Friction and Apparatus Compressibility

The Trautwein® CRS cell has a roller piston bearing to reduce friction, and a rubber diaphragm to seal the piston and the chamber. The piston can advance under its own weight. However, the high temperature CRS device has a higher piston friction. The piston (2.26 kg weight) does not advance under its own weight, so piston friction must be corrected in order to measure the vertical stress excerted on the specimen.

Figure 4-7 shows the net load vs. piston displacement. The net load is the difference between the axial force recorded by the load cell and the uplift force (ASTM D4186). The piston dynamic friction is 4.5 kg, the average of the blue and orange points. The points are recorded when piston is advancing and retracting at $1\%/hr$ strain rate. The piston dynamic friction to maximum axial stress ratio is 0.05 %. The piston friction is corrected in the data reduction program.

The apparatus compressibility is measured, and then modelled in Equation 4.5 (Figure 4-8). The procedures for how to calibrate the apparatus compressibility is describes in ASTM D4186 and Nordquist (2015).

$$disp. = D \times Load^{E} \tag{4.5}$$

Where disp. is the deflection of the apparatus in cm, load is the vertical total force in kg, D and E are fitting parameters, being 0.00022 and 0.470114.

Porous Stones

In this research, ceramic based porous stones fracture into pieces after 4-5 tests and must be replaced by new stones. New stones are likely to develop cracks in the top stone than in the bottom stone. Figure 4-9 shows cracked top stone. This top stone is only used for two tests. Both tests are loaded beyond 90 MPa. When stone fractures or cracks, the stone grain will mix with clay grain, and leads error to the void ratio calculation. To get an accurate test result, ceramic based stones should be used for two tests only, the maximum axial stress should be lower than 90 MPa.

4.4 Hydrothermal Reactor

Hydrothermal reaction is commonly used to induce mineral transformation in a laboratory environment. It has a steel chamber to contain slurry in a secondary container and cell fluid for pressurizing the slurry, a temperature control system to increase and maintain temperature, and pressure control system to regulate the cell pressure.

The device used in this research is manufactured by Col-Int Tech and modified to accommodate custom requirements (Figure 4-10).

The reactor is made of Cr-Ni-Ti 316 stainless steel to accommodate the high temperature and chemical corrosive environment. This reactor can tolerate temperature up to 350 °C and pressure up to 30 MPa. The cell pressure is injected externally by a PVA. The heating element attached to the bottom of the reactor provides energy to heat the sample. The tip of thermocouple is submerged in the fluid to measure the temperature inside the chamber. The tip length should be greater than five times of the thermocouple diameter to ensure enough contact area for heat transfer, thus guarantees the correct measurement of fluid temperature.

The reactor has a lid and a chamber. A graphite gasket is placed between the lip of the flanges (Figure 4-11). Six tension bolts link the lid and chamber together to be fluid tight. The graphite gasket is no longer needed if the researcher can ensure high tension (80N-M or more). The lips serve as a metal seal, they deform plastically to block the fluid pathway through the gap of the two flanges. In addition, proper surface cleaning is essential to the functioning of the metal seal.

The procedures for setting up the hydrothermal reactor is documented in Ge (2016).

4.5 Equipment for Measuring SSA

The total Specific Surface Area (SSA) is measured using Ethylene Glycol Monoethyl Ether (EGME) Method (Cerato & Lutenegger, 2002) in this study. Adams (2014) obtained total SSA using Methylene Blue (MB) spot test method (Santamarina et al.,

2002). The amount of MB used in the test replies on the researcher's visual judgment of the formation of a halo. Not only this visual judgment is subjective and prone to human error, but also the resolution of MB method is poor. EGME method measures the mass of the EGME retained by the fine grain clay and calculates the total SSA using Equation 4.6 assuming that a monolayer of EGME molecules covering the entire clay surface including the surface of interlayer space.

Figure 4-12 is the schematic diagram for the equipment used for measuring SSA. Aluminum tares are used to contain the mixture of EGME and clay. Researchers need to make sure every grain is submerged in the EGME liquid (tare 1 in Figure 4-13). $CaCl_2$ desiccant are placed in the cone flask and the desiccator. A vacuum pump ($>$ 635 mm (25 in.) Hg vaccum pressure) is attached to the cone flask to draw out the air.

$$SSA_{total} = \frac{W_a}{0.000286 \times W_s} \tag{4.6}$$

where SSA is in m^2/g, W_a is the weight of EGME retained by the clay in (g), W_s is the weight of dry clay (g), 0.00286 is the conversion factor, also the weight of EGME required to form a mono molecular layer on a square meter of surface.

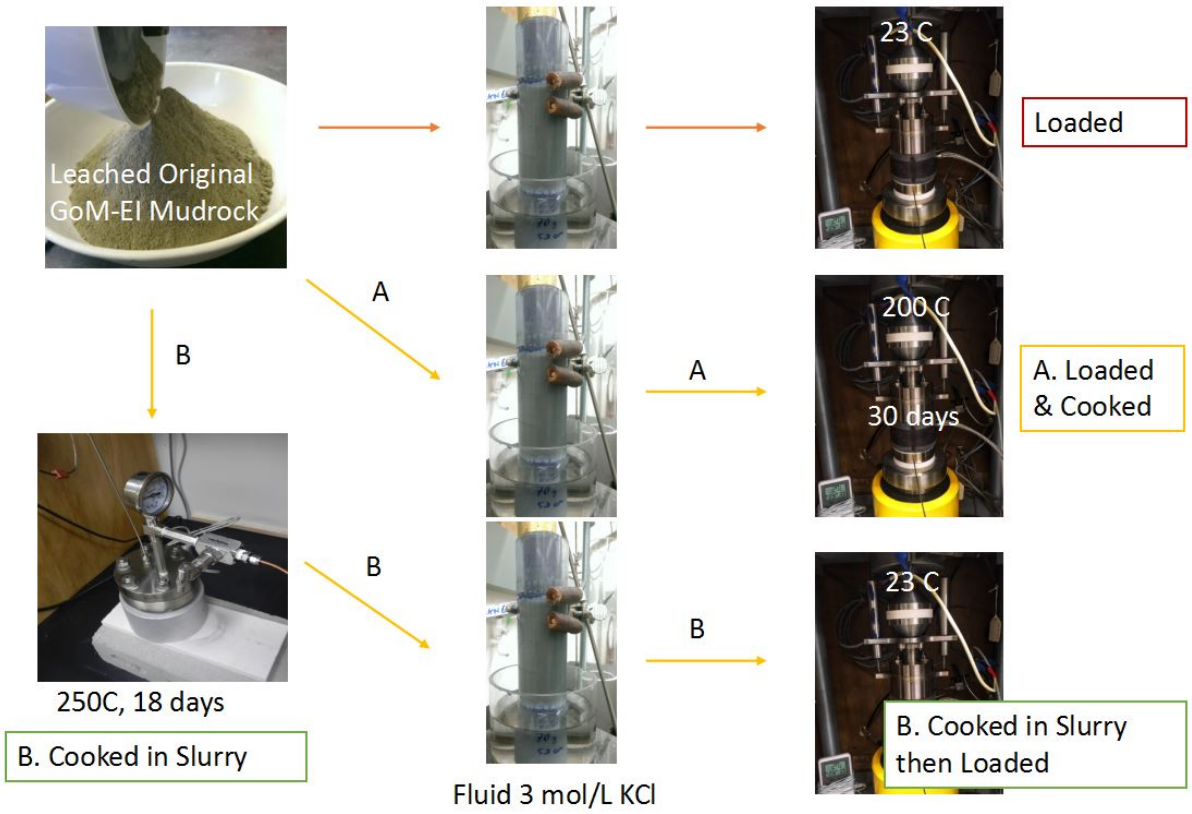

Figure 4-1: Experimental Procedures for Comparative Tests. The loaded test is the base line for smectitic mudrock, A and B are designed to measure the mechanical behavior of illitic mudrock.

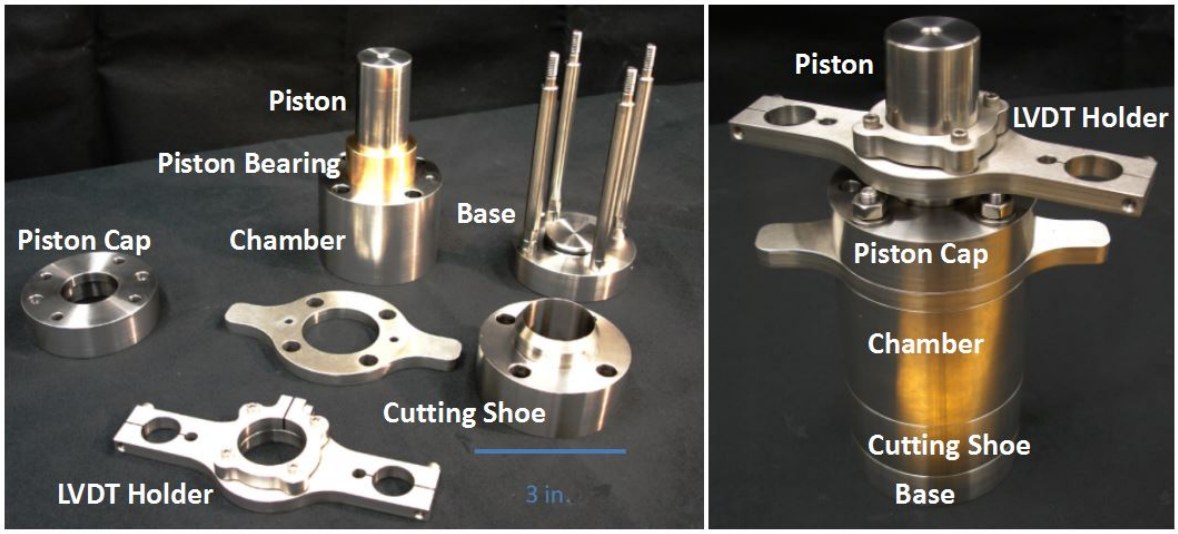

Figure 4-2: The High Temperature CRS Device Components

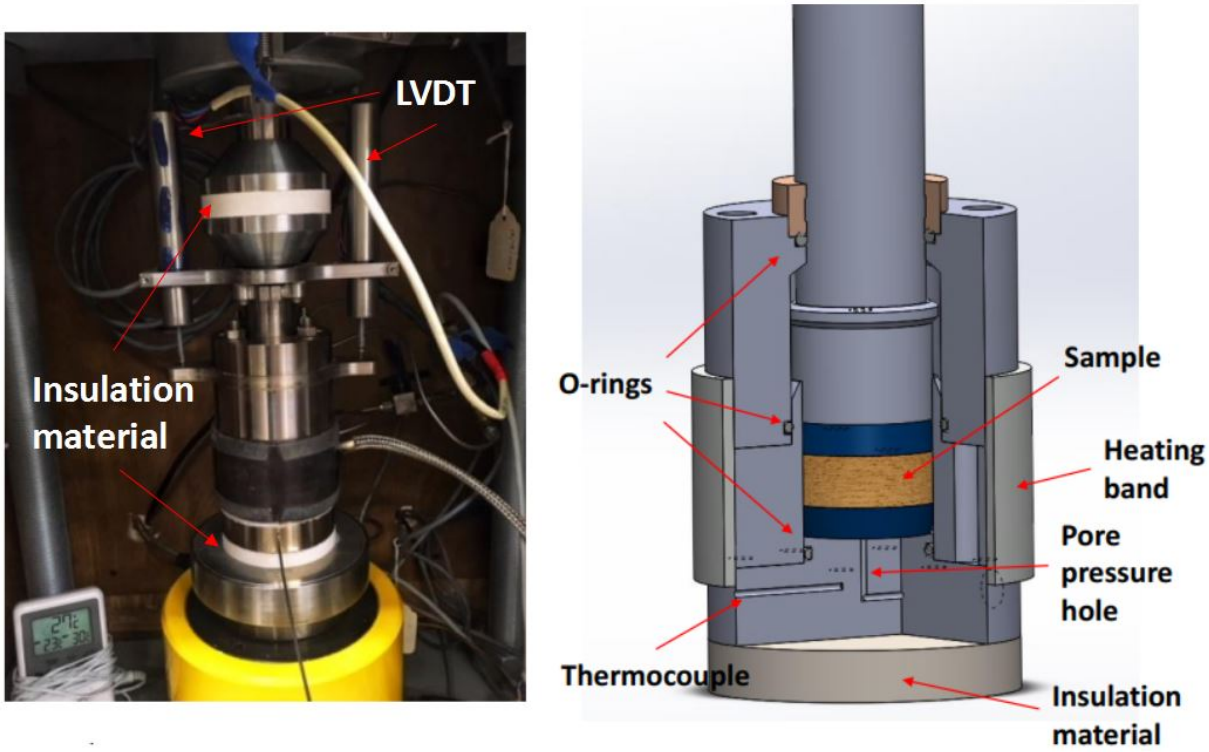

Figure 4-3: Cross Section of the High Temperature Device

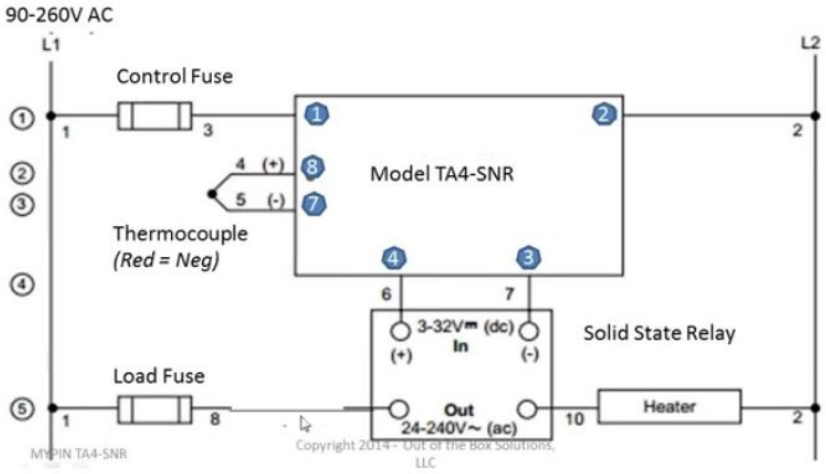

Figure 4-4: Schematic Diagram for Temperature Control System (photo courtesy of Out of Box Solution, LLC). Model TA4 and model TD4 wiring is the same.

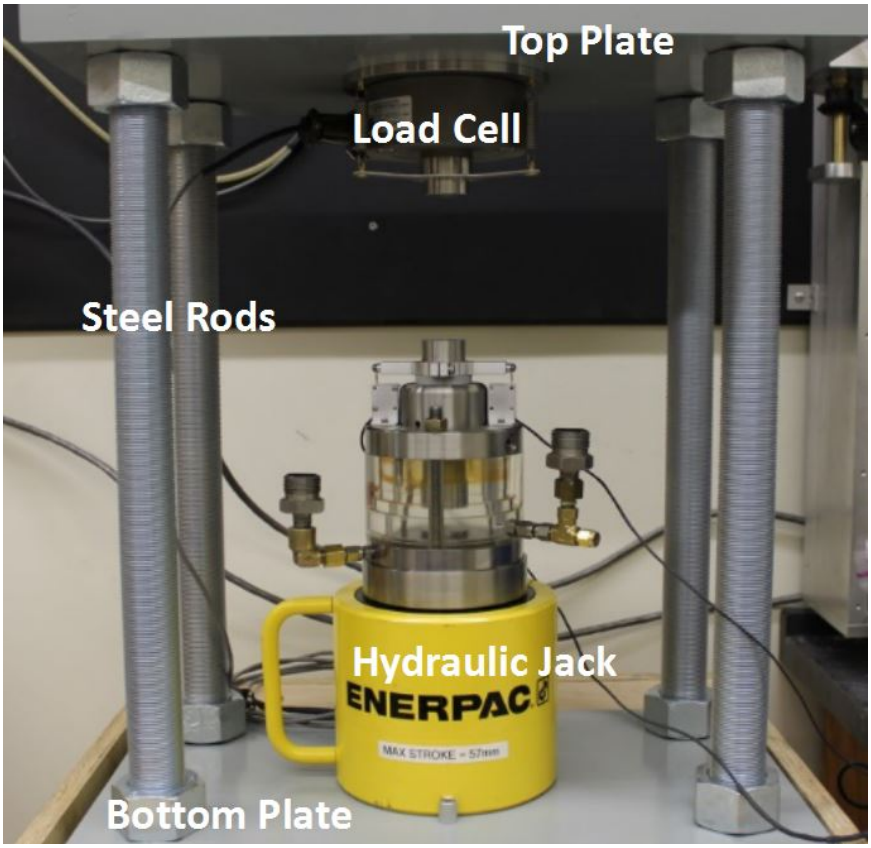

Figure 4-5: Load Frame for 100 MPa CRS Devices

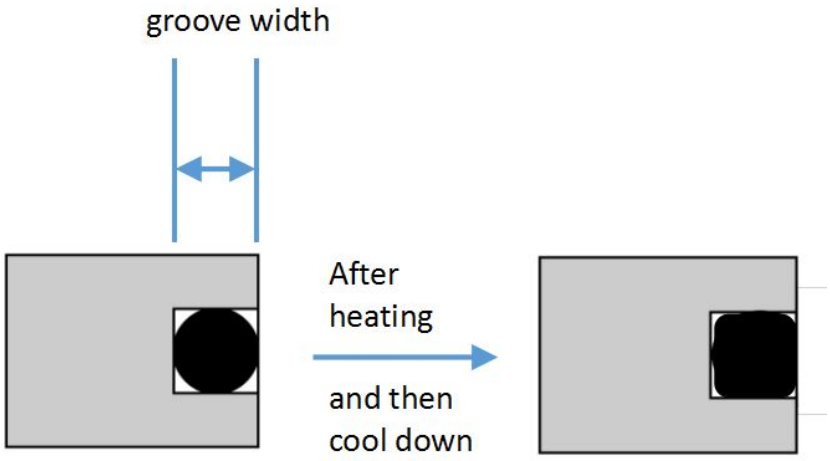

Figure 4-6: Thermal Set of the O-ring. The circular cross section of 0-ring changes to a rectangular shape after the heating-cooling cycle of the High temperature CRS device.

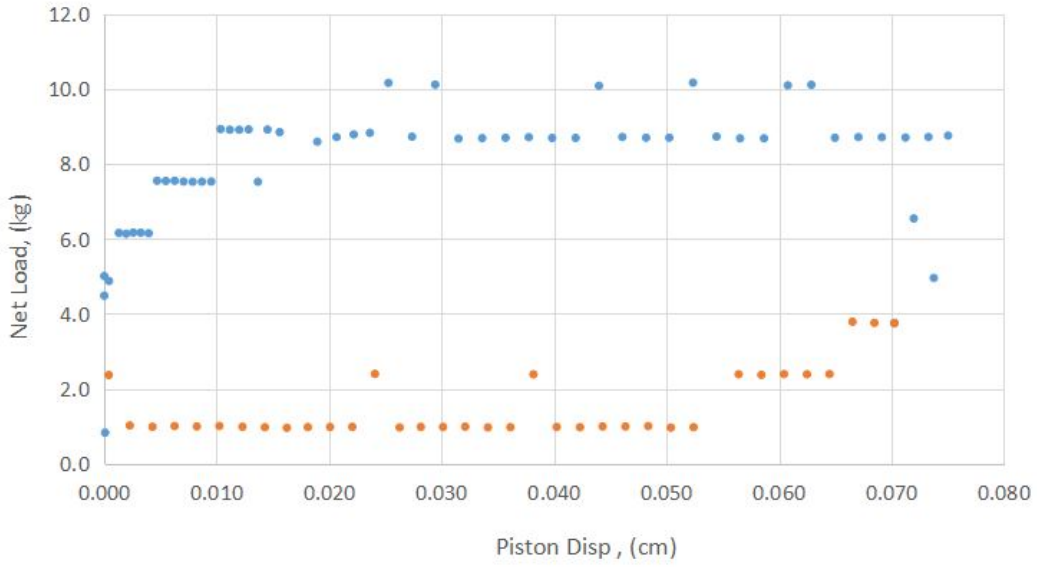

Figure 4-7: Net Load vs. Piston Displacement. Dynamic friction of the piston seal is determined by taking the average value of the load increment.

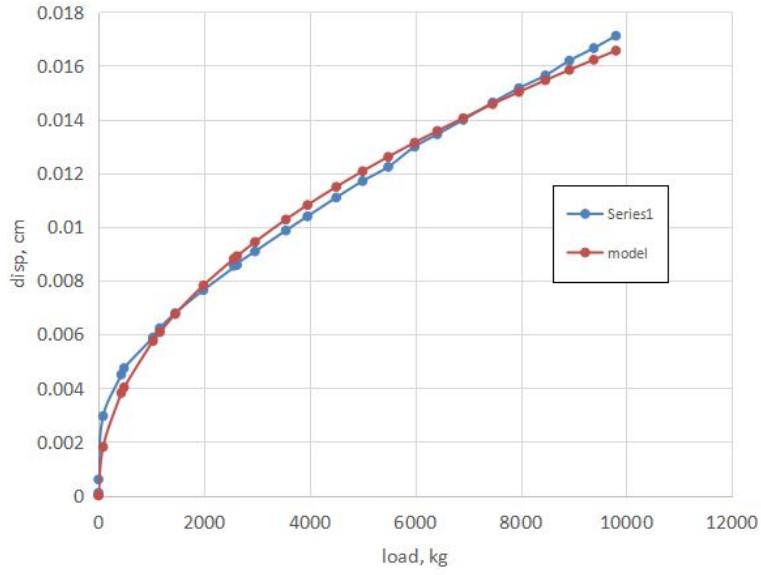

Figure 4-8: Apparatus Compressibility Curve. Blue dots are measured values, red dots are modelled using Equation 4.5

Figure 4-9: Cracked Porous Stone. The stone grains and specimen grains are difficult to differentiate.

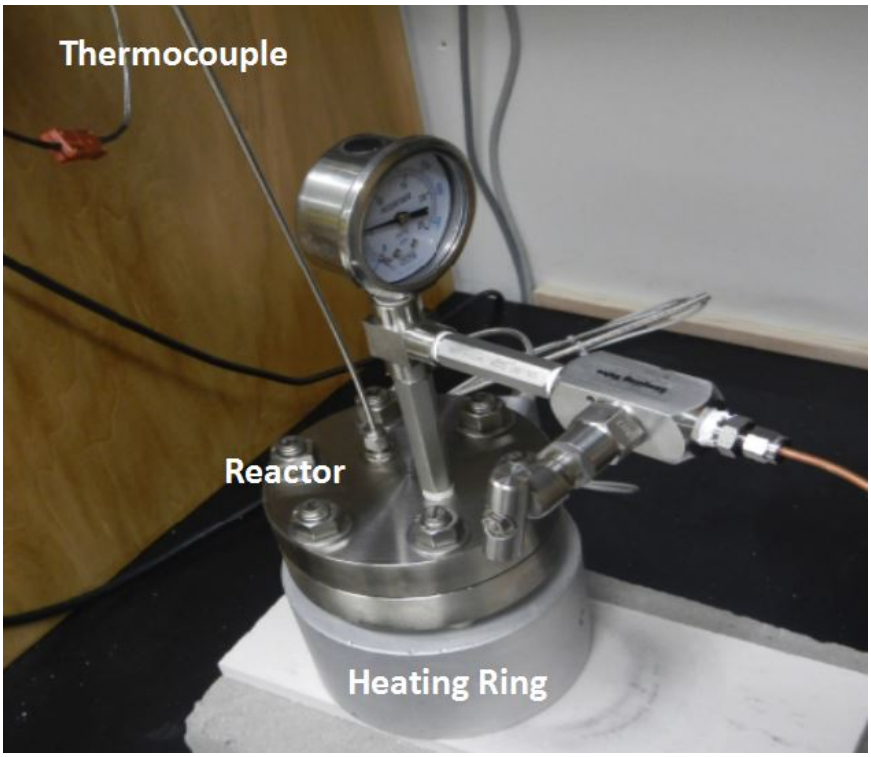

Figure 4-10: Hydrothermal Reactor used for cooking sample in slurry state

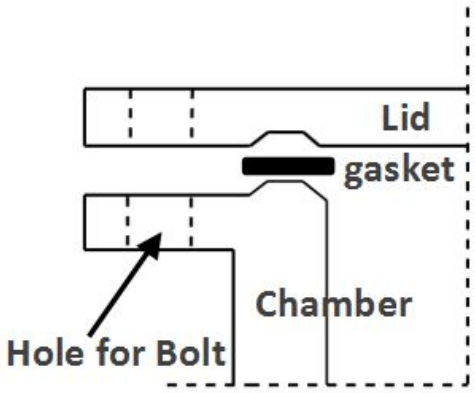

Figure 4-11: Cross Section of Seal for Hydrothermal Reactor

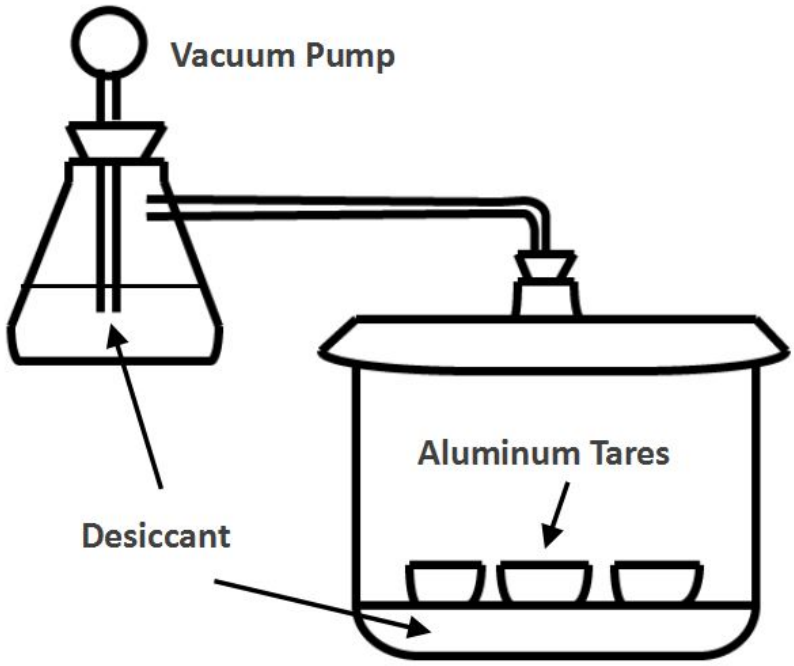

Figure 4-12: Equipment for Measuring Total SSA

Figure 4-13: Aluminum Tares with Mixture of EGME and Clay. In tare one, dry clay powder is totally submerged in EGME.

Chapter 5

Control Algorithm and Data Analysis for CRS Tests

In a CRS test, the ratio of excess pore pressure to total vertical axial stress increases exponentially with the increase of vertical load. For 100 MPa CRS devices, the expected pore pressure at the base of the equipment is enormous. The traditional strain rate control will no longer be suitable for this type of application. This chapter presents the algorithm to control the continuous loading of one dimensional compression of a mudrock specimen during the experiments. It has two stages. In stage I, the control program loads the specimen with constant rate of strain. In stage II, the control program decreases the strain rate, to achieve a balance between the generation and dissipation of the pore pressure, thus maintains a constant pore pressure gradient.

This chapter also shows the corresponding equations and theories for analyzing data collected in stage I and stage II. The hydraulic conductivity of the specimen is calculated using Wissa (1971)'s linear theory in stage I, and Lowe (1969)'s theory in stage II.

5.1 Control Algorithm

Two types of control methods are used to perform the uniaxial compression loading. The test starts with constant rate of strain (CRS) control or the displacement control, and then switches to constant gradient control or the pore pressure (PP) control when the pore pressure measured at the base of a CRS device reaches the target value. There are two pressure volume actuators (PVA) controlling vertical load and cell pressure. Cell pressure is maintained at a constant value throughout the test while vertical strain increment is controlled by feedback from displacement transducer during CRS control, and by feedback from pore pressure transducer during PP control.

The CRS chamber is bolted down to press on a rubber seal to prevent fluid leakage. The pore pressure accumulated at the base of the CRS cell exerts uplifting force on the chamber, thus compromises the down force applied on the rubber seal. To prevent the leakage of the fluid, the pore pressure should be smaller than designed pore pressure (PP) limit. In addition, there is a excess pore pressure gradient across the specimen, with the bottom being maximum, top being zero. A large gradient of pressure is not favorable. Considering the equipment limitation and test specimen condition, the combined control method is used for 100 MPa uniaxial compression tests.

Figure 5-1 shows the load vs. time and pore pressure vs. time relationship using the combined control method. Pore pressure increases linearly with time, when the vertical load is smaller than 200 kg; when in a transition zone from 200 kg to 600 kg, pore pressure increases exponentially with time (Figure 5-1). Then the control switches from CRS control to PP control once pore pressure reaches the target value (20 ksc for original RGoM-EI with $0g/L$ salinity pore fluid). The pore pressure stays at a constant value with time; load increases linearly with time. If the control algorithm does not switch to pore pressure control, the pore pressure will continue to increase exponentially and lift up the chamber. The target pore pressure value or PP limit is material specific as well, for the cooked specimens or higher permeability specimens, the PP limit is set to 15 ksc.

Figure 5-2 shows the change of strain rate with time. For RGoM-EI material or

high plasticity material, the strain rate starts with 0.6 $\%/hr$. The strain rate decays exponentially when control mode switches, it drops as low as 0.02 $\%/hr$. For Boston Blue Clay or low plasticity material, the starting strain rate is 1.0 $\%/hr$.

Figure 5-3 illustrates the logic and principles for how the control algorithm makes decisions. The key point is when and how transition between CRS control and PP control happens. In the CRS control stage (stage I), the code takes readings from transducers including pore pressure and displacement. It compares the measured strain with target strain, if the measured strain is smaller than target strain, the motor will move in positive direction to increase vertical load. In addition, the code constantly checks if pore pressure has reached the PP limit. If the answer is positive (Y) to the pore pressure check, then the control changes to PP control, the check condition also changes from comparing the strain to comparing the pore pressure. If the measured pore pressure is smaller than the target pore pressure, the motor will move to increase vertical load. The backwards motion of motor is prohibited by locking the relay of vertical loading motor.

Fahy (2014) also encounters the pore pressure problem. He uses a medium stress CRS cell (up to 40 MPa). He solves the problem by stopping the loading to let pore pressure dissipate for 24 hours (Figure 5-4). When pore pressure increases to 17 ksc, the loading is paused to allow time for pore pressure dissipation. Then when pore pressure drops to 12 ksc, the loading restarts until the specimen is loaded to the target stress level (40 MPa) . The disadvantage of this method is shown clearly in Figure 5-5 (the red circle), the permeability information is lost when a specimen is under a transient condition. A steady state factor F is used to determine whether or not the specimen is in a steady state (ASTM D4186, 2012).

$$F = \frac{(\sigma_v - \sigma_{v_0}) - (\Delta u - \Delta u_0)}{\sigma_v - \sigma_{v_0}} \tag{5.1}$$

where Δu is the excess pore pressure, σ_v is the total vertical stress on a specimen. The subscript 0 denotes the initial state when test just starts. If the F is above 0.4, transient condition is small enough to consider specimen in a steady state.

5.2 Data Analysis

Some introduction word, data analysis is based on CRS and PP In the previous section a combined control method is introduced to compress the specimen to a target stress level. The calculations for effective stress σ'_v for both controls are the same. The effective stress was defined by Wissa (1971) for a steady state condition as

$$\sigma'_v = \sigma_v - \frac{2}{3}\Delta u \tag{5.2}$$

5.2.1 Constant Rate of Strain Method

The calculation for hydraulic conductivity using CRS method is defined by equation 5.3. This equation is modifed after Wissa's linear theory for large strains. Wissa's original theory assumes a constant strain rate and small strain deformation. For the CRS tests conducted in author's lab, the strain can be as large as 50 %, Wissa's linear euqation is modified by Adams (2011) to accommodate large strain. Adams (2011) had conducted a systematic research on measuring hydraulic conductivity of fine grain soil using different theories. She also established that k calculated from CRS test using Wissa's linear theory is the same as k from constant head test.

$$k = \frac{\dot{\epsilon} H_0 H \gamma_w}{2\Delta u} \tag{5.3}$$

Where k is the hydraulic conductivity, $\dot{\epsilon}$ is the strain rate, H is the thickness of specimen at time t, H_0 is the thickness of specimen initially and γ_w is the density of water.

5.2.2 Controlled Gradient Consolidation Method

The formula for hydraulic conductivity using controlled gradient method is defined by equation 5.4 (Lowe et al., 1969).

$$k = \frac{c_v \gamma_w \alpha_v}{1 + e_0} \tag{5.4}$$

Where c_v is the coefficient of consolidation, α_v which defined by equation 5.5 is the coefficient of compressibility and e_0 is the void ratio at the start of test.

$$\alpha_v = -\frac{\partial e}{\partial \sigma'_v} \tag{5.5}$$

The c_v is computed as equation 5.6, it is modifed after Lowe's theory for large strains.

$$c_v = \frac{\partial \sigma_v}{\partial t} \frac{H_0 H}{2\Delta u} \tag{5.6}$$

where t is time.

5.3 Reduction Code for Analyzing the Data

The raw test data are analyzed using an Excel spreadsheet and Matlab program. The Excel spreadsheet converts the transducer voltages recorded by the central data acquisition system into engineering values of displacement, axial load, cell and pore pressures, which are in turn used to compute void ratio, vertical effective stresses, permeability and coefficients of consolidation.

Matlab codes and instructions for using the codes are attached in Appendix B.

5.4 Symbol List

1. σ_v = applied total vertical stress
2. u = pore pressure
3. H_0 = thickness of specimen initially
4. t = time
5. c_v = coefficient of consolidation
6. Δu = hydrostatic excess pressure at base
7. H = thickness of specimen at time t
8. σ'_v = vertical effective stress

9. e_0 = initial void ratio
10. $\dot{\epsilon}$ = strain rate
11. γ_w = density of water

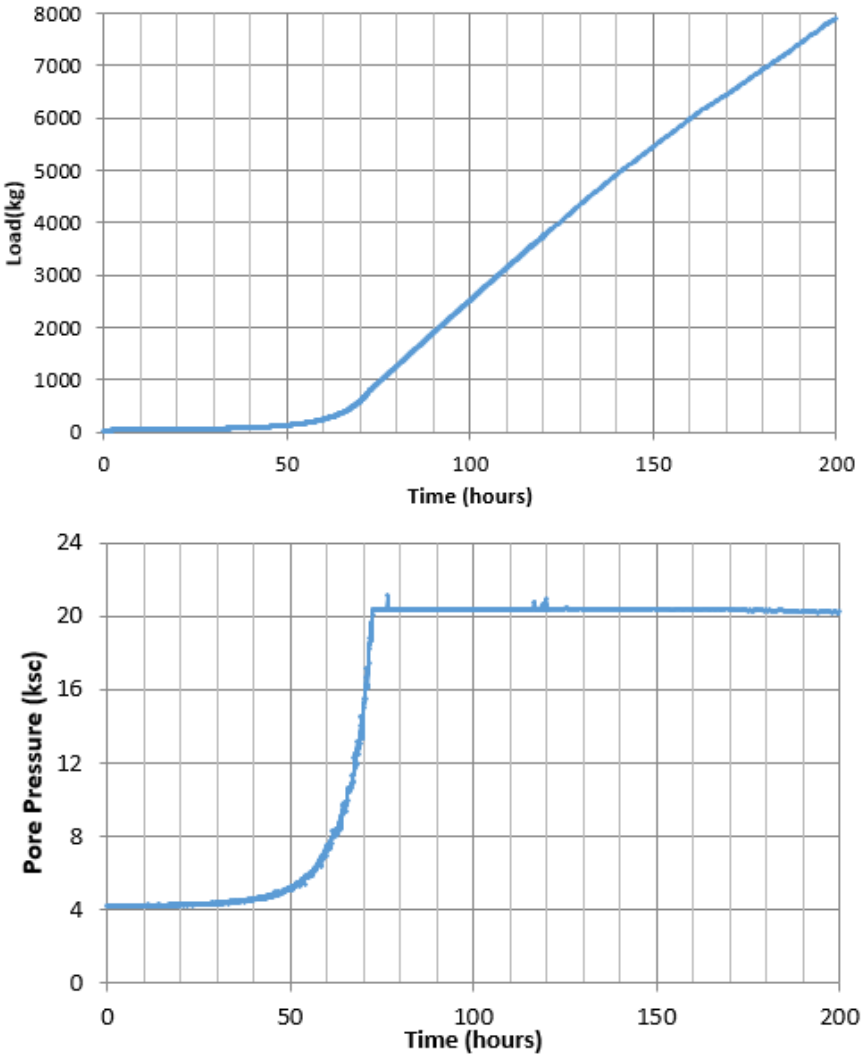

Figure 5-1: Combined Control Method Data from TCRS006

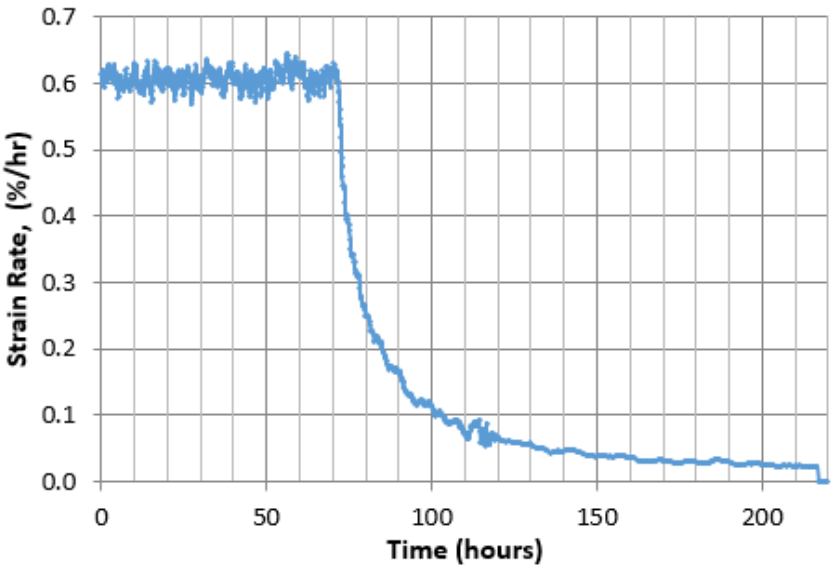

Figure 5-2: Strain Rate Changes with Control Method. In stage I, the strain rate maintains at 0.6 $\%/hr$. In stage II, the strain rate decays exponentially.

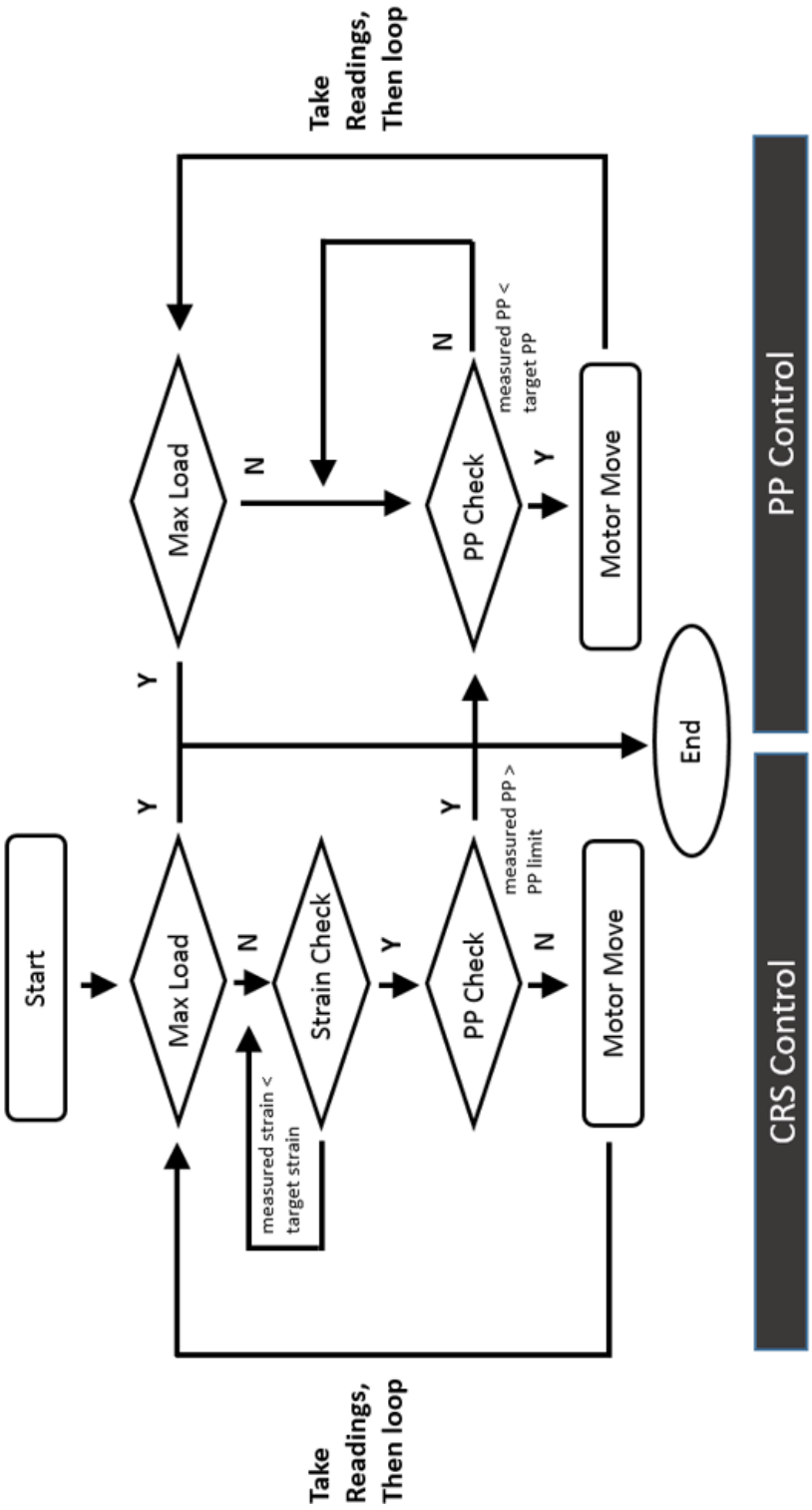

Figure 5-3: Flow Chart of Vertical Load Control Algorithm used to Perform Uniaxial Loading Test.

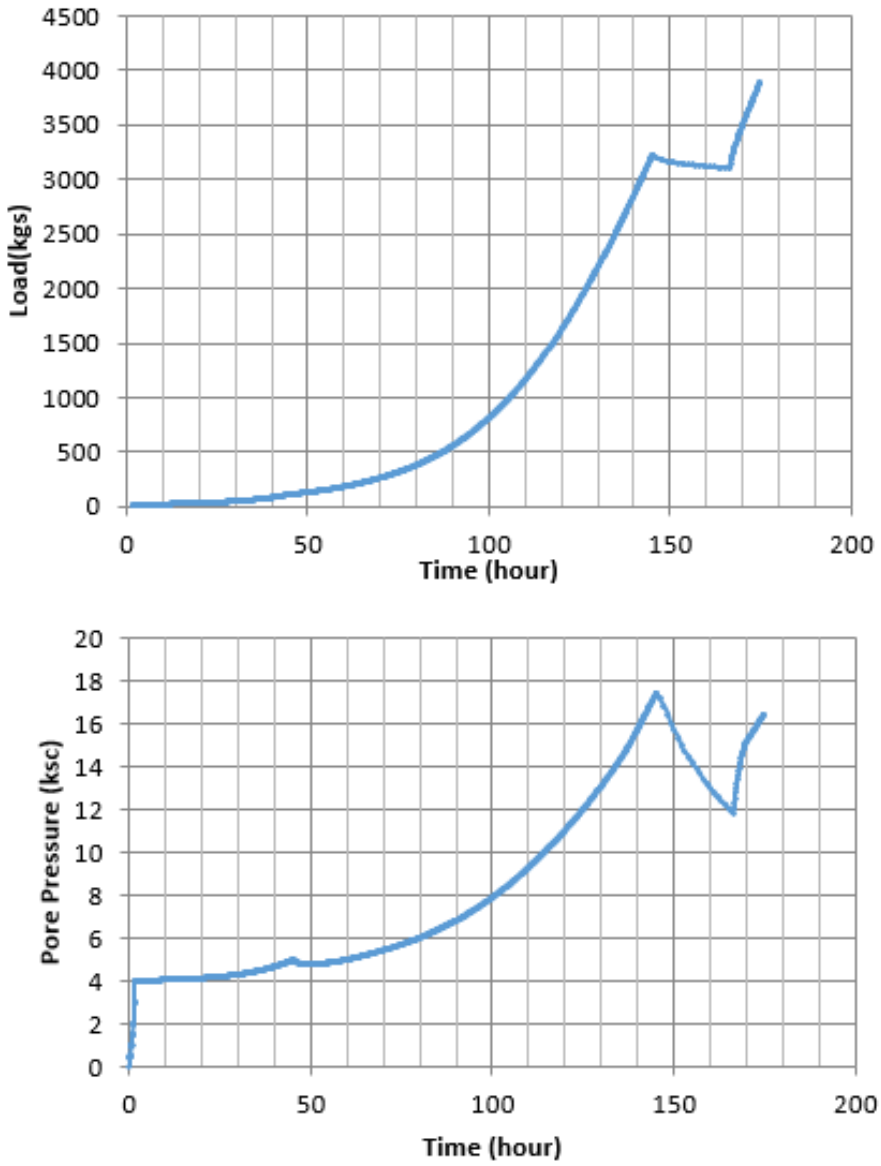

Figure 5-4: Results from CRS Test using a Cycle of Constant Load to Reduce Pore Pressure. (Fahy 2014)

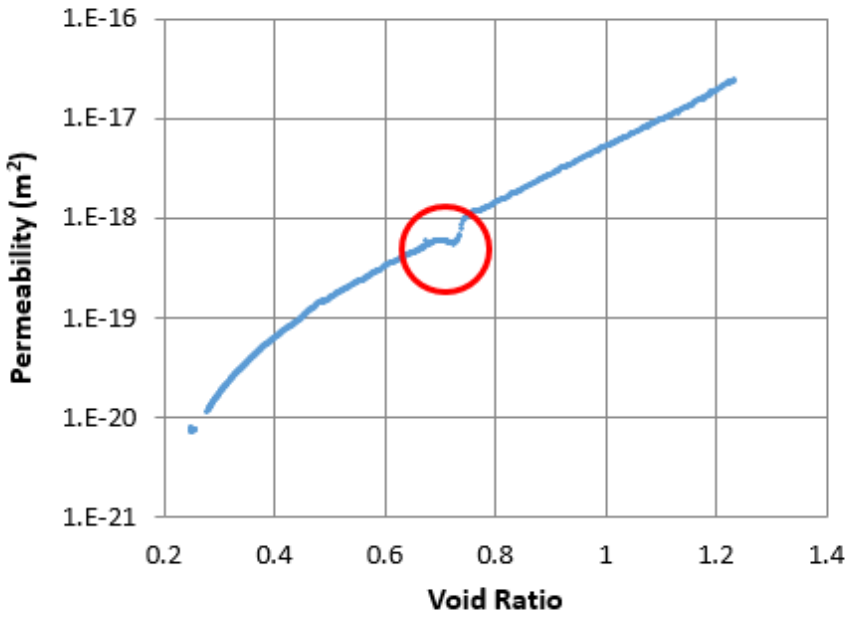

Figure 5-5: Permeability Result from CRS1370 by Fahy (2014). The red circle shows missing data due to a transient condition.

THIS PAGE INTENTIONALLY LEFT BLANK

Chapter 6

Results and Interpretation

This chapter summarizes the changes in compression and permeability behavior due to smectite-to-illite mineral transformation.

Chapter 2 provides a review of the laboratory methods for inducing smectite-to-illite transformation. The hydrothermal reaction is the most common method for transforming clay mineral, but this method usually produces a slurry in small quantity; the alternative is a triaxial or CRS cell with heating ability. This study presents result from both methods.

The cooked in slurry illitic mudrock (referred to as illitic mudrock B in the following sections) has different behavior than the mudrock cooked under effective stress (referred to as illitic mudrock A in the following sections). The mineral transformation does not greatly alter the compressibility of the mudrocks, but the permeability of illitic mudrocks increases by a significant amount compared with that of the smectitic mudrock.

The design of the reaction temperature and time is based on the understanding of the reaction speed of GoM-EI material. The author conducted a systematic study of hydrothermal reaction, by varying the temperature from 150 $^{\circ}C$ to 300 $^{\circ}C$ (Ge, 2016).

Figure 6-1 summaries the mineralogy results from author's master thesis. All tests were cooked for 18 days using a hydrothermal cooker. The mineralogy result shown in last column was cooked for 29 days. Not until the temperature is up to 200 $^{\circ}C$

does a significant increase in transformation occur. The 250 $°C$ and 18 days condition is selected for hydrothermal reaction method to induce a mineral change that could be observed on its mechanical properties.

In additional to the hydrothermal cooker, high temperature CRS device is used to transform mudrock with effective stress. The 200 $°C$ is selected for the high temperature CRS device due to the device limitation: the temperature needs to be smaller than the service temperature of the seal. In order to achieve similar degree of illitization for both methods and considering that the reaction speed at 200 $°C$ is smaller than that of the 250 $°C$, the reaction time for high temperature CRS device is extended to 30 days.

6.1 The Smectitic Mudrock

The smectitic mudrock uses the original leached GoM-EI as source material, which has 42 % of I/(I+S). This smectitic mudrock test sets the baseline for the smectitic mudrock, in order to compare with illitic mudrocks.

Compression Behavior

The test on smectitic mudrock was conducted with the combined control strategy. The test started with 0.6 $\%/hr$ strain rate as a CRS test, when the pore pressure reached 2 MPa, the computer program proceeded to stage II constant gradient control at a effective stress of 20 MPa. The strain rate dropped exponentially from 0.6 to 0.1 $\%/hr$ (Figure 6-2). It took 136 hours to finish the test. The CRS stage I lasted for 100 hours, including 1 day of power outage. The stage II lasted for 36 hours. During the entire test, the pore pressure was below the equipment pressure limit. This high plasticity mudrock was safely compressed to 100 MPa.

Compression curves are usually plotted as a fabric density parameter versus vertical effective stress. The fabric density parameter can be represented with strain (ϵ), void ratio (e), or porosity (n). Strain is the ratio of deformation of a specimen to the initial specimen height; void ratio is the volumetric ratio of voids to solids; porosity

is the ratio of void volume to total volume.

Most geotechnical engineers describe the compression behavior of a soil specimen in e - $log(\sigma_v^{'})$ space. In general, when the stress level is low, the compression curve demonstrates good linearity in the e - $log(\sigma_v^{'})$ space. However, over a wider stress range, n - $log(\sigma_v^{'})$ plot is more linear for high plasticity materials (Casey, 2016).

The compression behavior of the smectitic mudrock is plotted in e - $log(\sigma_v^{'})$ and n - $log(\sigma_v^{'})$ space respectively in Figure 6-3. The void ratio compression curve (blue line) has a convex profile. The void ratio starts at about 1.6 and decreases to 0.27 at 89 MPa. The power outage did not affect the compression curve, but there is a small stress drop at 0.2 MPa. The preconsolidation pressure observed from the compression curve (0.1 MPa) is consistent with the applied resedimentation stress. When the effective stress is greater than 0.1 MPa, the mudrock is in the normally consolidated (NC) range.

The porosity compression curve (orange curve) shows good linearity in the NC range ($>$ 0.1 MPa). A log-linear regression is fit to the linear portion of the porosity curve from 0.3 MPa to 100 MPa using equation 6.1.

$$n = -0.1387 \times log(\sigma_v^{'}) + 0.4849 \tag{6.1}$$

with a R^2 of 0.9997. The n - $log(\sigma_v^{'})$ model accurately describes the NC behavior over the entire NC stress range.

In the later sections, the compression results are presented from 0.1 MPa to 100 MPa, because all specimens were resedimented to 0.1 MPa, the compression behavior is similar in the overconsolidated range.

Permeability Behavior

The permeability of the smectitic mudrock is calculated using Wissa's linear theory adjusted for large strain in stage I CRS control . Lowe's equation which is also adjusted for large strain is used to calculate the permeability in stage II PP control.

The permeability data for the smectitic mudrock are shown in log(k) - n space and

log(k) - e space in Figure 6-4. The void ratio permeability line (dark orange curve) has a concave profile. Permeability curve displays better linearity in log(k) - n space than in log(k) - e space[1]. This is consistent with the Geofluids database. Over a large stress range, permeability of mudrocks is more linear in the porosity space.

The permeability of the smectitic mudrock starts around a value of 10^{-16} m^2 at a porosity of 0.6, decreases to 10^{-20} m^2 at a porosity of 0.22. A log-linear equation is fit to the linear portion of the curve from a porosity of 0.23 to 0.53 using equation 6.2 in the format used by Casey (2014).

$$log(k) = \gamma(n - 0.5) + log(k_{0.5}) \tag{6.2}$$

Where $k_{0.5}$ is the permeability value at a porosity, n= 0.5, γ is the slope of the permeability trend. $log(k_{0.5}) = -17.15$, $\gamma = 11.33$, $R^2 = 0.990$.

6.2 The K- saturated Smectitic Mudrock vs. the Na-saturated GoM-EI

The K smectitic mudrock discussed in the previous section is resedimented and compressed in 223.5 g/L KCl solution. However, in a natural geological setting and for most of the Geofluids tests, the pore fluid is NaCl solution. To relate the compression and permeability behavior of the K-saturated vs. Na-saturated smectitic mudrock, one CRS test with 64 g/L sea salt solution, conducted by Fahy (2014), is selected to compare with the K smectitic mudrock behavior in this research. The CRS test is labelled Na smectitic mudrock (CRS1364) in Figure 6-5 and 6-6. The Na-saturated specimen was resedimented to 0.1 MPa and compressed to 40 MPa with 64 g/L sea salt solution.

Figure 6-5 compares the compression behavior of the two mudrocks. The K smec-

[1]During the test, a power outage occurred, which resulted missing permeability data from a porosity of 0.53 to 0.57. In that porosity range, the illitic mudrock A has not been transformed, it is identical to the one used in this test. The permeability data from the illitic mudrock A overlays on the baseline test to fill the permeability data gap for the smectitic mudrock.

titic mudrock starts from a porosity of 0.6 to 0.21 over a stress range of 0.1 to 100 MPa. The initial porosity at 0.1 MPa for the Na smectitic mudrock is slightly lower than that of the K smectitic mudrock. The porosity reduces to 0.21 at 40 MPa. Both compression curves are log linear in the n - $log(\sigma_v^{'})$ space. The compression curve of the Na smectitic mudrock is parallel to K smectitic mudrock with a slight offset.

Figure 6-6 shows the permeability behavior of the two mudrocks. The permeability of the K smectitic mudrock reduces by four orders from 10^{-16} to 10^{-20} m^2 as porosity decreases from 0.6 to 0.2. The permeability value of Na smectitic mudrock is very similar to K smectitic mudrock, it overlaps that of K smectitic mudrock from a porosity of 0.6 to 0.4. At the low porosity, two permeability curves have a slightly difference slope, but the ratio of values are $\pm$ 2.

6.3 The Effect of Smectite-to-illite Transformation

Previous section sets the baseline for smectitic mudrock. This section discusses the effect of the mineral transformation in the following subsections:

1. Permeability Behavior Change
2. Compression Behavior Change
3. Mineral Composition Change
4. Specific Surface Area Change
5. Fabric Analysis and Interpretation

The illitic mudrocks are generated by two different methods: A. cooking with effective stress at elevated temperature using the high temperature CRS device; B. cooking in slurry state without effective stress in the hydrothermal cooker.

Although the methods are different, by selecting the appropriate temperature and time combination, it is possible to achieve similar degrees of illitization for the illitic mudrock A and B. The illitic mudrock A has around 84 % of I/(I+S). The illitic mudrock B has 84 % of I/(I+S). The pore fluid for both illitic mudrocks are 3 mol/L KCl solution; the illitic mudrock A was cooked at 200 $^{\circ}C$ for 30 days, while the illitic mudrock B was transformed at 250 $^{\circ}C$ for 18 days.

Smectitic mudrock required a combination control algorithm to reach 100 MPa effective stress. The illitic mudrocks A & B were tested with CRS control because the pore pressure never reached the CRS device limit value. Table 6.1 summaries the reaction conditions for illitic mudrocks, including stress state, salt concentration, temperature and time.

Table 6.1: Reaction Conditions for Illitic Mudrocks

	Condition	KCl, mol/L	Temp., $°C$	Time, days
A	$\sigma' = 5$ MPa	3	200	30
B	Slurry	3	250	18

6.3.1 Permeability Behavior Change

The illitic mudrock B and smectitic mudrock display similar permeability in the high porosity range (Figure 6-7). The difference in permeability amplifies with decreasing porosity. The permeability of the illitic mudrock reduces by three orders from $10^{-16}m^2$ to $10^{-19}m^2$, while the smectitic mudrock reduces by four orders from $10^{-16}m^2$ to $10^{-20}m^2$. The permeability values of the illitic mudrock A and B are similar at a given porosity from a porosity range of 0.22 to 0.32, they are both over a magnitude greater than that of the smectitic mudrock at a porosity of 0.25. The permeability of the smectitic mudrock is greatly increased by the mineral transformation.

A log-linear equation is fit to the linear portion of the permeability curve of the illitic mudrock B using equation 6.3.

$$log(k) = \gamma \times (n - 0.5) - log(k_{0.5}) \tag{6.3}$$

Where $log(k_{0.5})$= -16.80, γ = 8.983.

The permeability ratio r_k is the k of the illitic mudrock B in equation 6.3 over that of smectitic mudrock in equation 6.2. r_k increases from 2 to 10 (Figure 6-8) as the porosity reduces.

Mesri and Olso's (1971) tests show that illitic material has a higher permeability

than the smectitic material at a given porosity (Figure 6-9). The permeability curves for pure smectite and pure illite are in parallel when porosity is smaller than 0.8. Pure smectite and pure illite are evenly apart by 2 orders over the porosity range of 0.4 to 0.8. The observation from this study shows that the illitic material and smectitic material share similar permeability at high porosity. So the direction in change is consistent with the literature but the magnitude is much less than observed with pure mineral. As the porosity reduces, the permeability curves diverge rather than run in parallel to each other in Mesri and Olso's (1971) case. This is either due to the mixed nature of the material or the fact that both the smectite and the illite are mixed layer.

Coefficient of Consolidation Behavior

Following the discussion of permeability comparison, the coefficients of consolidation (C_v) for three materials are plotted on a $log(C_v)$-$log(\sigma_v^{'})$ scale. C_v indicates the rate of dissipation of pore pressure. With a lower C_v, more time is required to achieve 100% consolidation.

In this study, C_v starts about the same value for smectitic and illitic mudrock B (0.01 cm^2/s). C_v values for all three mudrocks continue to decrease as stress increases, but the decreasing rate reduces when the effective stress passes 1.5 MPa for the smectitic mudrock and the illitic mudrock B and 20 MPa for the illitic mudrock B. C_v for smectitic mudrock keeps dropping about one magnitude to 10^{-4} cm^2/s after 1 MPa, while C_v for illitic mudrock A and B decreases much slower compared with that of smectitic mudrock. C_v for illitic mudrock A overlays with illitic B from 20 to 90 MPa. It should be noted that after 20 MPa effective stress, the cluster of red dots for C_v of the smectitic mudrock becomes concentrated, forming a well defined line. In the baseline test, the control program switches mode to PP control at 20 MPa effective stress. The smooth control on the loading generates a well define C_v curve (Figure 6-10).

6.3.2 Compression Behavior Change

Effect of Transformation on Illitic Mudrock A

Following the steps described in Chapter 4.1, the specimen was compressed uniaxially to an effective stress of 5 MPa (Figure 6-11), the void ratio is about 1.49 at 0.1 MPa. reduces to 0.65 at 5 MPa. This portion of the compression curve is identical to the baseline line behavior.

Then the test was set to hold constant stress at room temperature for 5 days to measure the secondary compression rate.

The temperature was elevated to 200 °C and maintained constant at 200 °C for 30 days to induce smectite-to-illite transformation. During stage 2 and stage 3, the smectitic mudrock went through mineral transformation and secondary compression.

After 30 days of cooking, the device was cooled down to room temperature. The heating and cooling cycle thermally set the O-ring to a square cross-section ring which was no longer able to seal the fluid. The seal leaked once the device was at room temperature. Therefore, the high temperature CRS device was disassembled to replace the O-rings. The high temperature CRS device was reassembled and loaded to 100 MPa. The specimen was kept in the cutting ring throughout this process. The device was taken apart carefully by mechanical jack system to minimize disturbance. The LVDTs zero positions were taken twice with a dummy specimen before the trimming procedure and after the test to make sure the strain zero position is the same before and after the replacement of O-rings.

The compression curve of the illitic mudrock A follows different sections in Figure 6-11. In stage 1, the specimen (green line) is loaded from 0.1 to 5 MPa; in stage 2, 3 and 4, the compression curve follows three arrows at constant stress; in stage 6, the specimen (purple line) is loaded to 100 MPa.

In stage 1, the illitic mudrock A has not gone through transformation. The green compression curve overlaps the red smectitic mudrock. In stage 2, 3 and 4, the effective stress holds constant, the void ratio reduces straight down. Results about stage 2, 3 and 4 are discussed in Section 6.4

After changing O-rings, the converted illitic mudrock A is at very low effective stress, the compression curve is very stiff during reloading up to an effective stress of 16 MPa. Beyond 16 MPa, the illitic mudrock A is in the normally consolidated range. This behavior is comparable to reloading an OCR material.

The preconsolidation stress is determined using strain energy method (Germaine & Germaine, 2009). The energy or the work is calculated by summing the average force for each increment multiplied by the natural strain increment. The natural strain is deformation over the current volume of a specimen. Figure 6-12 shows that the $\sigma_p^{'}$ = 16 MPa. For the smectitic mudrock, the $\sigma_{vc}^{'}$ is 13.3 MPa for a void ratio of 0.49. The preconsolidation stress increases by 2.7 MPa over the effect of mechanical compression. The maximum consolidation stress for the illtic mudrock A is 5 MPa. So the OCR for the illitic mudrock A:

$$\frac{\sigma_p^{'}}{\sigma_{vc}^{'}} = \frac{16}{5} = 3.2 \tag{6.4}$$

There are several reasons for the illitic mudrock A to develop an increased preconsolidation stress. First of all, the mudrock underwent extensive secondary compression for more than a month at 5 MPa. Secondly, it was exposed to elevated temperature, thus causing thermal hardening. Thirdly, it experienced mineral transformation as well. The mineral dissolution-precipitation process reduces porosity and leads to an increase in quasi-preconsolidation stress. Either one or all of the three may contribute to the quasi-preconsolidation effect of the mudrock. When the stress increases beyond 16 MPa, the OCR effect goes away. The compression curve of the illitic mudrock A converges with the smectitic mudrock.

Comparison of the Compression Behavior

The compression results of the smectitic mudrock and illitic mudrocks are plotted in n - $log(\sigma_v^{'})$ space in Figure 6-13 and Figure 6-14. The initial porosity of the illitic mudrock B is 0.64 at 0.1 MPa, and the initial porosity of the smectitic mudrock is 0.6 at 0.1 MPa. All of the speicmens were resedimented to 0.1 MPa. As effective stress

increases, the illitic mudrock B and smectitic mudrock start to converge. The illitic mudrock B and smectitic mudrock compression curves intersect at 25 MPa.

The virgin compression behavior is strongly influenced by the mineralogy of the specimen at low stresses. According to Meade (1966) and Mondol et al. (2007), the order of porosity ranking at a given effective stress is: smectite (montmorillonite) > illite, but the results from Author's experiments are in reverse order. The illitic mudrock B has a higher porosity compared with the smectitic mudrock when $\sigma_v^{'} > 25$ MPa, the difference in porosity diminishes with increasing stress level.

Figure 6-14 is the zoom-in view of Figure 6-13 from 10 to 100 MPa. The illitic mudrock A is very stiff in the overconsolidated range before 16 MPa. The illitic mudrock A is less dense than smectitic mudrock. As stress increases, the illitic mudrock A converges with the smectitic mudrock. The illitic mudrock B reverses order with the smectitic mudrock at $\sigma_v^{'} = 25$ MPa. The illitic mudrock A is higher in porosity than the illitic mudrock B from a stress level of 20 to 100 MPa. The compression curves of illitic mudrock A and illitic mudrock B are relatively in parallel with each other.

Compressibility Behavior

The compressibility or the coefficient of volume change in the vertical direction (m_v) indicates the stiffness of a material (equation 6.5). It is calculated as the change in strain over change in vertical effective stress for the uniaxial compression test. A smaller value of m_v indicates a stiffer material.

$$m_v = \frac{\Delta\epsilon}{\Delta\sigma_v^{'}} \tag{6.5}$$

Figure 6-15 plots log (m_v) vs. n. The m_v value changes over 3 orders of magnitude from 100 to 0.1 %/MPa. The compressibility curves are essentially log linear over the porosity range of 0.2 to 0.6. The compressibility of smectitic mudrock is slightly higher than the illitic mudrock B at high porosity from 0.6 to 0.35, indicating that illitic mudrock is stiffer at a given porosity. As the porosity reduces, the compressibilities

of both mudrocks converge. The compressibilities of the smectitic mudrock and illitic mudrock A & B are almost identical when they are compressed to low porosity from 0.2 to 0.33 (Figure 6-16).

Figure 6-17 shows log (m_v) vs. log ($\sigma_v^{'}$). The compressibility difference is small, with smectitic material being slightly stiffer than the illitic mudrock. The noticeable divergence in the compressibility shown in porosity space becomes negligible. Figure 6-18 is the zoom-in view of Figure 6-17. The compressibility of the illitic mudrock A is slightly higher than the smectitic mudrock and illitic mudrock B in the log (m_v) vs. log ($\sigma_v^{'}$) space, whereas in the log (m_v) vs. n space, compressibility for all mudrock are almost identical at high stress.

Table 6.2: Summary of Smectitic vs. Illitic Tests

	Smectitic	Illitic	
		A	B
Test #	TCRS007	CRS1531	TCRS008
Porosity at 0.1 MPa	0.60	0.60	0.64
Final Porosity	0.21	0.21	0.20
Final Stress, MPa	89	93	93

6.3.3 Mineral Composition

The mineral composition for the smectitic mudrock, and illitic mudrock A and B is shown in Figure 6-19 and Table 6.3. The samples were send to Shell for X-ray diffraction (XRD) analysis. The XRD patterns were analyzed by Dr. Ruarri Day-Stirrat.

The smectitic mudrock has 43% smectite, 31% I/S and 13% illite. In the I/S mixed layer phase, the illite to smectite ratio is 79:21. The I/(I+S) ratio, which is a function of these three phases including the discrete illite, discrete smectite and I/S (equation 2.1), provides a single parameter to evaluate the degree of transformation.

From the mineralogy analysis, the illite content in both illitic mudrocks increases significantly. The discrete smectite in the illitic mudrock A and B decreases from 43% to zero, while the I/S increases from 31% to 66.4% and 85% respectively. The discrete

illite phase in the illitic mudrock B stays the same compared with the smectitic mudrock. The discrete illite phase in the illitic mudrock A increases from 13% to 29.6%.

Although the value for degree of illitization I/(I+S)% doubles from 42% to 84% in both illitic mudrocks, the values for illite and I/S are different. The illitic mudrock B has a higher number in I/S, but less discrete illite than the illitic mudrock A.

The formation of the discrete illite requires two steps. 1. The discrete smectite transforms to I/S phase. When the discrete smectite reduces, the I/S increases. 2. When the illite% in the I/S reaches unity, it precipitates as discrete illite. The illitic mudrock B is still in the first step. The discrete illite is the same as the smectite mudrock. The illitic mudrock A is in the second step. There is a 16.6% increase in the discrete illite.

The conversion of discrete illite to I/S causes increase in permeability, a higher porosity at low stress, and a lower porosity at high stress when comparing the illitic mudrock B with the smectitic mudrock.

The conversion of I/S to discrete illite leads no change in permeability, but slightly stiffens the structure when comparing the illitic mudrock A with the illitic mudrock B.

Table 6.3: Mineral Composition for the Clay Fraction

	Illite	Chlorite	Kaolinite	Smectite	I/S	I/S		I/(I+S)	Reichweite
						I	S		
Smectitic	13	4	9	43	31	79	21	42	R0
Illitic A	29.6	1.5	2.5	0	66.4	77	23	84	R1
Illitic B	13	0	2	0	85	82	18	84	R1

6.3.4 Specific Surface Area

The specific surface area (SSA) of the murdrocks was measured using the Ethylene glycol monomethyl ether (EGME) method. Unlike the BET method, which only measures the external SSA, the EGME method measures the total SSA including the surface area inside the interlayer space.

Natural mudrocks extracted from the ocean are Na^+ saturated. However, after the cooking process, the illitic mudrocks are saturated with K^+. To make sure the SSA result is not biased by the cations, a series of comparative tests were done on Ca^{2+}, K^{2+} and Na^{2+} saturated GoM-EI to investigate the effect of cations on SSA measurement. The results are listed in Table 6.4. For each cation, there are three repeated measurements. The average SSA of Ca^{2+} saturated is the highest, being 162 m^2/g. The average SSA of K^+ and Na^+ saturated GoM-EI are similar. The greatest difference in average SSA among different cations is around 7 m^2/g, and this difference is less than 5% of the Ca^{2+} GoM-EI. Based on these measurements, the different cations do not affect the measurement of SSA.

The total SSA for smectitic mudrock and illitic mudrocks are listed in Table 6.5, they are all K^+ saturated. The smectitic mudrock has the highest SSA value (157 m^2/g). As expected, the total SSA decreases with increasing illite content. The illitic mudrock A has 60 m^2/g, while B has 126 m^2/g. The illitic mudrock A and B have similar degree of illite content, but the SSA value of A is only half of the B. This is constant with mineralogy observation. The discrete illite is thicker and larger in size than the I/S. The illitic mudrock A has more discrete illite than the illitic mudrock B, thus the specific surface area of A should be less than B inferring from the mineral composition.

One potential explanation for the SSA difference in the illitic mudrock A and B is the time factor. The fixation of potassium in the interlayer space is the first step for illitization. The neoformed illite needs time to grow bigger in size.

The illitic mudrock A reacted for 30 days while B only reacted for 18 days. Another factor is stress, the illitic mudrock A was cooked under stress. The clay particles have

grain-to-grain contact, so they are easier to grow in size. Whereas the illitic mudrock B was cooked in slurry state, the solid to fluid ratio is high, so clay particles are floating in the pore fluid without contact and are difficult to grow in size.

The SSA value was measured for Boston Blue Clay (BBC). The SSA value of BBC measured by the author is very close to that measure by Cerato and Lutenegger (2002). This validates that the SSA results for the illitic mudrocks and the smectitic mudrock is trustworthy.

Table 6.4: SSA of GoM-EI with different Cations (Unit: m^2/g)

Trial	Ca^{2+}-GoM-EI	K^{+}-GoM-EI	Na^{+}-GoM-EI
1	159	155	152
2	159	159	159
3	169	158	151
Mean	162	157	155
Std. Dev	4.5	1.4	3.4

Table 6.5: Summary of Total SSA

Mudrock	Temp.	Time	Total SSA
	$^{\circ}C$	days	m^2/g
Illitic A	200	30	60
Illitic B	250	18	126
Smectitic			157
BBC			28
BBC (Cerato and Lutenegger, 2002)			30

6.3.5 Observation based on Fabric Analysis

SSA measurements indicate that the particle of the mudrock has been altered by the S-I conversion. In order to gain understanding of the observed mechanical behavior change of the smectitic vs. illitic mudrocks, scanning electron microscope (SEM) images were taken for smectitic and illitic mudrocks. The samples were uniaxially compressed, oven dried and then ion milled to achieve a flat surface for imaging. Images are captured on a vertical cross-section. The SEM images presented are provided by Amer Deirieh and Mark Zablocki.

Figure 6-20 compares the SEM images of the smectitic mudrock and the illitic mudrock B. Both mudrocks are compressed to $\sim$ 100 MPa and to a gravimetric porosity or oven-dried lab porosity of $\sim$ 0.2. Images c) and d) are zoom in view of the red squares in a) and b) respectively. The grey areas are the clay matrix or clay aggregates, the black area is the pore space. The large grains in Figure a) are quartz. Comparing Figure a) and b) qualitatively, the visible pore space in b) is more than the visible pore space in a). The pore space of the illitic mudrock B is more scattered than the smectitic mudrock. The clay aggregates of the smectitic mudrock are larger than the illitic mudrock. According to Deirieh (2016), the SEM porosity of smectitic mudrock reveals only 39-54% of the oven dried lab porosity. The reminder of the gravimetirc porosity is invisible under the resolution of SEM. Based on the SEM images in Figure 6-20 and Deirieh's (2016) study, the author thinks during the S-I transformation, the interlayer pore space which is under the resolution of SEM collapses and more pore space is visible to the SEM.

The viscosity of the interlayer water or bound water is greater than that of free pore water (Low, 1976). The elevated viscosity of interlayer water is attributed to the viscoelectric effect between the exchangeable cation and the negatively charged clay particle surface. When two mudrocks are at the same gravimetric porosity, the one with more interlayer porosity will have a lower permeability. When the interlayer space in the smectitic mudrock collapses and turns into bulk pore space, the fluid has less drag when flows through bulk pore space, therefore the permeability of the mudrock increases after transformation.

Comparing the smectitic mudrock and illitic mudrock B in Figure 6-20, there are more edge-to-face contact between clay aggregates in the illitic mudrock B SEM image. While, clay aggregates in the smectitic mudrock are mostly face-to-face contact. So the illitic mudrock B can support more pore space at a given effective stress compared with the smectitic mudrock.

Figure 6-21 illustrated by Bowers (2011), represents the microsturcture of the smectitic mudrock (Figure 6-21a) and illitic mudrock (Figure 6-21b). Figure 6-21a are mostly "fat" smectite clay matrix. The free pore space is limited. The inside of a

clay aggregate is mostly composed of smectite. The smectite coating covers the illite and quartz. Figure 6-21b represents a illitic mudrock. The clay matrix are skinny compared with the smectitic clay matrix. The volume percentage of the illite over smectite increases. There are more visible and scattered pore space. The SEM images in Figure 6-20 share remarkable similarities with illustration in Figure 6-21.

Figure 6-22 compares the SEM images of the illitic mudrock A (30 days) and B(18 days). Both mudrocks are compressed to $\sim$ 100 MPa and to a gravimetric porosity or oven-dried lab porosity of $\sim$ 0.2. These two mudrocks have similar permeability value and same percentage of I/(I+S). Images c) and d) are zoom in view of the red squares in a) and b) respectively. Both images c) and d) have more visible pore space than the smectitic mudrock. The difference between the illitic mudrock A and B is that the pore space of the illitic mudrock A is less discrete than the illitic mudrock B.

There are two evidences that suggest the illitic mudrock A has greater clay particle size than the illitic mudrock B:

1. The thickness of the clay aggregates in the illitic mudrock A is greater than that of the illitic mudrock B by visual comparison between two SEM images.
2. The SSA of the illitic mudrock A is half of the illitic mudrock B.

With a longer reaction time and applied effective stress, the illite particle grows in size.

6.4 Secondary Compression Evaluation

Previous section summarize the effect of the mineral transformation on the compression and permeability behavior. This section presents the secondary compression or creep observed in the hold stress stages (stages 2 and 3 in Figure 6-11)

6.4.1 Secondary Compression of Protocol A

The void ratio reduction was recorded during the hold stress stages (Figure 6-23). In the first 5 days, the void ratio dropped from 0.616 to 0.605 is due to secondary

compression. The reduction from 0.605 to 0.575 is due to dissipation of pore fluid in the specimen. In the heating up stage, the cell pressure was increased gradually from 0.4 MPa to 2 MPa in order to keep cell fluid in the liquid phase at a temperature of 200 $°C$. The increase in stress combined with temperature change causes the specimen to consolidate. It is confirmed by calculating the time factor T_v and the corresponding average degree of consolidation (U_v).

$$T_v = \frac{C_v t}{H_d^2} \tag{6.6}$$

where C_v is obtained from the CRS test of the smectitic mudrock, t is about 90 minutes, H_d is the half of the specimen thickness. The resulting T_v is greater than 2, and the corresponding U_v is close to 100%.

After the heating up, the void ratio dropped gradually from 0.575 to 0.550 in 30 days. This is a combination of creep and transformation. The rapid void ratio reduction from 0.550 to 0.530 was caused by contraction of the specimen when the temperature of the device dropped from 200 °C to 23 °C.

Secondary Compression at Room Temperature

The secondary compression rate at room temperature is determined by calculating the slope of e - log(t) curve in Figure 6-24. Time starts when the excess pore pressure measured at the base of the high temperature CRS cell is zero. The secondary compression curve keeps a flat slope from 0 second to 10^4 seconds, then the slope increases and become log linear. The C_α is determined to be 0.0067 by calculating the slope of P1-P2. The void ratio reduces from 0.616 to 0.605. Δe_{1-2} is the void ratio difference between P1 and P2. Converting the void ratio space to porosity space, the rate of secondary compression $C_{\alpha n}$ is 0.0023.

Secondary Compression at Elevated Temperature

Figure 6-25 shows the secondary compression curve at elevated temperature. Time starts when the heating element was turned on. The curve is color coded, the green

markers are the void ratio reduction due to increase in stress combined with temperature change, the red markers are the void ratio reduction when temperature due to creep and mineral transformation, the blue markers are the void ratio reduction when the specimen cooled down.

C_α at elevated temperature is determined using the slope of P3-P4. Δe_{3-4} is the void ratio difference between P3 and P4. The rate of secondary compression is calculated as 0.0095 in void ratio space and 0.004 in porosity space. C_α increases by 50 % compared with C_α at room temperature.

Discussion of Creep Rate

Karig et al. (2003) presents the rate of secondary compression as $C_{\alpha n}$ in the porosity space. The data were measured using odemeter tests at room temperature. The samples are clay rich mudrocks from two locations: ODP site 897 at a depth of 619 m below the seafloor (blue dots in Figure 6-26)and from A20ST well at a depth of 2100 m below the seafloor where the source material for this study is extracted (triangles in Figure 6-26). $C_{\alpha n}$ measured in this study (purple and red dots) are added to Karig's database. Author's data points are in the typical range as Karig's. Additionally, Karig et al (2003) found that there is an increase in $C_{\alpha n}$ when time is greater than 10^5 seconds, but in author's test, there is no obvious change in $C_{\alpha \eta}$ after 10^5 seconds.

According to Mesri and Castro (1987), the C_α / C_c ratio is around 0.04 for low stress level ($<$ 1 MPa) and high plasticity soil. The $C_{\alpha@23C}$ / C_c is 0.016, C_c is measured from 4 MPa to 5 MPa in Figure 6-11. This number is much lower than 0.04.

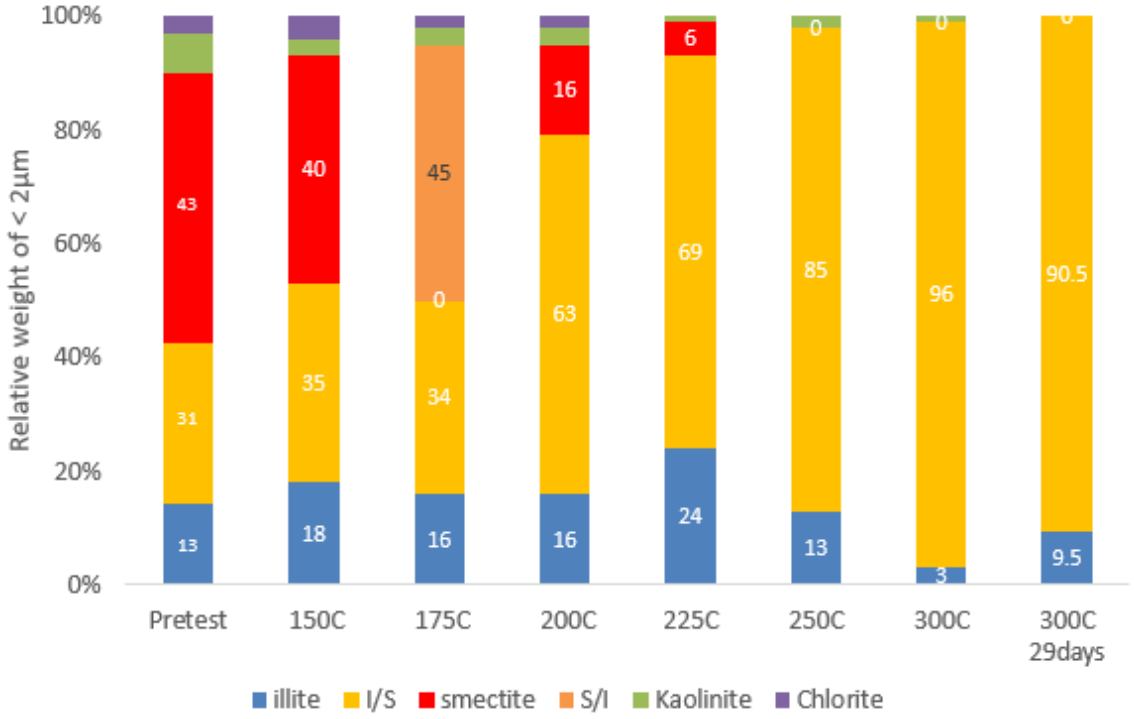

Figure 6-1: Summary of Hydrothermal Reaction Result from Author's Master Thesis. (Ge, 2016) All tests were cooked for 18 days using a hydrothermal cooker. The mineralogy result shown in last column was cooked for 29 days.

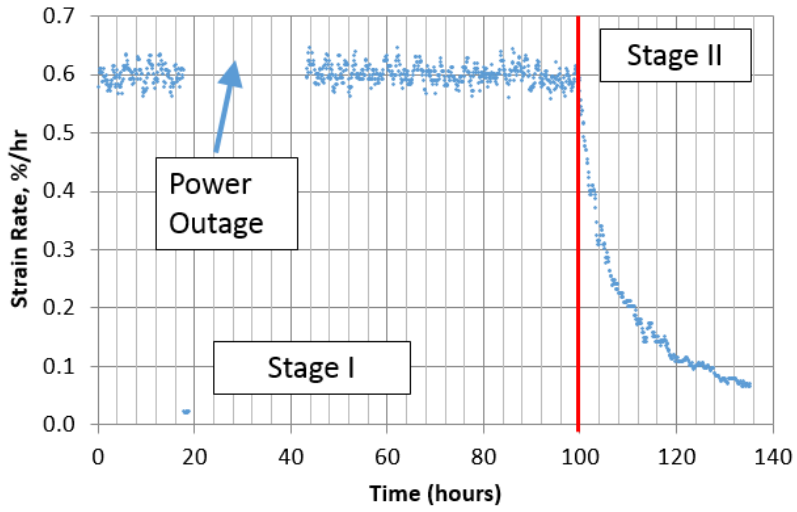

Figure 6-2: Strain Rate for Smectitic Mudrock. The starting strain rate is around 0.6 $\%/hr$, the stage I is constant rate of strain control, stage II is constant pore pressure gradient control. Power outage occurred in the middle of the test, causing data missing.

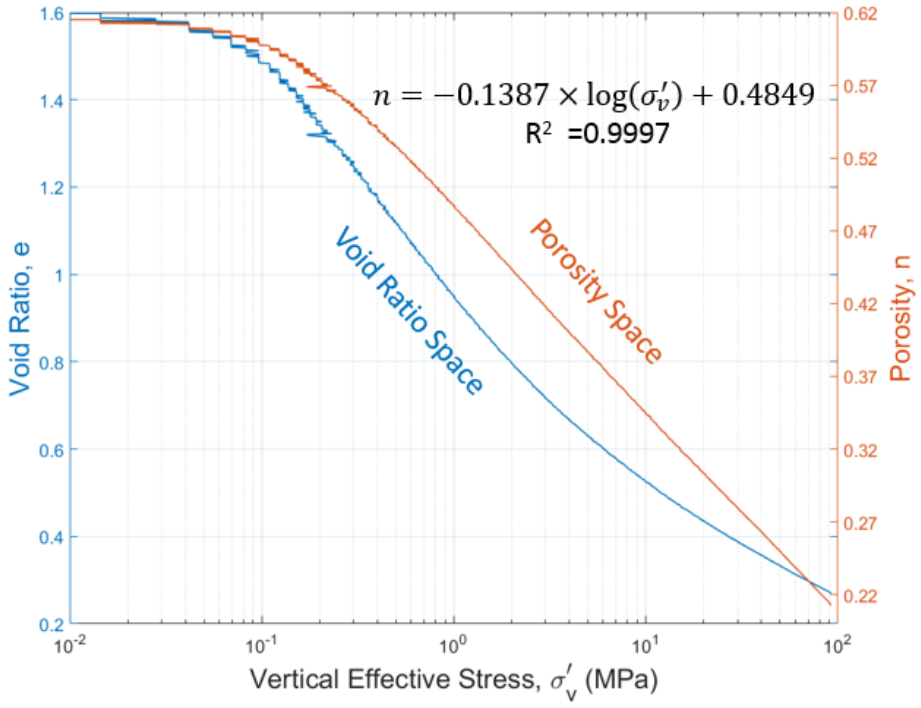

Figure 6-3: Compression Curve for the Smectitic Mudrock. Compression curve shows good linearity in n - $log(\sigma_v')$ space.

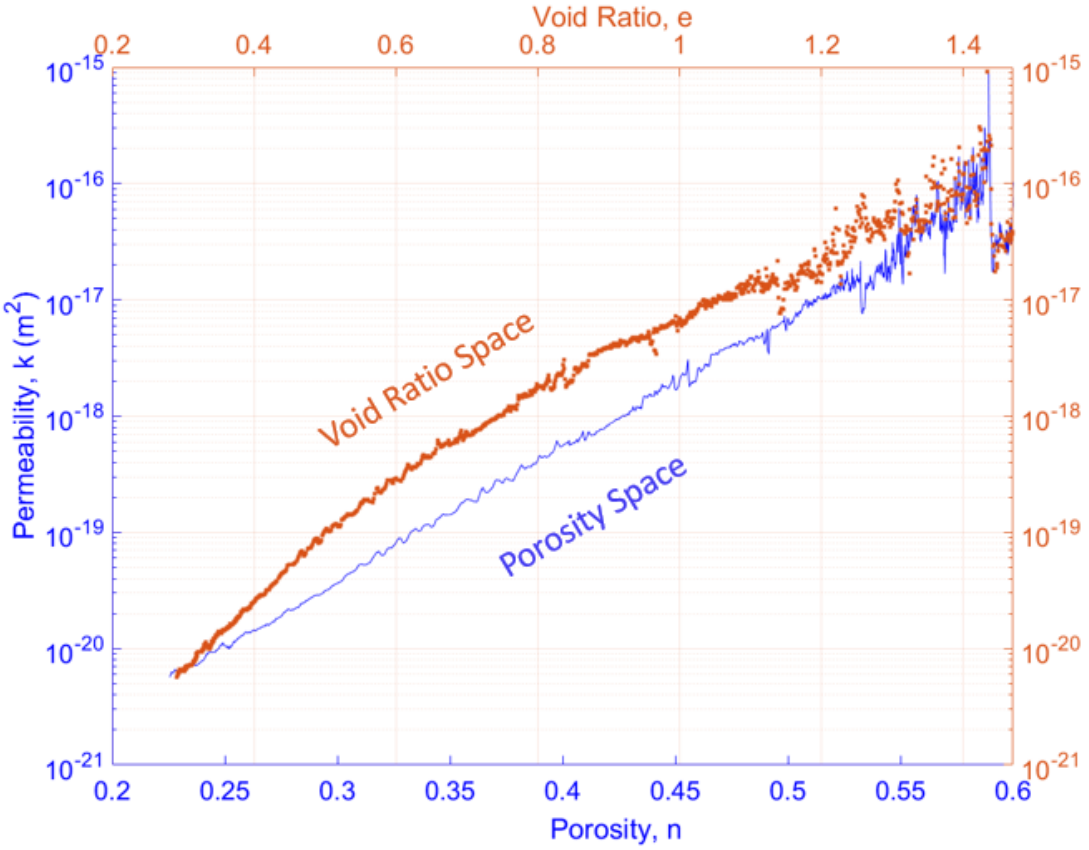

Figure 6-4: Permeability Data for the Smectitic Mudrock. The permeability line displays good linearity in n - $log(\sigma_v^{'}$ space.

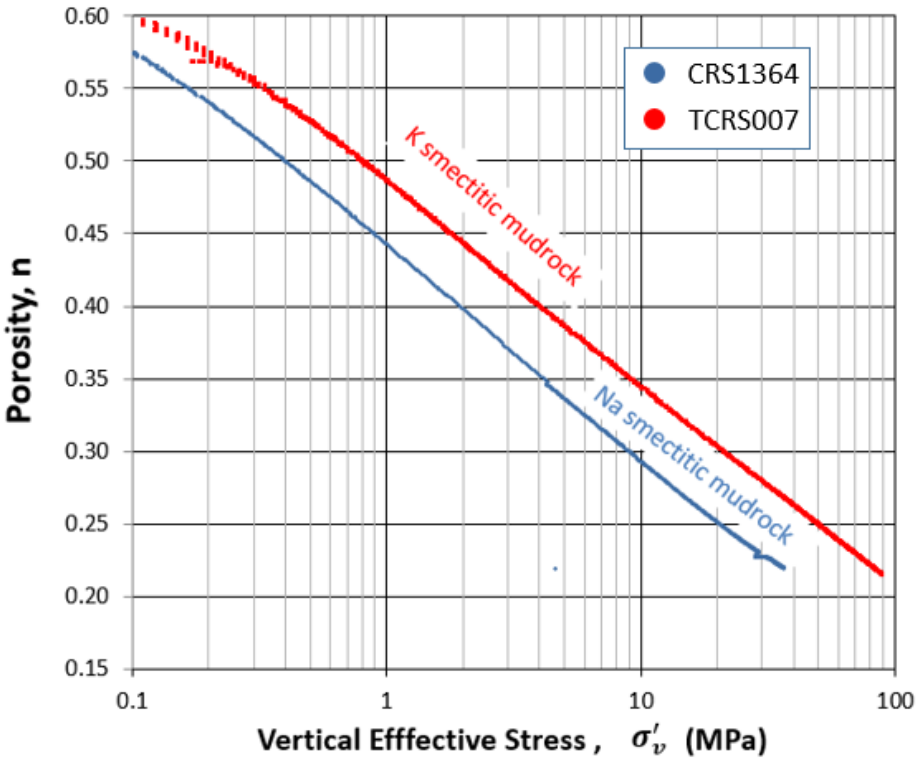

Figure 6-5: Compression Curve for the K-Smectitic Mudrock and Na-Smectitic Mudrock (Fahy, 2014).

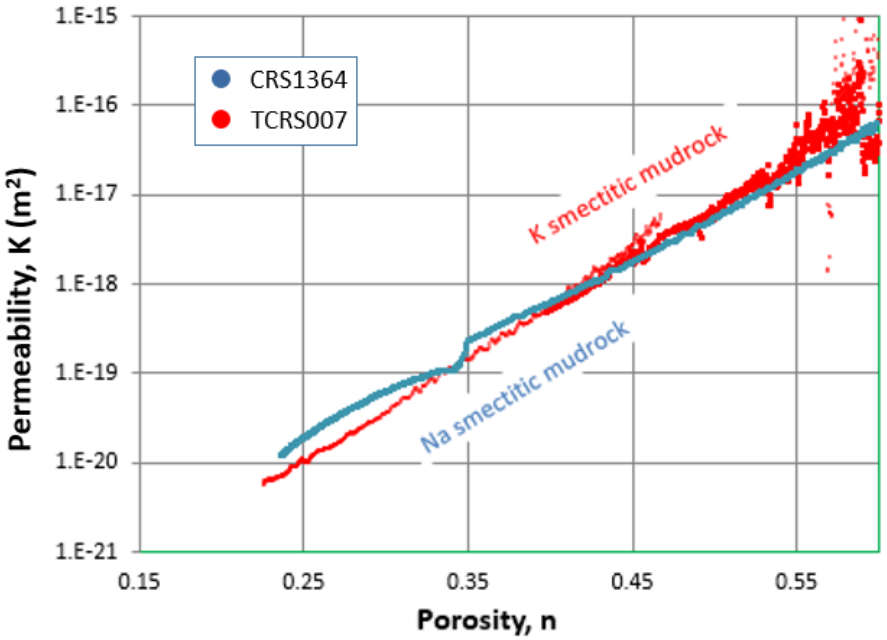

Figure 6-6: Permeability curve for the K-Smectitic Mudrock and Na-Smectitic Mudrock (Fahy, 2014).

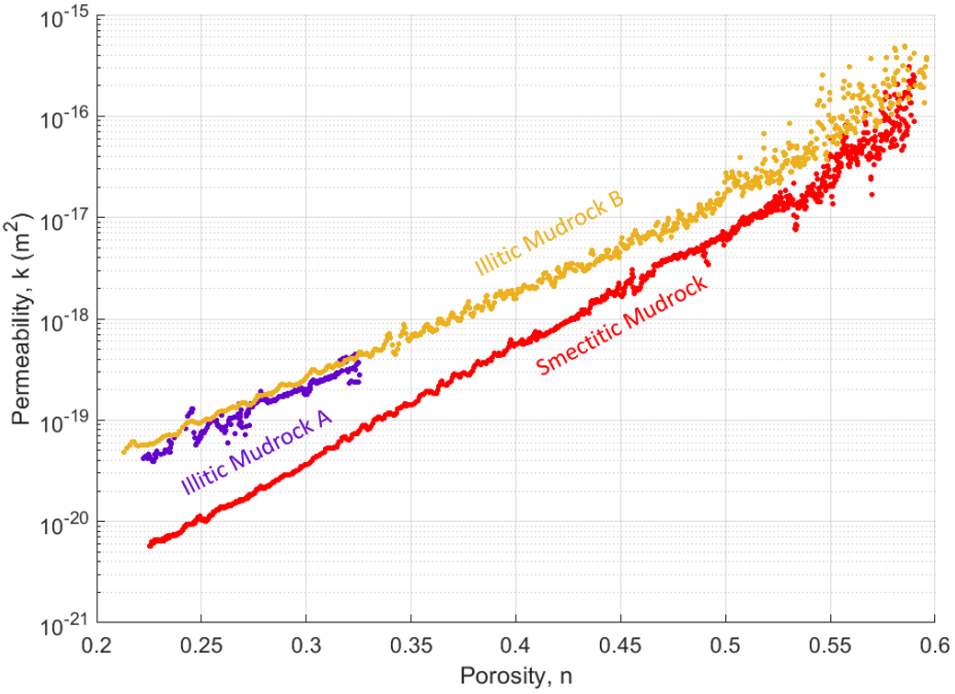

Figure 6-7: Permeability Curve Comparison

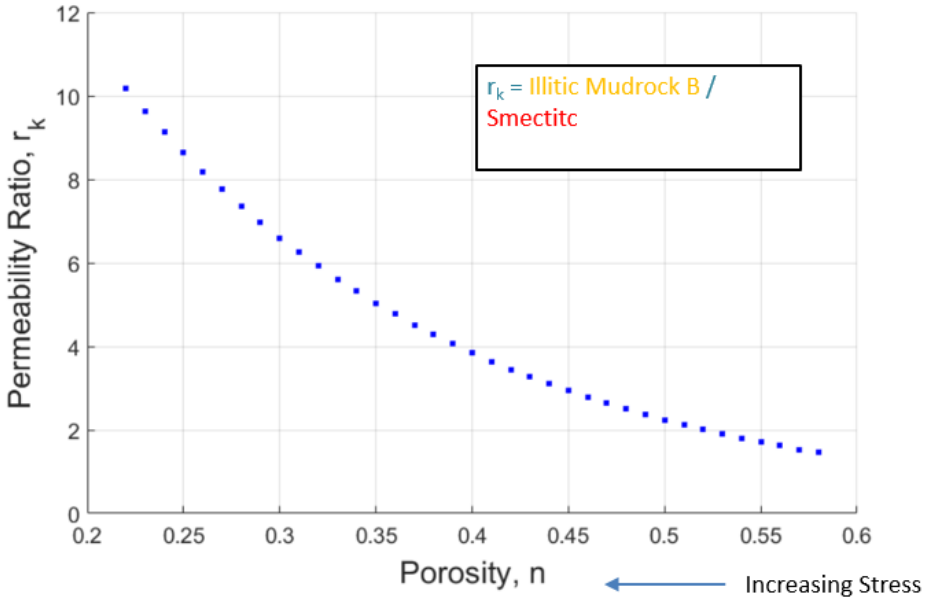

Figure 6-8: Ratio of Permeability. r_k is the ratio of permeability of the illitic mudrock B over permeability of the smectitic mudrock.

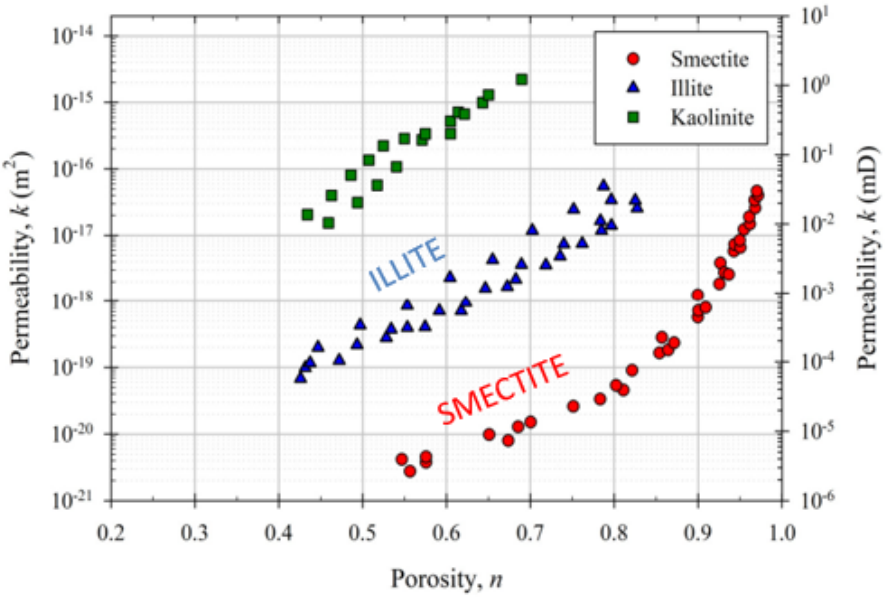

Figure 6-9: Permeabilities of smectite, illite and kaolinite clay minerals (adapted from Mesri and Olson 1971)

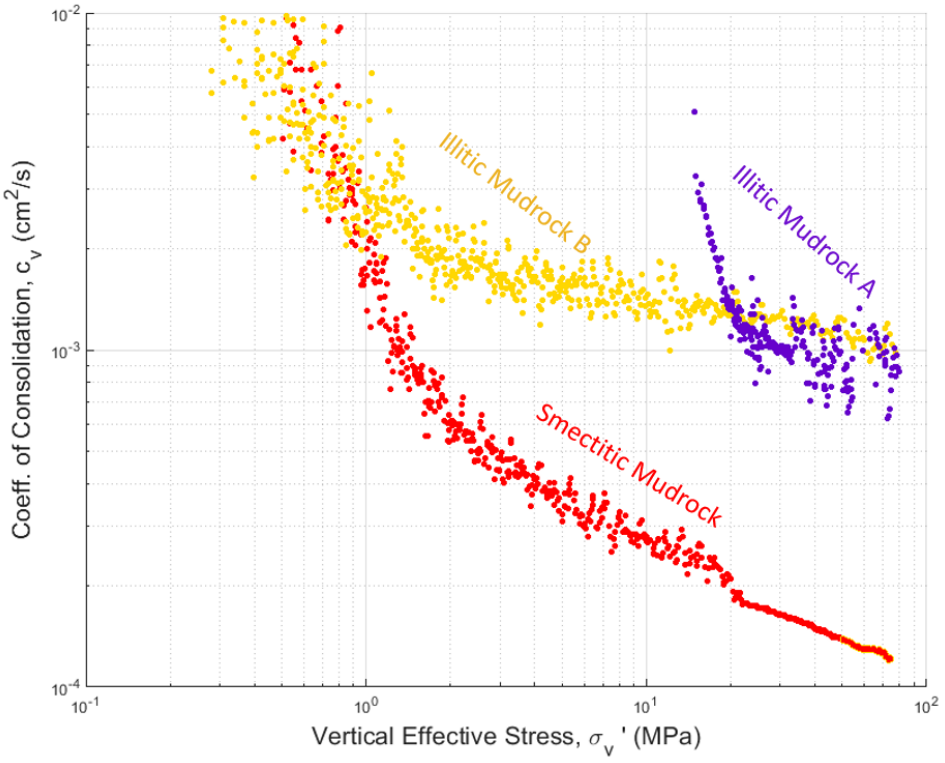

Figure 6-10: Coefficient of Consolidation Comparison

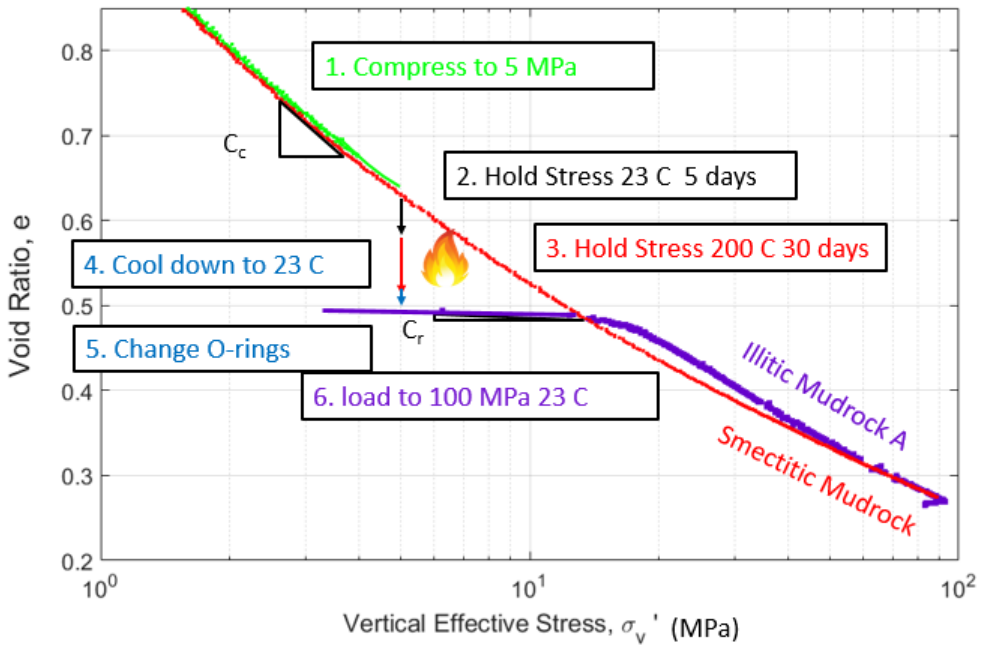

Figure 6-11: Compression Curve for Illitic Mudrock A

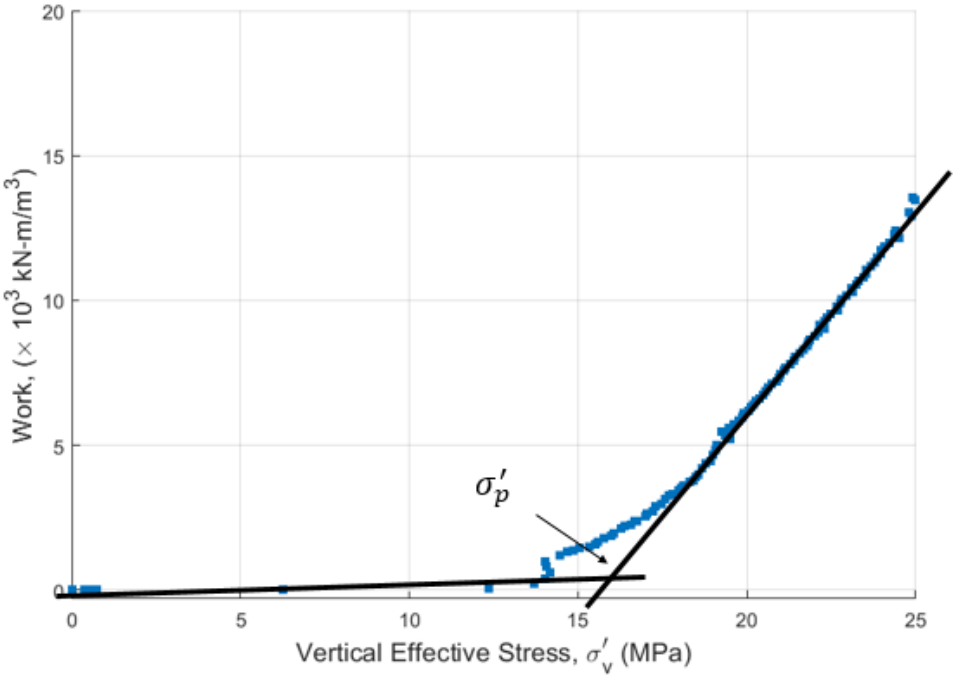

Figure 6-12: Strain Energy Method to Determine the Preconsolidation Stress for Illitic Mudrock A. The $\sigma_p^{'}$ is determined to be 16 MPa.

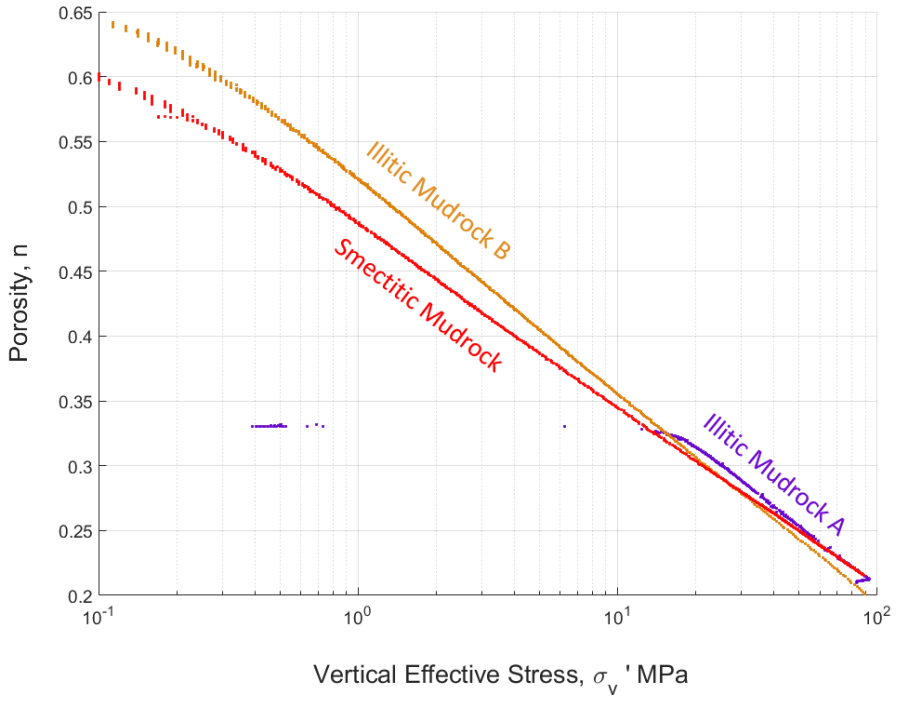

Figure 6-13: Compression Curve Comparison for the Smectitic Mudrock and Illitic Mudrocks.

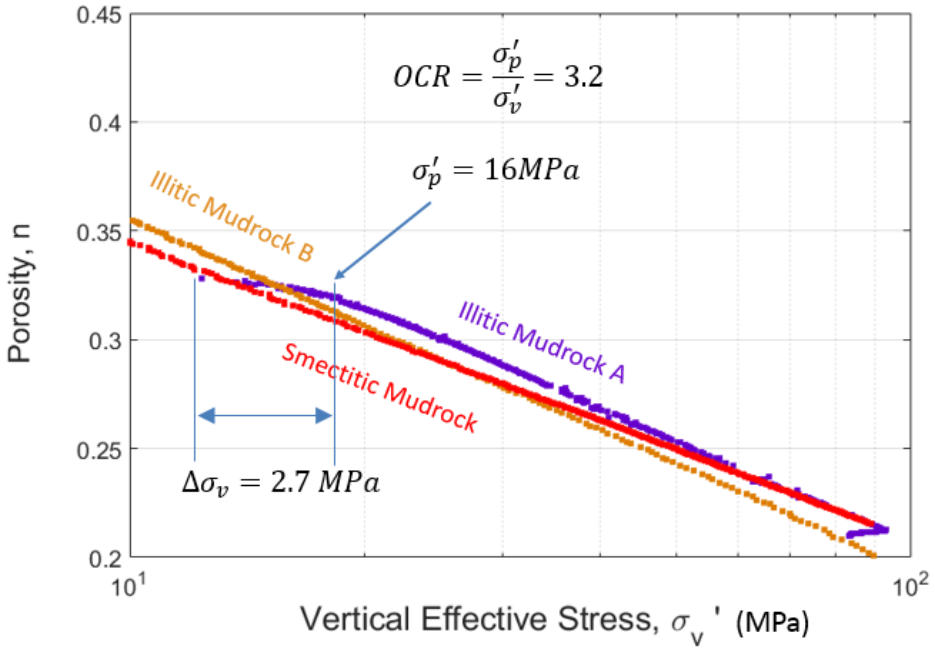

Figure 6-14: Compression Curve Comparison for the Smectitic Mudrock and Illitic Mudrocks from 10 to 100 MPa.

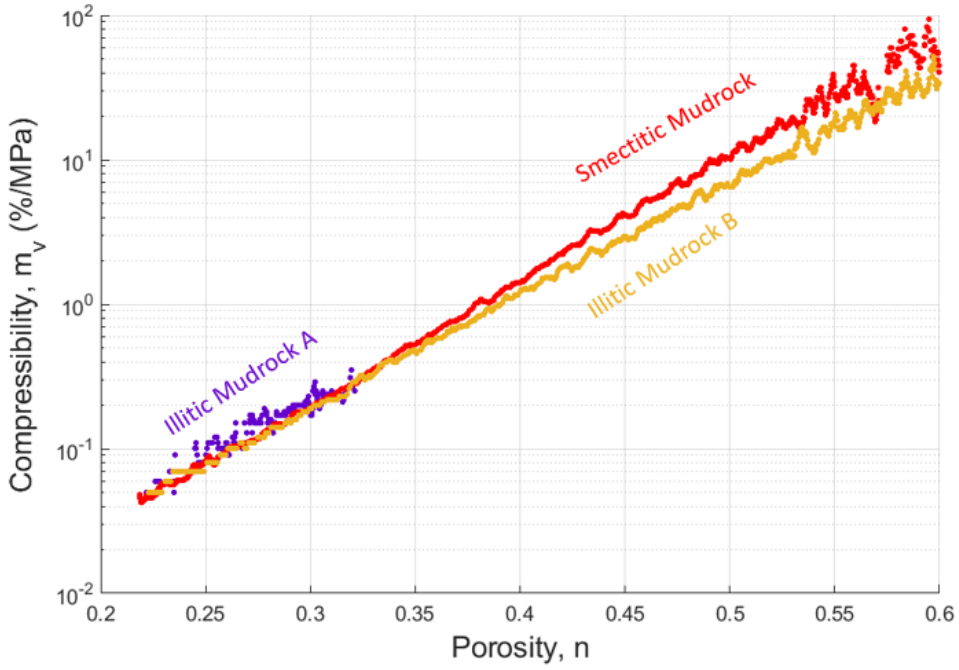

Figure 6-15: Compressibility Comparison for the Smectitic Mudrock and Illitic Mudrocks.

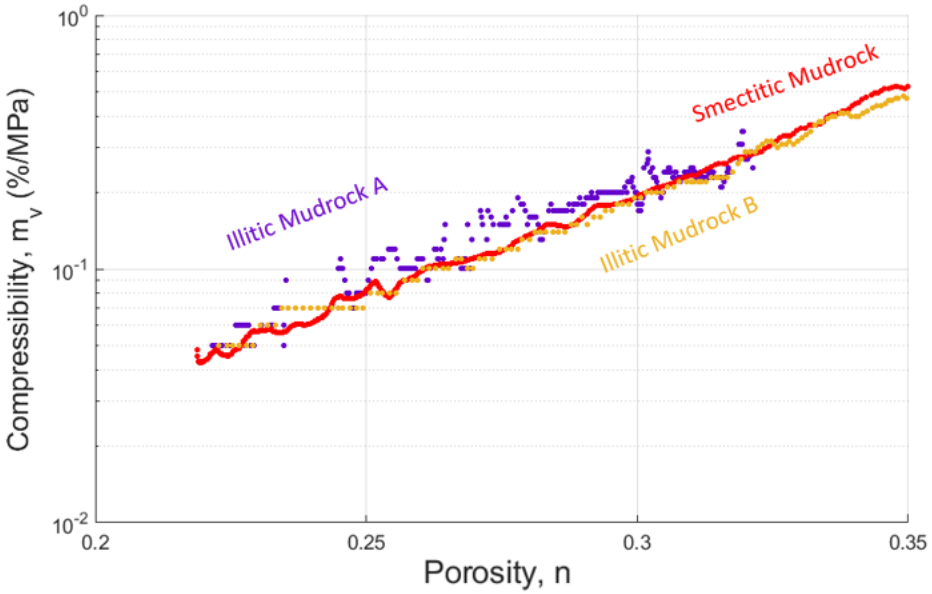

Figure 6-16: Compressibility Comparison Zoom In

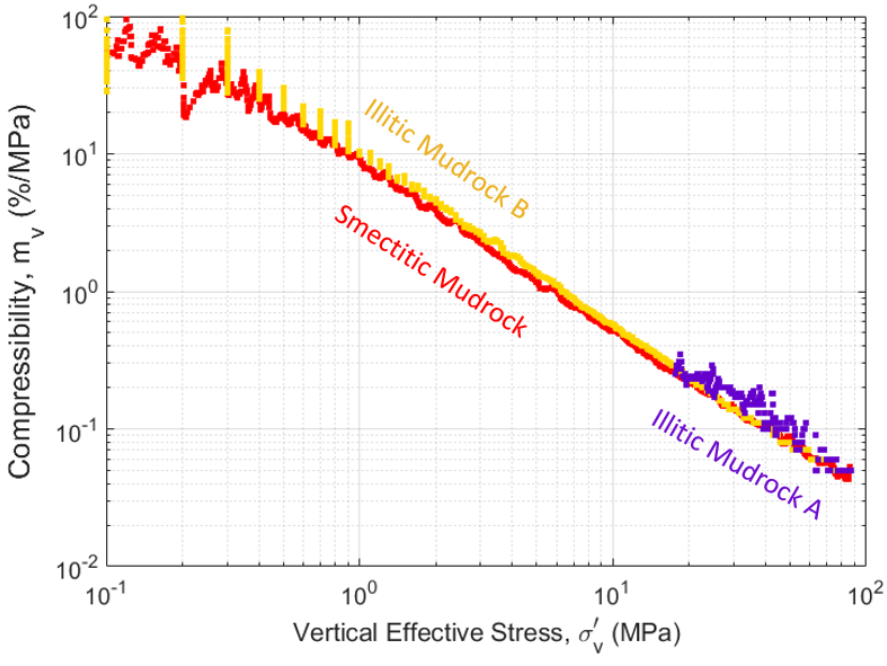

Figure 6-17: Compressibility in Stress Space

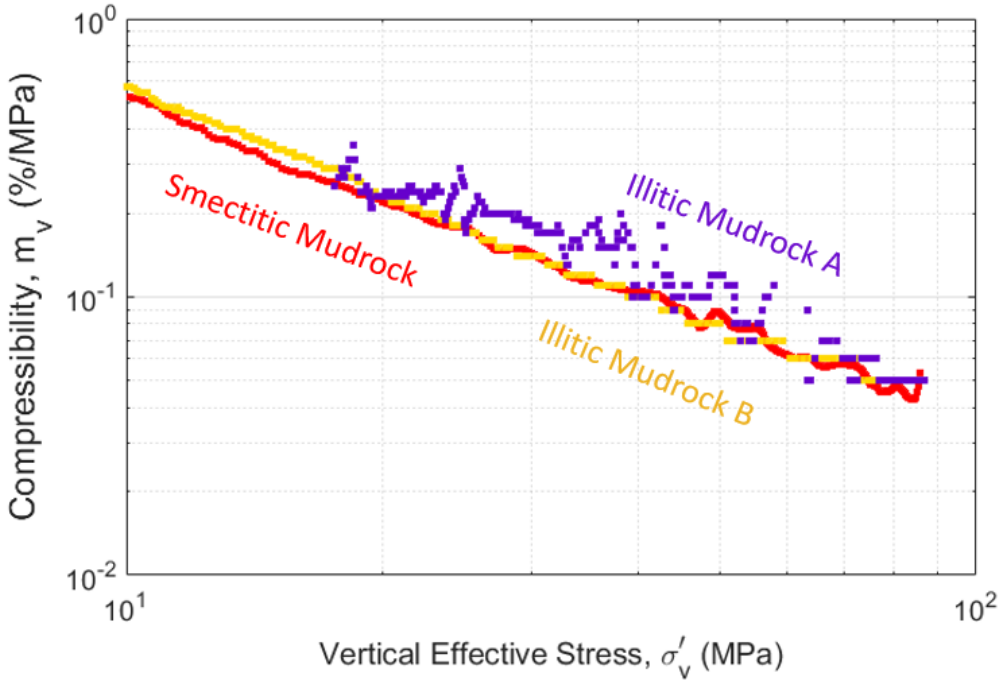

Figure 6-18: Compressibility in Stress Space Zoom In

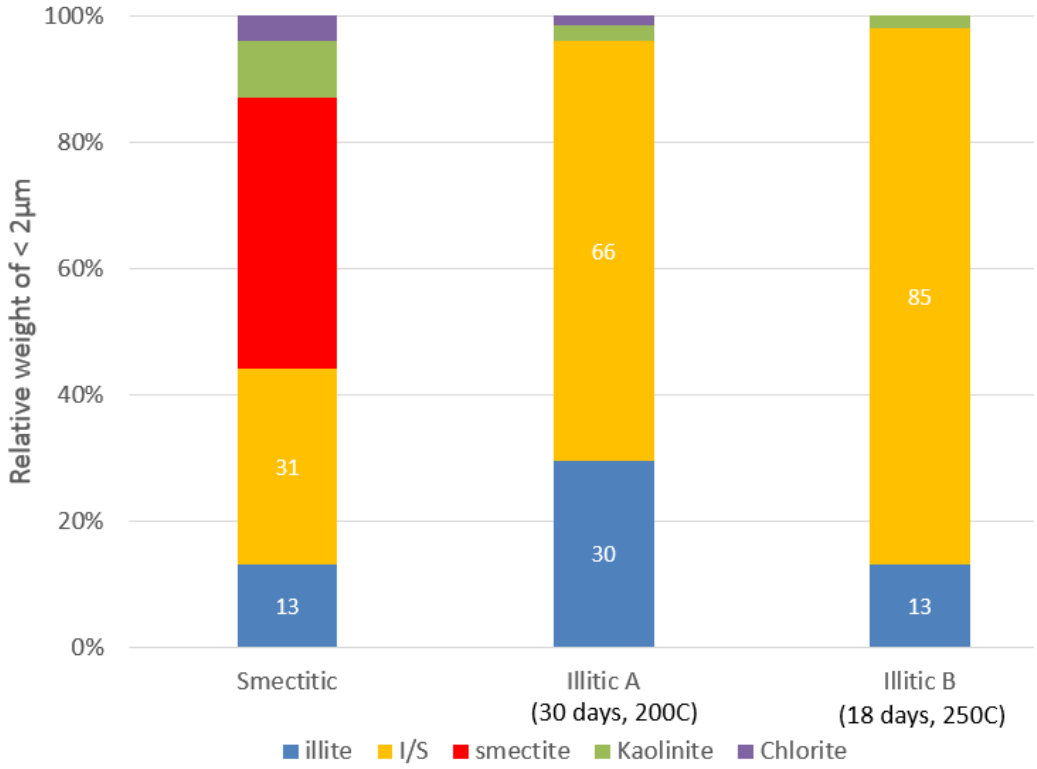

Figure 6-19: Mineral Composition of the three Mudrocks

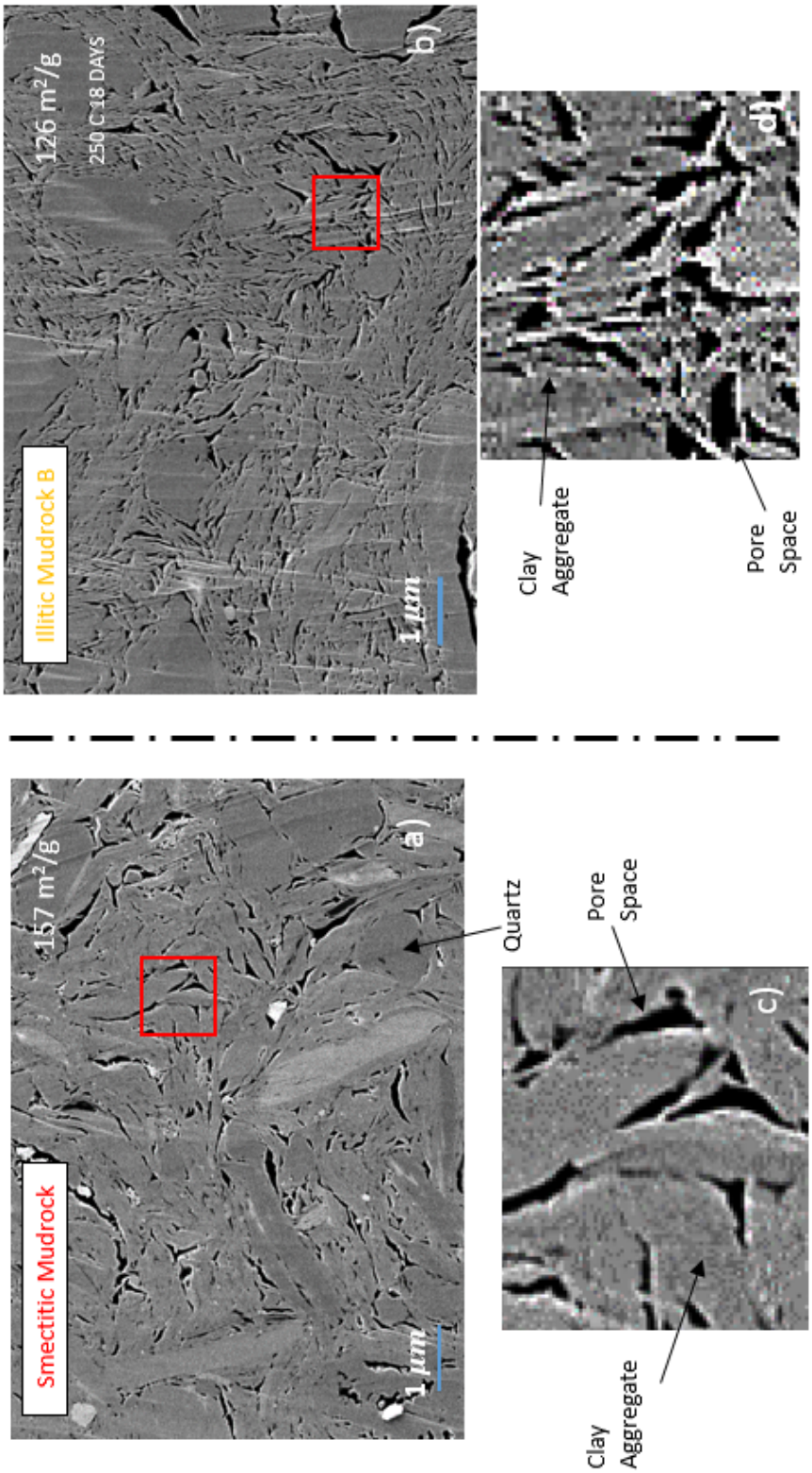

Figure 6-20: SEM Images for the Smectitic Mudrock and Illitic Mudrock B at around 90 MPa and a Porosity of 0.21. The magnification is 100kx.

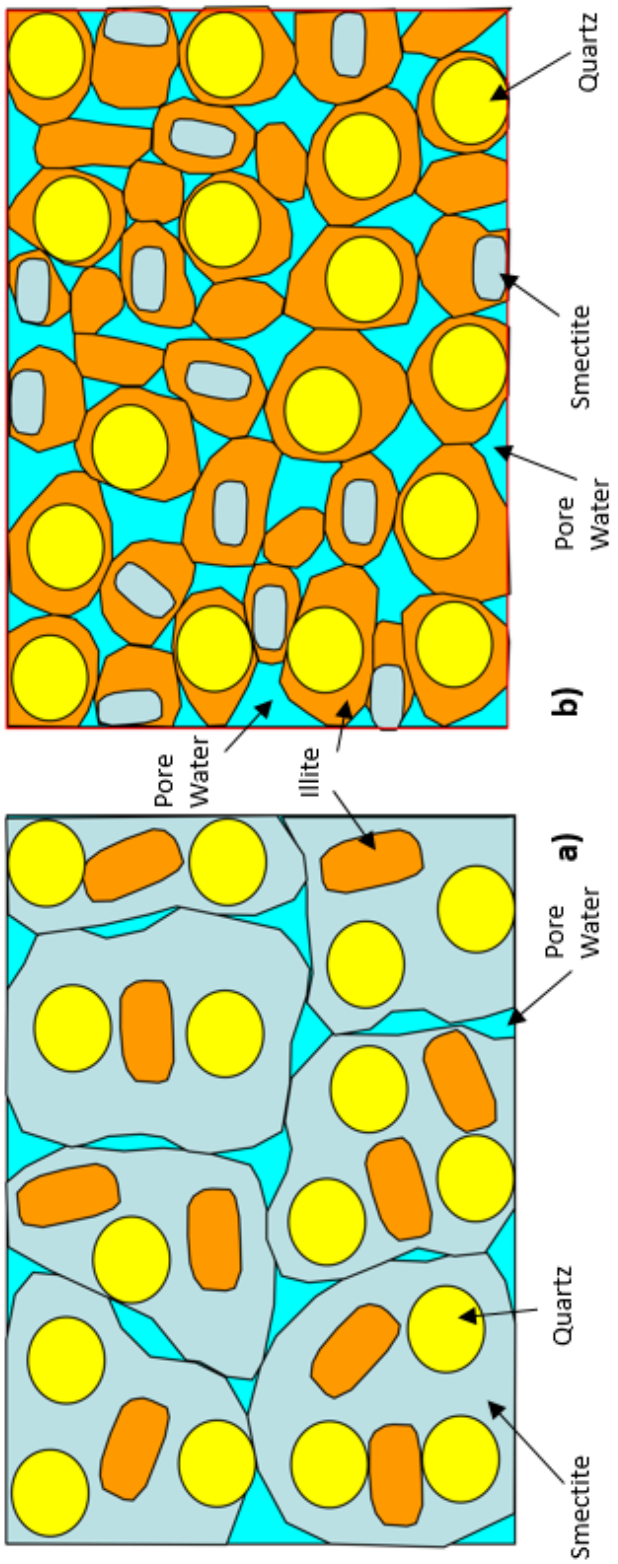

Figure 6-21: Illustration for the Smectite-to-illite Transformation (after Bowers 2011)

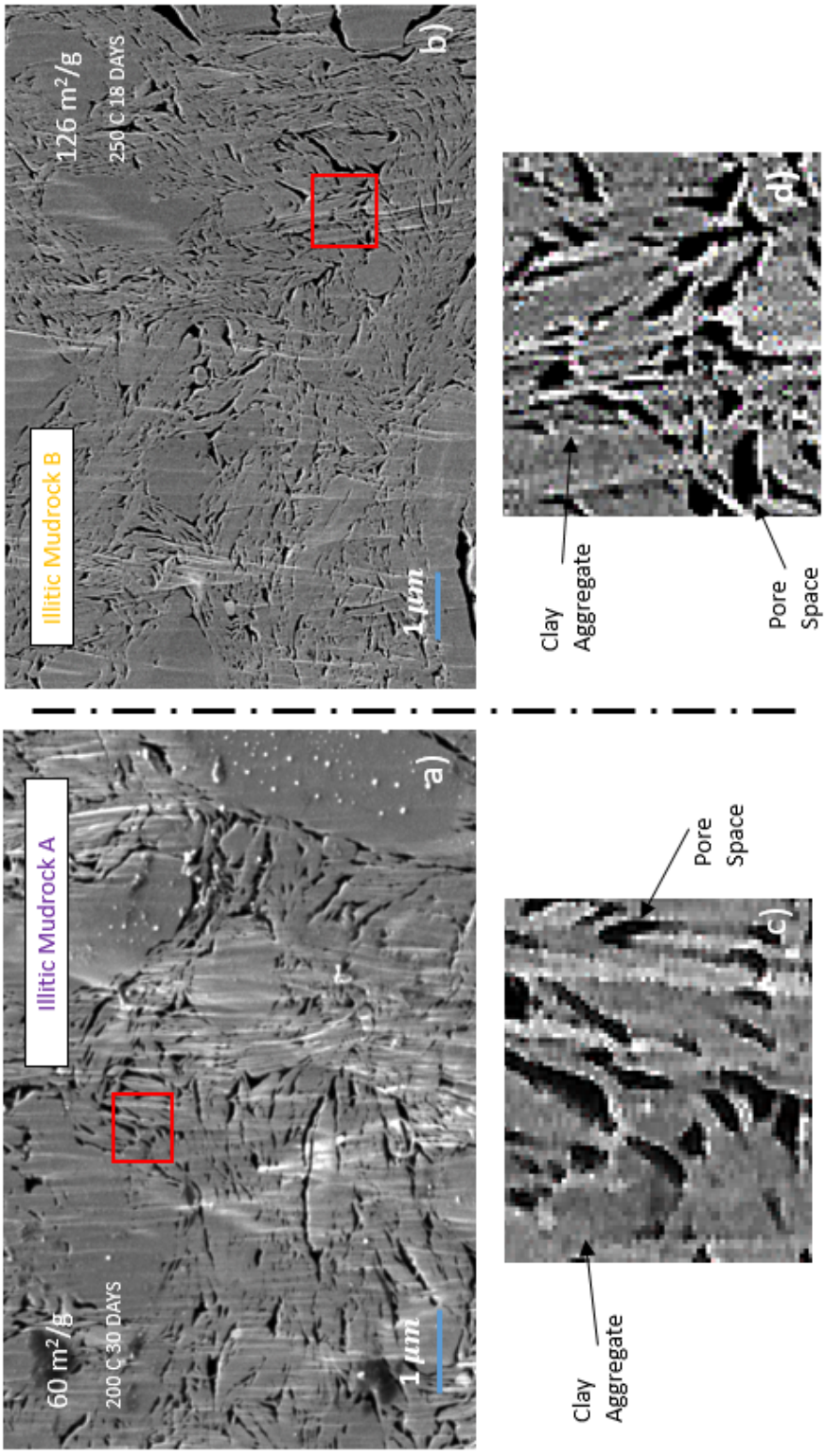

Figure 6-22: SEM Images for the Illitic Mudrock A and B.

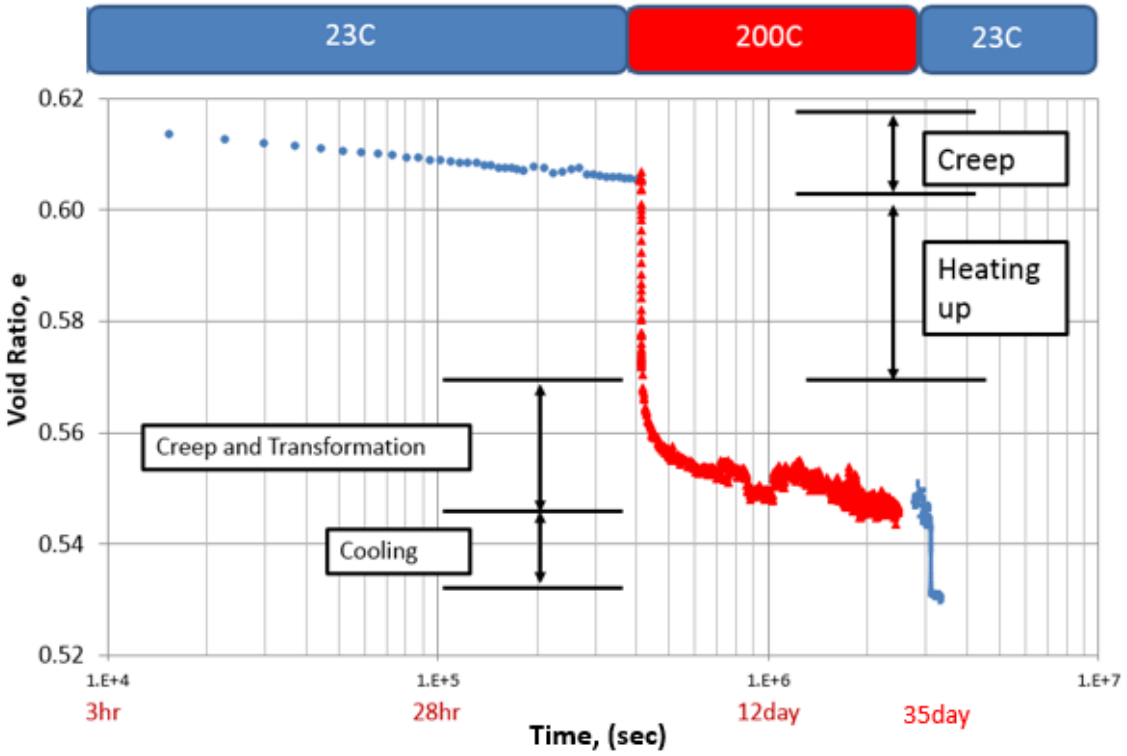

Figure 6-23: Void Ratio Drop at Stage 2 & 3 due to Creep and Mineral Transformation.

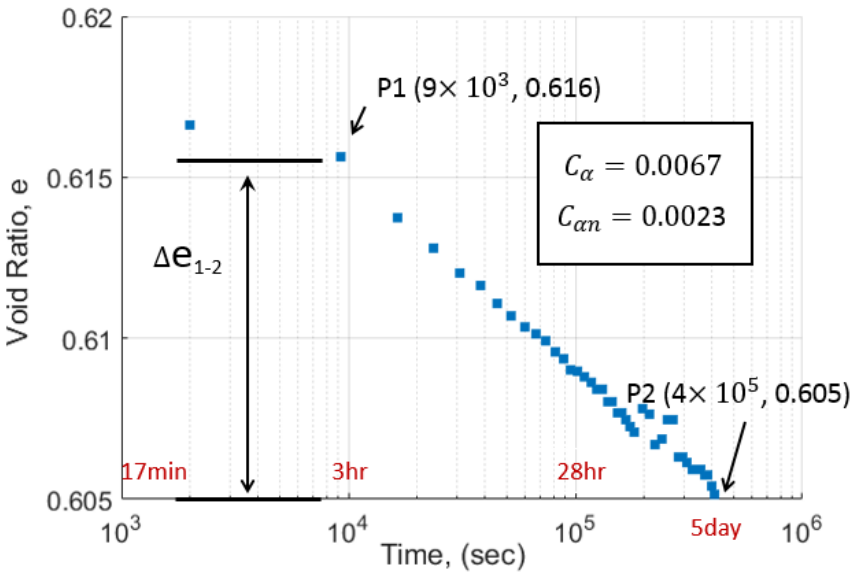

Figure 6-24: Creep at Room Temperature. The zero time is from the time when excess pore pressure measured at the base of the high temperature CRS cell is zero.

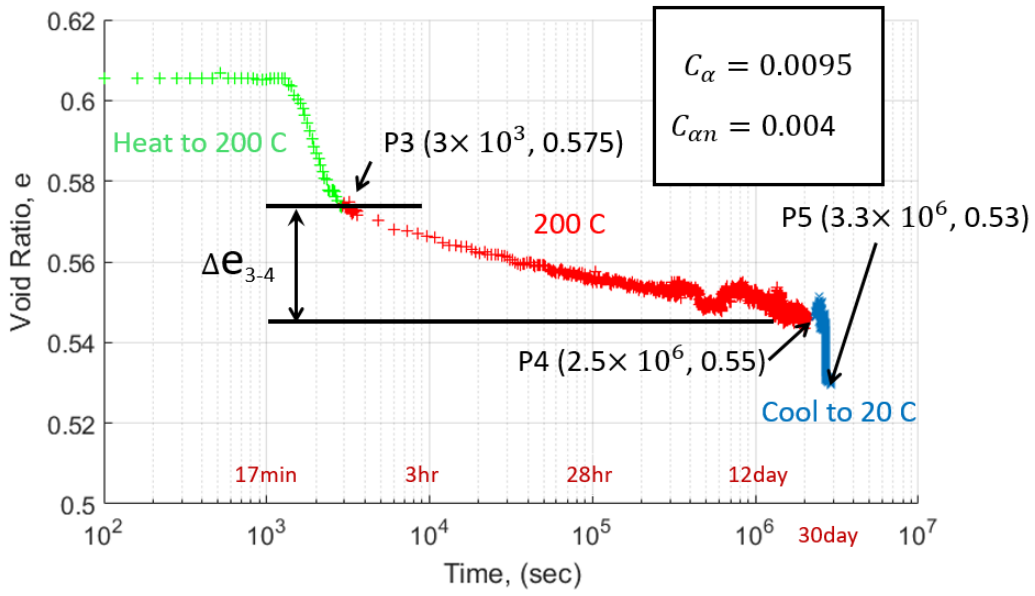

Figure 6-25: Creep at Elevated Temperature. The zero time is from the time when the temperature of the high temperature CRS device starts to increase.

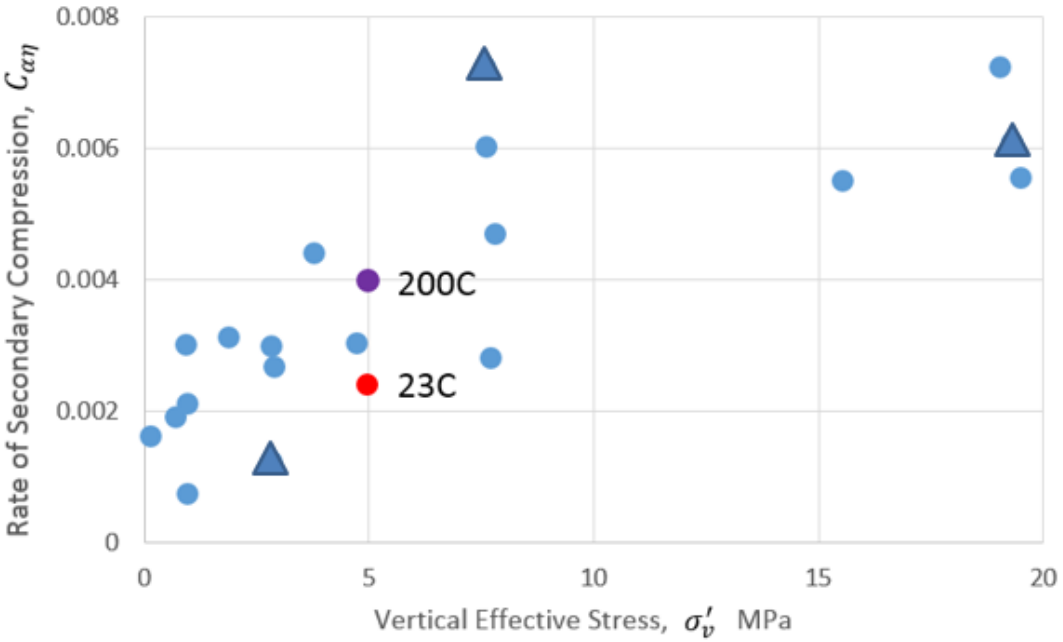

Figure 6-26: $C_{\alpha n}$ Value in This Study vs. Data from Karig et al. (2003). Blue dots are ODP site 897 at a depth of 619m below the seafloor, triangles are A20ST well samples at a depth of 2100m below the seafloor where the source material for this study is extracted. $C_{\alpha n}$ measured in this study are purple and red dots.

Chapter 7

Overpressure Model

7.1 Introduction

Models that are based on the relationships between mudrock porosity and effective stress have been used as a valid principle to estimate the overpressure in many sedimentary basins (England et al., 1987; Warbrick & Osborne, 1998). However, in the basins where high temperature and mineral diagenesis prevail, the magnitude of overpressure is often underestimated by these models.

This chapter presents a new approach to estimate overpressure potential caused by transformation of smectite to illite. It is based on the observations made from the experimental program. This overpressure model predicts the magnitude of overpressure based on the relationship between the smectitic mudrock porosity and effective stress, as well as the degree of illitization I/(I+S).

7.2 Components of Mudrock Transformation

Figure 7-1 a) illustrates the basic element of a mudrock. The total volume is 1 including soil grains (clay fraction and non-clay fraction), bound water and pore water. The porosity, n, includes the volume of bound water and pore water. The volume of the bound water is represented as a function of the soil grain and parameter

f using Equation 7.1

$$n_{bw} = f \times (1 - n) \tag{7.1}$$

The theoretical value of parameter f is a function of weight percentage of clay fraction in the soil grains (CF), amount of smectite in the clay fraction (S), and percentage of bound water per smectite particle (BW).

$$f = CF \times S \times BW \tag{7.2}$$

When the mudrock is subjected to mineral transformation, the volume of expelled bound water is:

$$n_{expelled\ bw} = c \times f \times (1 - n) \tag{7.3}$$

where c is the degree of illitization or change in I/(I+S).

The effect of smectite-to-illite transformation depends on the boundary conditions. In a free draining system where the expulsion of pore water is not limited by the low permeability of the mudrock, the system does not generate overpressure, but will experience a higher rate of creep, leading to lower porosity at a given effective stress.

One can consider two scenarios in a low permeability system for estimating overpressure: constant volume system in Figure 7-1 b) and undrained system in Figure 7-1 c). In a constant volume system, the volumetric expansion of expelled bound water Δn translates into overpressure ΔP. This situation sets the maximum magnitude of overpressure. In a general undrained system, the volume is able to swell due to the reduction of the effective stress. The mudrock unloads following the swelling curve of the mudrock while maintaining constant total stress.

7.3 Model Formulation

7.3.1 Free Draining System

If the illitization occurs in a short period of time without additional sediment accumulation (constant total stress), and the permeability of the mudrock is high enough

for the generated overpressure to dissipate, the mudrock remains at constant effective stress. The material will compress at constant effective stress with the reduction of porosity or void ratio. Referring to Figure 7-2, the porosity drops from B to D due to a combination of creep and mineral transformation. The porosity reduction from B to C is mainly attributed to creep, the porosity reduction from C to D is mainly caused by release of bound water during the S-I transformation. The free draining condition is analogous to the condition for transforming illitic mudrock A in the laboratory. In a free draining condition, the system does not create overpressure but it does produce apparent overconsolidation. The illitization process densifies the mudrock significantly in comparison to the observed secondary compression.

The compression behavior observed in the laboratory suggests that the illitic mudrock (the purple line) will converge to the virgin consolidation line of the smectitic mudrock once the stress goes beyond the quasi-preconsolidation stress. This is contrary to the traditional S-I transition model. Lahann's (2001) model suggests that the illitic mudrock is lower in porosity space at a given effective stress, and the compression curve of the illitic mudrock is simply parallel to the smectitic line (Figure 7-2).

To quantify the effect of mineral transformation and to estimate the resulting overconsolidation, some assumptions are necessary:

1. The system starts with a known amount of smectite in the clay fraction, assuming illite is formed from smectite-to-illite transformation.
2. The void ratio or porosity reduction during the constant effective stress stage is the effect of two independent processes: 1. reduction due to creep (from point B to point C in Figure 7-2); 2. reduction due to mineral transformation (from point C to point D in Figure 7-2).
3. The void ratio or porosity reduction due to mineral transformation from point C to point D is solely caused by the dissipation of expelled interlayer water or bound water.
4. The volume of the expelled bound water is proportional to the degree of smectite-to-illite transformation,

5. The volume of the expelled bound water based on experimental observation is about 1/20 of the theoretical expelled bound water value.

Void ratio or porosity reduction also involves fabric change, dissolution and precipitation of clay mineral and quartz, but these factors cannot be quantified with existing experimental data, thus they are not included in the model.

7.3.2 Constant Volume System

In a low permeability system where no drainage is allowed and no additional total stress is exerted, when the bound water is released to the free pore space, the volume of bound water increases since the density of the bound water is higher than 1 (Powers, 1967). The load transfers from the clay matrix to pore water, and leads to a reduction of effective stress (Figure 7-3). The increased water volume causes the pressure to increase, but the deformation of the system is fixed. This situation sets the maximum magnitude of overpressure.

If the system is allow to swell, the potential volumetric expansion caused by the S-I transformation is calculated as:

$$\Delta n = (R_p - 1) \times n_{expelled\ bw} = (R_p - 1) \times c \times f \times (1 - n) \tag{7.4}$$

The Δn is a function of R_p, f, and the amount of conversion c, where R_p is the ratio between the density of bound water and the density of pore water.

$$R_p = \frac{\rho_{bound\ water}}{\rho_{pore\ water}} \tag{7.5}$$

and c is in linear proportion to the change in I/(I+S), assuming the volume of expelled bound water is in linear relationship with the percentage of smectite transformed. Section 7.4.2 discusses the procedures to determine f.

Since the deformation of the system is fixed, the volumetric expansion of the bound water translates into an increase in the pressure ΔP. The ΔP is the product of bulk modulus of water K_p and volumetric strain of the pore volume $\epsilon_{pore\ vol}$, where

$\epsilon_{pore\ vol}$ is calculated as:

$$\epsilon_{pore\ vol} = \frac{\Delta V}{V_0} = \frac{e_0 - e}{e_0} = \frac{n_0/(1-n_0) - n/(1-n)}{n_0/(1-n_0)} \tag{7.6}$$

The porosity after the illitization n_0 is the sum of the porosity before transformation and the porosity expansion of the bound water.

$$n_0 = n + \Delta n \tag{7.7}$$

Substituting n_0 in Equation 7.6 with Equation 7.7, the volumetric strain is expressed as:

$$\epsilon_{pore\ vol} \approx \frac{\Delta n/n_0}{1 - n_0 + \Delta n} \tag{7.8}$$

The overpressure is calculated as

$$\Delta P = K_p \times \epsilon_{pore\ vol} = K_p \times [\frac{\Delta n/n_0}{1 - n_0 + \Delta n}] \tag{7.9}$$

This ΔP sets the upper bound of the overpressure.

7.3.3 Undrained System

In an undrained system where the system keeps constant mass, the basic element can swell with additional deformation Δn as shown Figure 7-1 c).

The compression curve for the smectitic mudrock can be represented by the following equation:

$$n = n_{0n} + C_{cn} \times log(\sigma'_{max}) \tag{7.10}$$

Where C_{cn} is the compression index in porosity space, n_{0n} is the porosity value when effective stress is 1 MPa. When illitization happens in an undrained system, the effective stress reduces, the mudrock becomes less dense and the void ratio or porosity increases. The porosity vs. effective stress curve follows the unloading curve in Figure 7-3 as overpressure develops. The effective stress decreases from σ'_{max} to σ'_f. The volumetric expansion or change in porosity, Δn, is calculated using Equation 7.4.

The Δn is related to the unloading curve using the following equation:

$$\Delta n = C_{sn} \times log(\frac{\sigma^{'}_{max}}{\sigma^{'}_{f}}) \tag{7.11}$$

Where C_{sn} is the swelling index in porosity space, it is approximately 1/10 of the compression index C_{cn} according to Burland (1990) for high plasticity material.

Solving Equation 7.4 and 7.11, the final effective stress, $\sigma^{'}_{f}$, is expressed as:

$$\sigma^{'}_{f} = \frac{\sigma^{'}_{max}}{10^{[\frac{(R_p-1)\times c\times f\times(1-n)}{C_{sn}}]}} \tag{7.12}$$

The values for $\sigma^{'}_{max}$ and n are generated from Equation 7.10 based on the measured compression curve.

The overpressure is the difference between $\sigma^{'}_{max}$ and $\sigma^{'}_{f}$.

$$\Delta P = \sigma^{'}_{max} - \sigma^{'}_{f} \tag{7.13}$$

The overpressure ratio is

$$OPR = \frac{\Delta P}{\sigma^{'}_{max}} = \frac{\sigma^{'}_{max} - \sigma^{'}_{f}}{\sigma^{'}_{max}} \tag{7.14}$$

7.4 Evaluation of Free Draining Case

7.4.1 Theoretical Released Bound Water

The theoretical value for the released bound water is calculated based on the data available for the GoM-EI mudrock.

Table 7.1 summarizes the data for the GoM-EI mudrock at three states including virgin state, smectitic, and illitic A. The virgin state assumes that all illite converts back to smectite and there is no illite in the clay fraction. The mineral composition for smectitic and illitic A are listed in Table 6.3. The smectite percentage is the total amount of smectite over the sum of 5 phases in the clay fraction. The smectite

percentages are 86%, 50% and 14% for virgin material, smectitic and illitic A respectively. The virgin state material has zero degree of transformation. The smectitic GoM-EI has 42% conversion, the illitic A GoM-EI has 84% conversion.

The clay fraction (CF) is 63% of the soil grain, and it is the same for all three states. The porosity of the GoM-EI element at 5 MPa effective stress after 35 days of creep is 0.369. The procedure for determining this porosity is described in section 7.4.2.

During the transformation, the d-spacing of a smectite particle reduces from 15 Å to 10 Å (illustrated in Figure 7-5). The volume of a smectite particle reduces by 33%, so $BW = 33\%$. The theoretical f is calculated:

$$f = 0.63 \times 0.86 \times 0.33 = 0.179 \tag{7.15}$$

The S = 0.86 is used for calculating the f when conversion is zero. For a mudrock that has 42% of increase in the I/(I+S), the theoretical expelled bound water is

$$n_{expelled\ bw} = (84\% - 42\%) \times 0.179 \times \times (1 - 0.369) = 0.0474 \tag{7.16}$$

7.4.2 Analysis of Lab Test

This subsection describes the procedure to determine the volume change associated with expelled bound water during the transformation stage for the illitic mudrock A.

Based on the assumptions made in the beginning of this chapter, the void ratio reduction from C to D (Δe_{C-D}) is the volume change associated with the bound water or the interlayer water released during the transformation. In order to calculate this, the void ratio reduction in the heating up stage is removed. The creep curve AB at room temperature is extrapolated to 35 days to determine the void ratio reduction due to creep (dash line in Figure 7-6 and Figure 7-7).

The void ratio reduction due to creep and mineral transformation at elevated temperature is equal to Δe_{3-4} measured in Figure 7-7. Using the creep rate measured at room temperature, the extrapolated void ratio reduction Δe_{ext} or the void ratio

reduction due to creep Δe_{B-C} is determined by Equation 7.17. Time for P3 and P4 is shown in Figure 6-25.

$$\Delta e_{B-C} = \Delta e_{ext} = C_{\alpha@23C} \times [log_{10}(P4) - log_{10}(P3)] = 0.02 \tag{7.17}$$

Δe_{C-D}, the difference between Δe_{ext} and Δe_{3-4}, is the void ratio reduction due to mineral transformation (Figure 7-7).

$$\Delta e_{C-D} = \Delta e_{3-4} - \Delta e_{ext} = 0.005 \tag{7.18}$$

Knowing Δe_{C-D}, Δe_{ext} and the void ratio for B = 0.605, the void ratio and porosity for point C and D are listed in Table 7.1. The porosity for expelled bound water is calculated in Equation 7.19.

$$n_{expelled\ bw} = 0.369 - 0.367 = 0.002 \tag{7.19}$$

Table 7.1: Summary Table

		Based on the theortical release of Bound Water				Lab Test	
		Virgin material	smectitic	illitic A	Increment	Fig. 7-7	
	Symbol					n	e
Clay fraction	CF	0.63	0.63	0.63			
smectite	S	0.86	0.5	0.14			
bound water	BW	0.33	0.33	0.33			
Bound water density	Rp	1.4	1.4	1.4			
bw fraction	f	0.179	0.179	0.179			
conversion	c	0	0.42	0.84	0.42		
Porosity after creep	n	0.369	0.369	0.369		0.369	0.585
Porosity after trans						0.367	0.580
Expelled bw porosity	$n_{expelled\ bw}$		0.0474	0.0948	0.0474	0.002	

Theoretical Value vs. Experimental Analysis

The $n_{expelled\,bw}$ from the experimental analysis in Equation 7.19 is 0.002. The theoretical released bound water volume (Equation 7.16) is 20 times greater than the one measured in the test. The small change in expelled bound water measured during the transformation implies that there is no significant structural change due to mineral transformation. This observation is consistent with the compression behavior measured in the illitic mudrock A and B. The compressibility of the illitic mudrocks is similar to the smectitic mudrock. Mineral transformation has a small impact on compression behavior.

7.5 Evaluation of Overpressure Cases

The following results are based on the GoM-EI material. Parameters including f, C_{cn} and n_{0n} are determined from experimental test.

Figure 7-8 presents the results calculated from the overpressure model. The orange dots are the overpressure based on Equation 7.9. The constant volume condition generates the upper bound for the overpressure. The black triangles are the overpressure (c = 20%) calculated using Equation 7.13 for the undrained system. The blue dots (σ'_{max}) are the compression curve for the smectitic mudrock. The red dots (σ'_{f}) are the reduced effective stress due to overpressure. The ratio between the ΔP and σ'_{max} is the overpressure ratio for the undrained system. The overpressure ratio increases as the porosity decreases, because the difference between ΔP and σ'_{max} decreases as the porosity decreases.

The upper bound overpressure (orange dots) is greater than σ'_{max} as shown in Figure 7-8, but the difference between the upper bound overpressure and σ'_{max} reduces as porosity decreases. The overpressure calculated for the constant volume system is physically impossible. An upper limit for the overpressure is controlled by the fracture pressure or the minimum principle stress for a borehole (Osborne and Swarbrick, 1997). The σ'_{max} + pore pressure is greater or equal to the minimum principle stress if there is no tectonic loading. In a more general case, the upper limit for overpressure

should be the σ'_{max}.

A more realistic and practical scenario for the overpressure model is an undrained system. The inputs for the model are listed: 1. $R_f = 1.4$; 2. $f = 0.179$; 3. $K = 2.24$ GPa; 4. $C_{cn} = 0.1387$, $n_{0n} = 0.485$; 5. $C_{sn} = 0.014$. The values for n_{0n} and C_{cn} are from the CRS test on the smectitic GoM-EI mudrock (Equation 6.1). Varying the degree of transformation, c, from 20% to 100%, a series of overpressure ratio curves are generated to see the effect of overpressure with different degrees of illitization (Figure 7-9).

When c = 20% in Figure 7-9, the overpressure ratio increases from 60% to 85% from a porosity of 0.63 to 0.20. Increasing the degrees of transformation from 20% to 100%, the overpressure ratio curves shift right. The overpressure for each curve increases significantly. The offset gaps between every 20% increase in conversion are not of equal distance.

From 20% I/(I+S) to 40%, the offset distance along the entire porosity range is about 20%. The higher degree of transformation curves (c= 60%, 80% and 100%) have significant overpressure ratio increase compared with 20% conversion, they achieve 100% of overpressure ratio when porosity is below a certain value. c = 60% curve reaches 100% overpressure ratio when porosity is smaller than 0.28. c = 100% curve reaches 100% overpressure ratio when porosity is below 0.5. The offset gap between every 20% increase in c diminishes as conversion degree increases. The offset distances between these three curves (c= 60%, 80% and 100%) are quite small compared with the gaps between 20%, 40% and 60%. The non-linearity of the offset gaps between the porosity vs. overpressure ratio curves is due to the fact that the swelling curve in the undrained system is log linear. When presenting the overpressure ratio in linear space, the offset gaps are non-linear.

Results in Figure 7-8 and Figure 7-9 are using 1.4 g/cm^3 as the density of the bound water for calculating Rp. According to Powers (1967), the density of the bound water is greater than 1.0 g/cm^3, and extends up to 1.7 g/cm^3. To study the effect of the bound water density, porosity is fixed at 0.388, which corresponds to 5 MPa effective stress, the $C_{sn} = 1/10\ C_{cn}$. Figure 7-10 shows the relationship between

the overpressure ratio and Rp at a porosity of 0.388. The percentage labels in the figure are the degree of conversion. For 100% of transformation, the overpressure ratio increases from 83% to 100% when the Rp increases from 1.1 to 1.3; when Rp is greater than 1.3, the overpressure ratio remains 100%. Reducing the degree of transformation, the overpressure ratio vs. Rp curves shift down. For c = 80%, 60% and 40% curves, they start at a lower overpressure ratio value compared to c = 100% curve; they reaches 100% of overpressure ratio when Rp is greater than certain value. The c= 20% curve follows the increasing trend as well but only reaches 91% overpressure ratio at Rp = 1.7.

Parameters including n, c and Rp, as well as C_{sn} affects the overpressure ratio. Figure 7-9 and Figure 7-10 demonstrates the influence of the c and Rp on overpressure estimation. Figure 7-11 shows the effect of C_{sn} on the magnitude of overpressure. The porosity is fixed at 0.388, and Rp at 1.4. The percentage labels in the figure are the degree of conversion. For 20% of transformation, a stiffer swelling index ($C_{sn} = \frac{1}{13}C_{cn} = 0.011$) generates 85% of overpressure ratio; when the C_{sn} to C_{cn} ratio increases to 1/7 ($C_{sn} = 0.02$), the overpressure reduces to 64%. The reduction in overpressure ratio for each curve decrease as the degree of transformation increases. In addition, the magnitude of overpressure ratio for each curve increases as the degree of transformation increases.

The results presented in this section assumes the system never drains. It is more reasonable to consider that the mudrock has particle drainage and allows additional creep and relaxation. With those consideration, the resulting overpressure ratio will reduces accordingly.

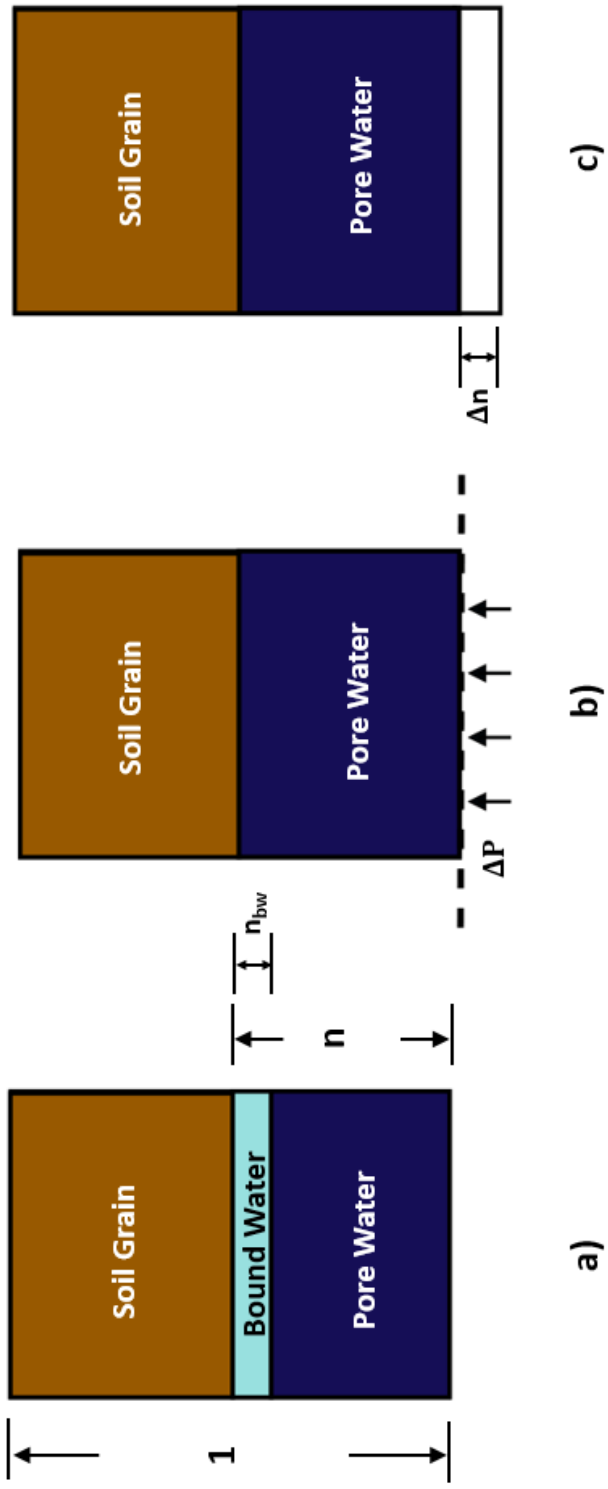

Figure 7-1: General Model of Overpressure a) the basic element b) constant volume system c) undrained system

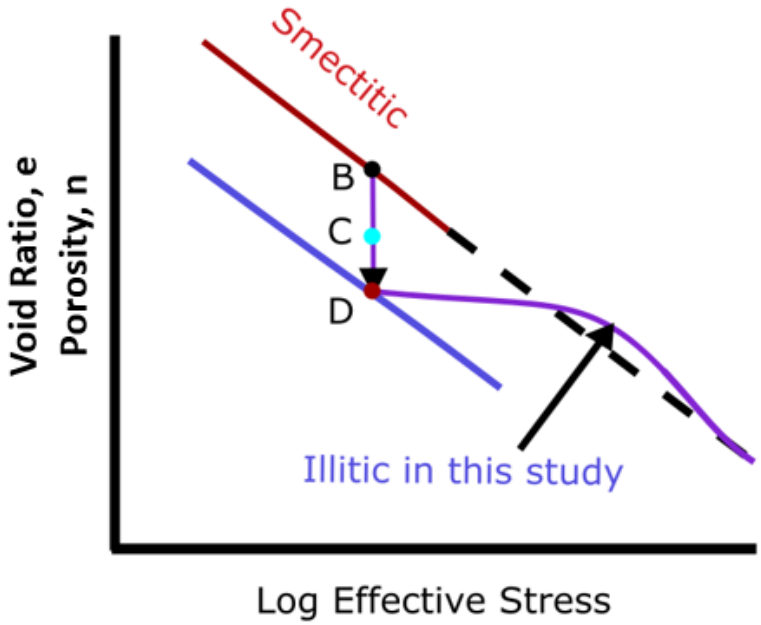

Figure 7-2: The Compression Behavior of a mudrock going through S-I transition for a Free Draining System

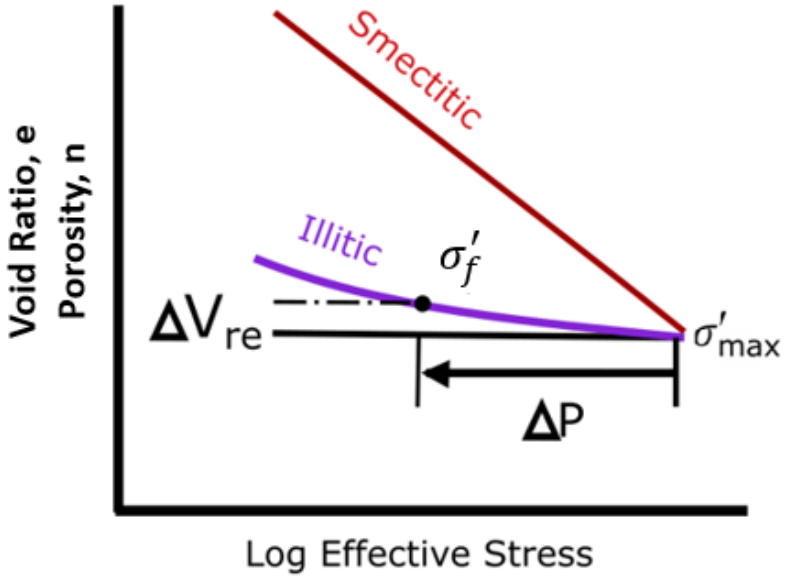

Figure 7-3: The Proposed Overpressure Model for an Undrained System

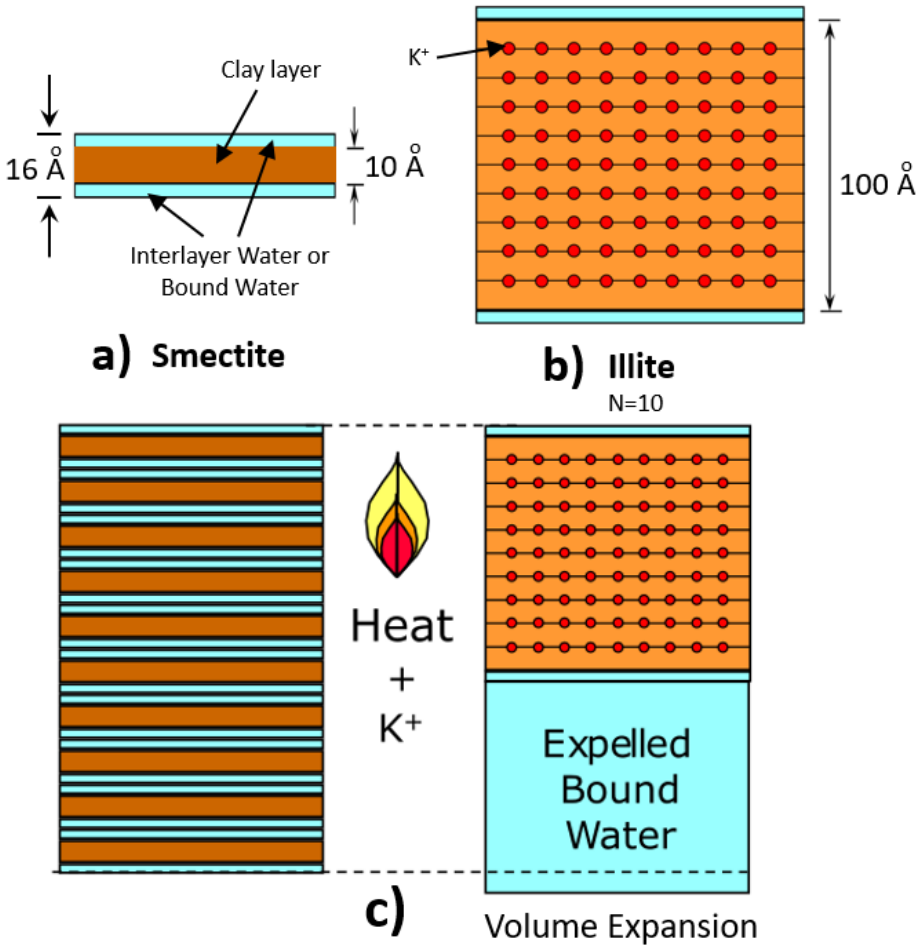

Figure 7-4: Explanation for Volume Expansion Due to bound Water Release. (after Bowers 2011). When the bound water releases to the pore space, the bound water volume increases because the bound water density is greater than 1.

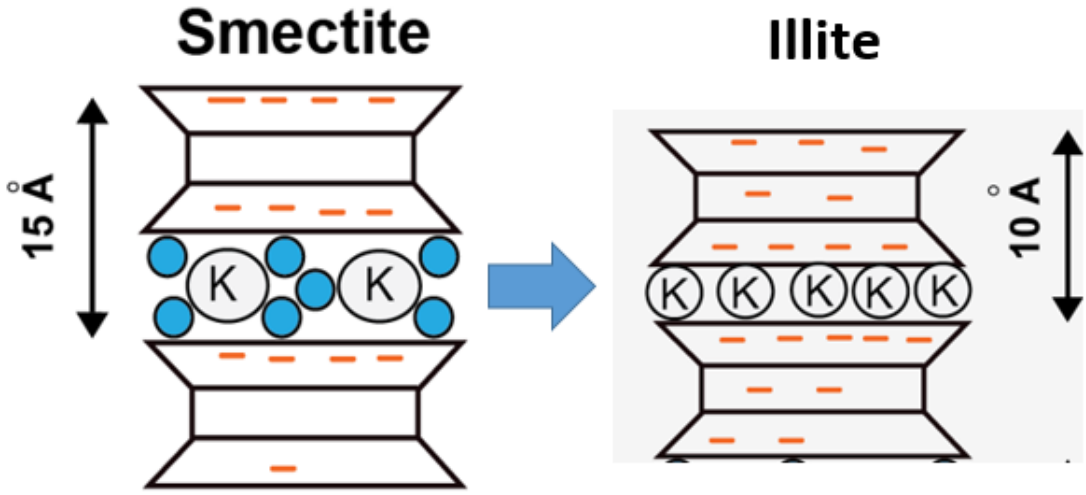

Figure 7-5: The D-spacing Change of the Smectite. The interlayer space reduces from 15 Å to 10 Å; the bound water releases to pore space.

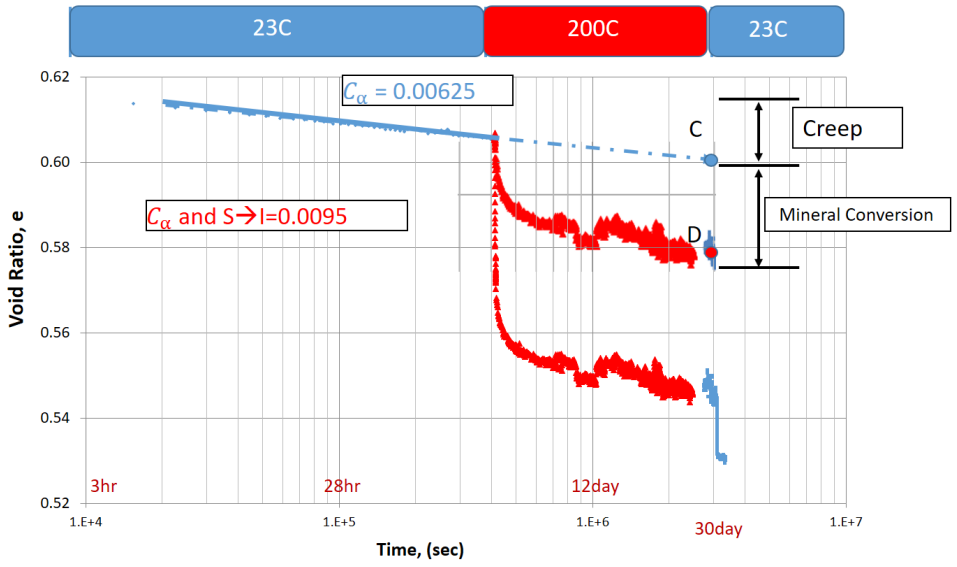

Figure 7-6: Procedures for Calculating Void Ratios for Blue Dot and Red Dot

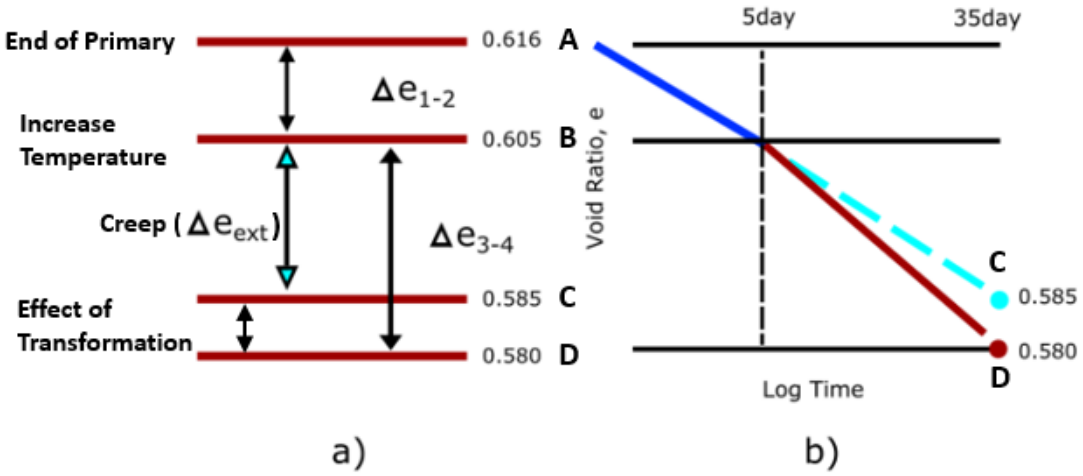

Figure 7-7: Schematics for Void Ratio Calculation

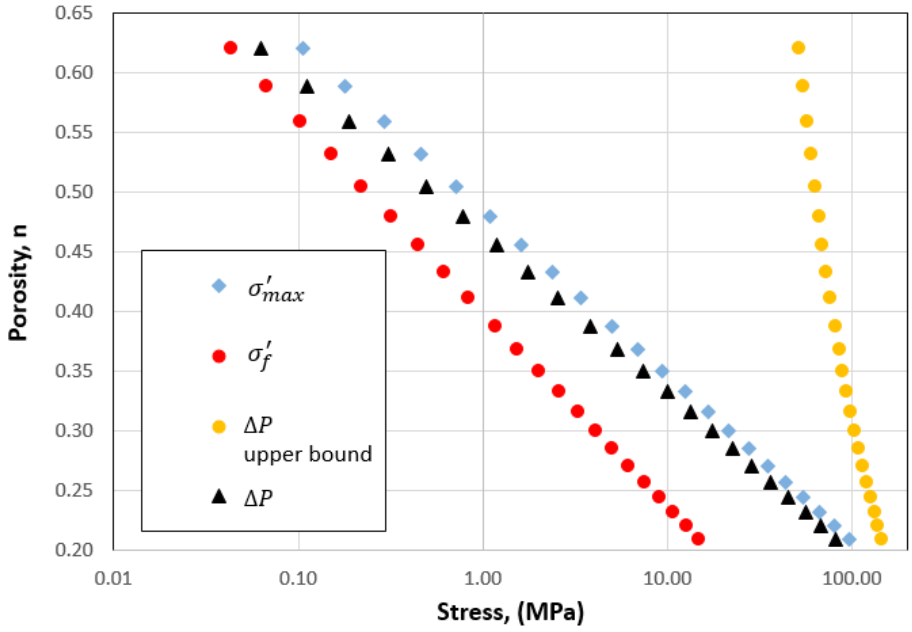

Figure 7-8: Overpressure Model: Porosity vs. Stress. The blue diamonds are the σ'_{max}, the red dots are the reduced effective stress due to overpressure, orange dots are the upper bound for overpressure, the black triangles are the overpressure for the undrained system. Predictions are for c = 20%.

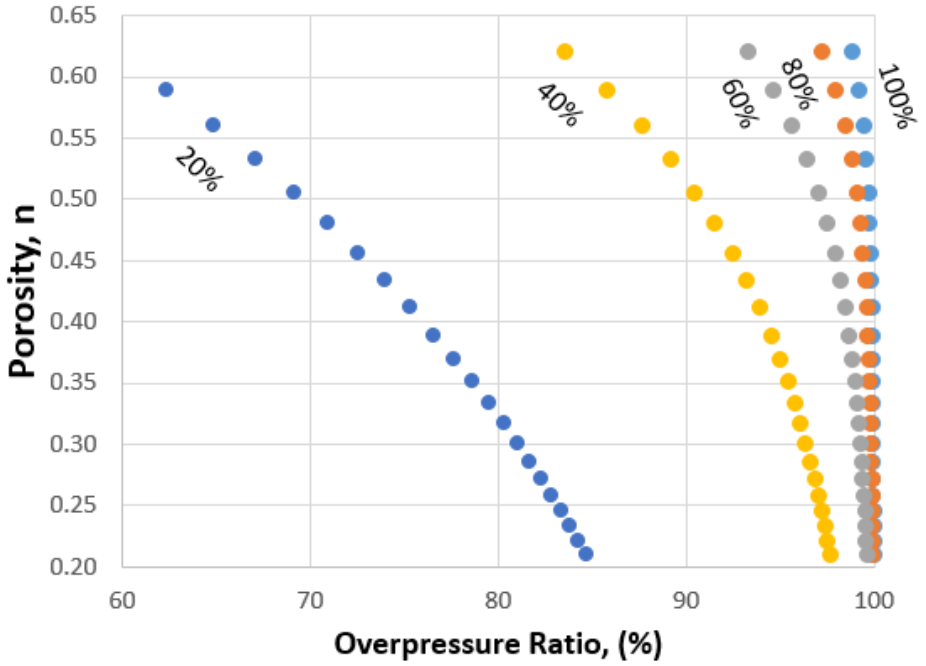

Figure 7-9: Porosity vs. Overpressure Ratio with Different Degree of Illitization. The percentage label besides each overpressure ratio curve represents the percentage of conversion.

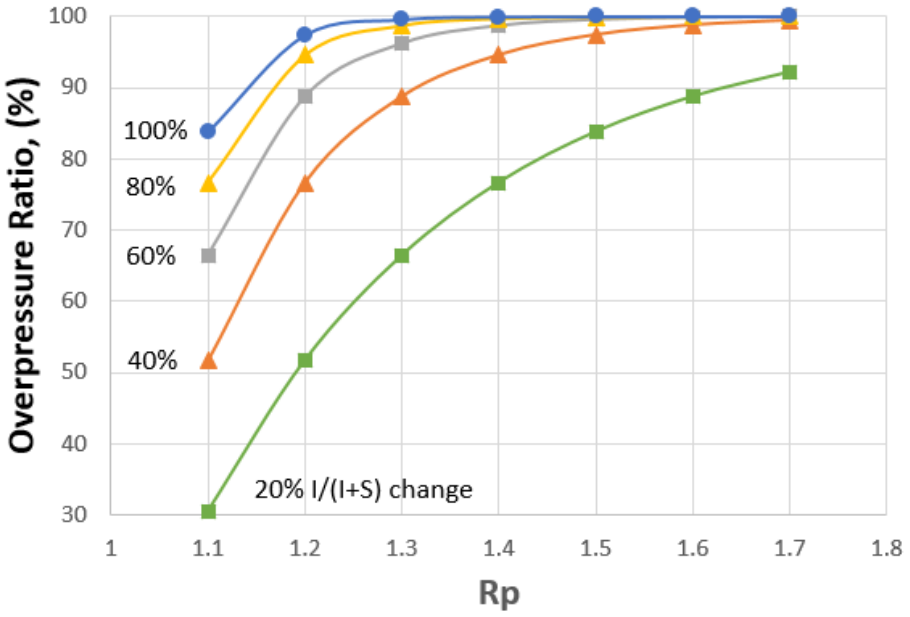

Figure 7-10: Overpressure Ratio vs. Rp with Different Degree of Illitization at 5 MPa effective stress. The percentage label besides each overpressure ratio curve represents the percentage of conversion.

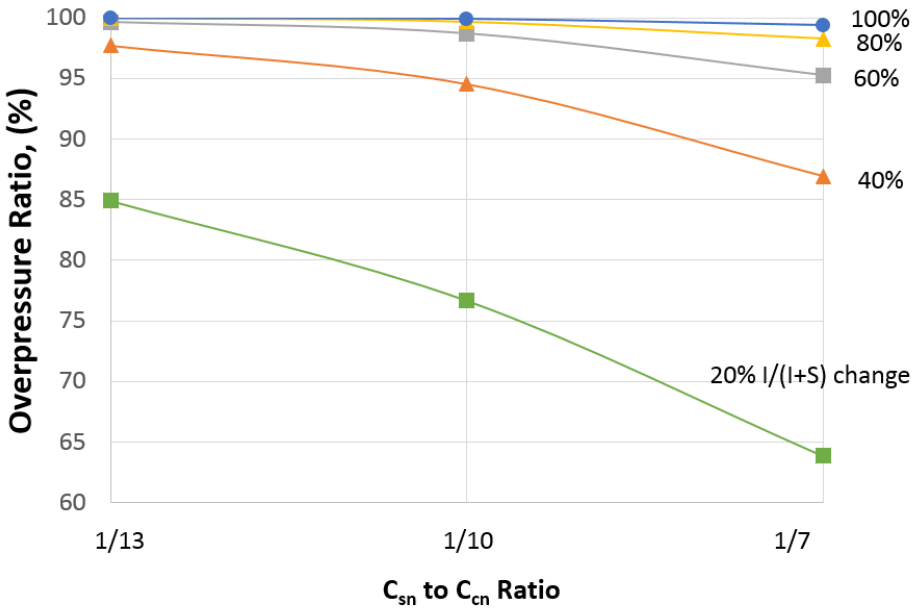

Figure 7-11: Overpressure Ratio vs. C_{sn} to C_{cn} Ratio with Different Degree of Illitization at 5 MPa effective stress. The percentage label besides each overpressure ratio curve represents the percentage of conversion.

THIS PAGE INTENTIONALLY LEFT BLANK

Chapter 8

Conclusions and Recommendations

8.1 Key Observations and Developments

This thesis investigates the compressibility and permeability behavior change due to smectite-to-illite transformation. Two major challenges in terms of hardware and control strategy were overcome: 1. compressing high plasticity mudrock to 100 MPa; 2. inducing mineral transformation using two different methods.

From the previous studies in the author's lab, when dealing with high plasticity material, the excess pore pressure generated during the test, not only exerts a huge pressure gradient on the specimen, but also often reaches the pressure capacity of the CRS device. A combined control method is developed and optimized to compress high plasticity material to 100 MPa. The control algorithm starts with constant rate of strain control and then switches to constant pore pressure control.

Uniaxial compression testing was performed on potassium saturated smectitic and illitic mudrocks. The original Gulf of Mexico - Eugene Island (GoM-EI) mudrock sets the baseline for smectitic mudrock in order to compare with illitic mudrocks.

Two methods were used to create illitic mudrock from the GoM-EI sediment. The illitic mudrock A was created by cooking in a high temperature constant rate of strain (CRS) device with effective stress applied (200 °C and 30 days); the illitic mudrock B was created by cooking in a hydrothermal cooker in a slurry state (250 °C and 18 days). Although the methods of inducing S-I transformation are different, similar

degrees of illitization for the illitic mudrock A and B was achieved by selecting the appropriate temperature and time combination.

In this thesis, the XRD pattern of the smectitic and illitic mudrocks were analyzed using the probability research on disordered lamerllar structures by Drits and Tchoubar (2012). This method fits the theoretical XRD pattern to the measured XRD pattern by optimizing the structure parameters of each clay mineral phase and the weight fraction of each phase. From the mineralogy analysis, the discrete smectite in the illitic mudrock A and B decreases from 43% to zero; the illite content in both illitic mudrocks increases significantly. While the I/S increases from 31% to 66.4% and 85% respectively. The discrete illite phase in the illitic mudrock A increases from 13% to 30%.

The SEM images of the smectitic mudrock and the illitic mudrocks were taken for highly compressed mudrocks. The samples were oven dried then ion milled for fabric analysis. All three mudrocks are compressed to the same gravimetric porosity. The illitic mudrocks have more visible pore space. According to Deirieh (2016), the SEM porosity of smectitic mudrock reveals only 40-54% of the oven dried lab porosity. The reminder of the gravimetric porosity is invisible under the resolution of SEM. During the transformation, the interlayer pore space which is under the resolution of SEM collapses and more pore space is visible to the SEM.

The mineral transformation does not greatly alter the compressibility of the mudrocks. However, the illitic mudrock B sits higher in porosity space than the smectitic mudrock at low stress level. As effective stress increases, the illitic mudrock B reverses order with the smectitic mudrock at 30 MPa. The illitic mudrock A develops an increased preconsolidation stress due to extensive secondary compression and mineral transformation. The preconsolidation stress increases by 2.7 MPa over the effect of mechanical compression. As effective stress increases, the illitic mudrock A converges with the smectitic mudrock.

The compression behavior observed in this research suggests the illitic mudrock will converge with the virgin consolidation line of the smectitic mudrock once the stress goes beyond the quasi-preconsolidation stress in a free draining system. This is

contrary to the traditional S-I transition model. According to Lahann's (2011) model, the illitic line is lower in porosity than the smectitic line at any given effective stress.

The permeability of the smectitic mudrock ranges over five orders from 10^{-16} to 10^{-20} m^2 from a porosity of 0.58 to 0.23. The permeability of the mudrocks are greatly increased by the mineral transformation. The permeability ratio of the illitic mudrocks over the smectitic mudrock increases from 2 to 12 as porosity decreases. The viscosity of the interlayer water or bound water is greater than that of free pore water (Low, 1976), when the bound water in the smectitic mudrock collapses and translates into pore water, the fluid has less drag when flows through the bulk pore space comparing with flowing through the interlayer space, therefore the permeability of the mudrock increases after the transformation.

The creep rate (C_α) at room temperature and elevated temperature were measured during the transformation stage of the illitic mudrock A. C_α at elevated temperature increases by 50 % compared with that at room temperature. The increase in the creep rate is caused by a combination of temperature effect, mineral transformation and dissolution-precipitation of quartz. According to Mesri and Castro (1987), the C_α/C_c ratio is around 0.04 for low stress level and high plasticity soil, the C_α/C_c ratio measured at 5 MPa and room temperature is 0.016. This number is much lower than Mesri and Castro's (1987) observation. The C_α/C_c ratio is stress level dependent. The constant ratio at low stress level might not be valid under the geological conditions of high stress and very slow consolidation rates.

8.2 Modeling the Impact of Illitization

The effect of illitization is different under different boundary conditions. In a free draining system where the expulsion of pore water is not limited by the low permeability of the mudrock, the system does not generate overpressure.

In a low permeability system, two cases are discussed in this thesis. Both cases considers the porosity and the degree of transformation.

In a constant volume system, where the deformation is fixed, the overpressure

calculated from the model due to the fluid expansion of the bound water exceeds the fracture pressure at any given porosity. The calculated overpressure in this situation results in zero effective stress.

In a more realistic undrained system, the system is able to swell due to the reduction of the effective stress. The calculated overpressure ratio increases from 60% to 85% from a porosity of 0.63 to 0.20 when I/(I+S) is 20%. At 100% I/(I+S), the overpressure ratio from the model increases from 98% to 100% from a porosity of 0.63 to 0.20. Increasing the degree of transformation, the entire overpressure ratio vs. porosity curve shifts. The offset gaps between each curve are not equally distanced due to the non linearity introduced by the mudrock swelling curve.

8.3 Recommendations for Future Work

- It is still unclear how big a difference that effective stress exerts on the illite particle growth. This question can be answered by conducting a comparative experiments. We should cook the original GoM-EI mudrock in a hydrothermal cooker under the exact conditions as cooking the illitic mudrock A. The SSA value on the slurry sample will indicates the clay particle size.
- The research presented in this thesis was conducted in a much higher temperature than the in situ temperature (70-120 °) in the basin. The S-I transition is a temperature driven reaction. At an elevated temperature, the transformation has much faster reaction rate. A faster reaction rate guarantees mineralogy change in a short period of time, but the texture and fabric of the laboratory made mudrock might be different from what is created in a geological time. A lower temperature (150 °) and longer time test is suggested to simulate the diagenesis conditions that are closer to the geological setting.
- Karlrez O-rings are used in the high temperature CRS device to seal the fluid in high temperature and high salinity environment. Although Karlrez O-rings survived 30 days of extreme conditions, they leaked when temperature dropped to room temperature. The heating-cooling cycle thermally sets the O-ring to

the geometry of the groove. The geometry of circular cross section becomes rectangular, thus the squeeze ratio becomes zero. Then the device needs to be disassembled to replace the O-ring. To avoid sample disturbance and sample deformation measurement error which could be introduced during the replacement of O-ring, the design of the high temperature should be totally different. From the very beginning, we should design an active cooling system that circulates coolant to reduce the local temperature around the seal. With the advancement of 3D metal printing technology, we can design a tunnel inside the cell allowing coolant to reduce the temperature of target area locally.

- The overpressure model assumes the system never drains, thus generates huge overpressure ratio. It is more reasonable to combine this model with partial drainage, relaxation and creep.

THIS PAGE INTENTIONALLY LEFT BLANK

References

Bétard, F., Caner, L., Gunnell, Y., & Bourgeon, G. (2009). Illite neoformation in plagioclase during weathering: evidence from semi-arid northeast brazil. *Geoderma*, *152*(1-2), 53–62.

Bjølykke, K. (1998). Clay mineral diagenesis in sedimentary basinsâĂŤa key to the prediction of rock properties. examples from the north sea basin. *Clay minerals*, *33*(1), 15–34.

Boles, J. R., & Franks, S. G. (1979). Clay diagenesis in wilcox sandstones of southwest texas: implications of smectite diagenesis on sandstone cementation. *Journal of Sedimentary Research*, *49*(1).

Bowers, G. L. (2011). Elastic vs inelastic unloading during smectite/illite genesis-a geomechanics perspective. In *Geopressure*.

Burland, J. (1990). On the compressibility and shear strength of natural clays. *Géotechnique*, *40*(3), 329–378.

Carman, P. C. (1956). *Flow of gases through porous media*. Academic press.

Cerato, A. B., & Lutenegger, A. J. (2002). Determination of surface area of fine-grained soils by the ethylene glycol monoethyl ether (egme) method. *Geotechnical Testing Journal*, *25*(3), 315–321.

Day-Stirrat, R. J., Aplin, A. C., Środoń, J., & Van der Pluijm, B. A. (2008). Diagenetic reorientation of phyllosilicate minerals in paleogene mudstones of the podhale basin, southern poland. *Clays and Clay Minerals*, *56*(1), 100–111.

Day-Stirrat, R. J., Schleicher, A. M., Schneider, J., Flemings, P. B., Germaine, J. T., & van der Pluijm, B. A. (2011). Preferred orientation of phyllosilicates: Effects of composition and stress on resedimented mudstone microfabrics. *Journal of Structural Geology*, *33*(9), 1347–1358.

Drits, V. A., & Tchoubar, C. (2012). *X-ray diffraction by disordered lamellar structures: Theory and applications to microdivided silicates and carbons*. Springer Science & Business Media.

Duffy, L. M. (2011). *Compaction mechanisms in mudstones and shales: Implications from the laboratory and nature* (Unpublished doctoral dissertation). Newcastle University, Newcastle, England.

Eberl, D. D. (1980). Alkali cation selectivity and fixation by clay minerals. *CLAYS CLAY MINER. Clays Clay Miner.*, *28*(3), 161.

England, W., Mackenzie, A., Mann, D., & Quigley, T. (1987). The movement and entrapment of petroleum fluids in the subsurface. *Journal of the Geological Society*, *144*(2), 327–347.

Ferrage, E., Vidal, O., Mosser-Ruck, R., Cathelineau, M., & Cuadros, J. (2011). A reinvestigation of smectite illitization in experimental hydrothermal conditions: Results from x-ray diffraction and transmission electron microscopy. *American Mineralogist*, *96*(1), 207–223.

Fitts, T. G., & Brown, K. M. (1999). Stress-induced smectite dehydration: ramifications for patterns of freshening and fluid expulsion in the n. barbados accretionary wedge. *Earth and Planetary Science Letters*, *172*(1-2), 179–197.

Ge, C. (2016). *Smectite to illite transformation of gulf of mexico -eugene island (gom-ei) mudrock* (Unpublished master's thesis). MIT, Cambridge, MA.

Germaine, J. T., & Germaine, A. V. (2009). *Geotechnical laboratory measurements for engineers*. John Wiley & Sons.

Goulty, N., Sargent, C., Andras, P., & Aplin, A. (2016). Compaction of diagenetically altered mudstones–part 1: Mechanical and chemical contributions. *Marine and Petroleum Geology*, *77*, 703–713.

Hart, B., Flemings, P., & Deshpande, A. (1995). Porosity and pressure: Role of compaction disequilibrium in the development of geopressures in a gulf coast pleistocene basin. *Geology*, *23*(1), 45–48.

Hillier, S. (2003). Quantitative analysis of clay and other minerals in sandstones by x-ray powder diffraction (xrpd). *International Association of Sedimentologists Special Publication*, *34*, 213–251.

Ho, N.-C., Peacor, D. R., & Van der Pluijm, B. A. (1999). Preferred orientation of phyllosilicates in gulf coast mudstones and relation to the smectite-illite transition. *Clays and Clay Minerals*, *47*(4), 495–504.

Hower, J., Eslinger, E. V., Hower, M. E., & Perry, E. A. (1976). Mechanism of burial metamorphism of argillaceous sediment: 1. mineralogical and chemical evidence. *Geological Society of America Bulletin*, *87*(5), 725–737.

Huang, W.-L., Longo, J. M., & Pevear, D. R. (1993). An experimentally derived kinetic model for smectite-to-illite conversion and its use as a geothermometer. *Clays and Clay Minerals*, *41*, 162–162.

Karig, D., & Ask, M. (2003). Geological perspectives on consolidation of clay-rich marine sediments. *Journal of Geophysical Research: Solid Earth*, *108*(B4).

Ladd, C. (1991). The twenty-second terzaghi lecture..

Lahann, R. (2002). Impact of smectite diagenesis on compaction modeling and compaction equilibrium. *MEMOIRS-AMERICAN ASSOCIATION OF PETROLEUM GEOLOGISTS*, 61–72.

Lambe, T. W., & Whitman, R. V. (2008). *Soil mechanics si version*. John Wiley & Sons.

Losh, S., Eglinton, L., Schoell, M., & Wood, J. (1999). Vertical and lateral fluid flow related to a large growth fault, south eugene island block 330 field, offshore louisiana. *AAPG bulletin*, *83*(2), 244–276.

Low, P. F. (1976). Viscosity of interlayer water in montmorillonite 1. *Soil Science Society of America Journal*, *40*(4), 500–505.

Lowe, J., Jonas, E., & Obrican, V. (1969). Controlled gradient consolidation test. *Journal of Soil Mechanics & Foundations Div*, *92*(SM5, Proc Paper 490).

Meade, R. H. (1963). Factors influencing the pore volume of fine-grained sediments under low-to-moderate overburden loads 1. *Sedimentology*, *2*(3), 235–242.

Meade, R. H. (1966). Factors influencing early stages of compaction of clays and sands–review. *AAPG Bulletin*, *50*(3), 626–627.

Mesri, G. (1971). Mechanisms controlling the permeability of clays. *Clays and Clay Minerals*, *19*, 151–158.

Mesri, G., & Castro, A. (1987). C α/c c concept and k 0 during secondary compression. *Journal of Geotechnical Engineering*, *113*(3), 230–247.

Meunier, A., & Velde, B. D. (2013). *Illite: Origins, evolution and metamorphism*. Springer Science & Business Media.

Mitchell, J. K., Soga, K., et al. (2005). *Fundamentals of soil behavior* (Vol. 3). John Wiley & Sons New York.

Mondol, N. H., Bjørlykke, K., Jahren, J., & Høeg, K. (2007). Experimental mechanical compaction of clay mineral aggregatesâĂŤchanges in physical properties of mudstones during burial. *Marine and Petroleum Geology*, *24*(5), 289–311.

Montoya, J., & Hemley, J. (1975). Activity relations and stabilities in alkali feldspar and mica alteration reactions. *Economic Geology*, *70*(3), 577–583.

Moore, D. M., & Reynolds, R. C. (1989). *X-ray diffraction and the identification and analysis of clay minerals* (Vol. 378). Oxford university press Oxford.

Nadeau, Wilson, M., McHardy, W., & Tait, J. (1985). The conversion of smectite to illite during diagenesis: evidence from some illitic clays from bentonites and sandstones. *Mineralogical Magazine*, *49*(352), 393–400.

Nadeau, P. (2005). *Distribution of hydrocarbons in sedimentary basins*. Statoil Oil.

Pevear, D. (1992). Illite age analysis, a new tool for basin thermal history analysis. *Water-Rock Interaction. Balkema, Rotterdam*, 1251–1254.

Pinkston, F. W. M. (2017). *Pore pressure and stress at the macondo well, mississippi canyon, gulf of mexico* (Unpublished master's thesis). University of Texas at Austin, Austin, TX.

Powers, M. C. (1967). Fluid-release mechanisms in compacting marine mudrocks and their importance in oil exploration. *AAPG bulletin*, *51*(7), 1240–1254.

Pytte, A., & Reynolds, R. (1989). The thermal transformation of smectite to illite. In *Thermal history of sedimentary basins* (pp. 133–140). Springer.

Santamarina, J., Klein, K., Wang, Y., & Prencke, E. (2002). Specific surface: determination and relevance. *Canadian Geotechnical Journal*, *39*(1), 233–241.

Środoń, J., & MaCarty, D. K. (2008). Surface area and layer charge of smectite from cec and egme/h2o-retention measurements. *Clays and clay minerals*, *56*(2), 155–174.

Swarbrick, R. E., Osborne, M. J., & Yardley, G. S. (2001). Aapg memoir 76, chapter 1: Comparision of overpressure magnitude resulting from the main generating mechanisms.

Warbrick, R., & Osborne, M. (1998). Mechanisms that generate abnormal pressure: an overview. *Abnormal Pressure in Hydrocarbon Environments*, *70*, 13–43.

Wissa, A. (1971). Consolidation at constant rate of strain. *Journal of Soil Mechanics & Foundations Div*.

Wolf, A., Brown, M., & Prentiss, P. (1975). 1976. concentrative properties of aqueous solutions: conversion tables. *Handbook of Chemistry and Physics. RC Weast, editor. CRC Press, Cleveland, Ohio. D-218-D-272*.

Appendix A

KCl Salt Mixing Guide

This appendix lists the needed mass of KCl salt and mass of water for different salinity at 24 °C. In the Excel sheet, user can input the water temperature measured at the time of operation to update the mass of KCl salt and mass of water.

Table A.1: KCl Potatssium Chloride Solution Mixing Guide

Salt Concentration	Salt Concentration	Effective Density of Salt	Density of Salt Water at 20 °C	Mass of Water
mol/L	g/L	g/cm3	g/cm3	g
1	74.50	2.538	1.043	968.03
2	149.00	2.536	1.088	938.70
3	223.50	2.483	1.131	907.53
4	298.00	2.380	1.170	872.42
5	372.50	2.226	1.203	830.42

THIS PAGE INTENTIONALLY LEFT BLANK

Appendix B

Reduction File

This appendix includes the Matlab® codes for the main reduction function for analyzing CRS test data, smoothing function for reducing noisy data, permeability function for calculating permeability using Wissa's linear theory with no regression and permeability function with regression.

Comparing the permeability results calculated with regression and without regression, the difference is negligible.

The files required to run this program include:

1. a CRS file storing the data in engineering units in the format of: time in second in first column, displacement of specimen in cm in second column, vertial load in kg in third column, cell and pore pressure in ksc in forth and fifth column.
2. Smooth Function
3. Permeability Function

The output matrix R includes the calculated values for time in sec, strain in %, total vertical stress in ksc, pore pressure in ksc, cell pressure in ksc, vertical effective stress in ksc, void ratio, excess pore pressure in ksc, permeability in cm/s, coefficient of consolidation in cm^2/s, appratus compressibility in cm.

THIS PAGE INTENTIONALLY LEFT BLANK

Listings

B.1 Main Reduction Function 173
B.2 Smooth Function 177
B.3 Permeability Function 178
B.4 Permeability Function with Regression 179

Listing B.1: Main Reduction Function

```
% need CRSxxxxr.dat file
% Perm1.m
% PerReg.m
% smooth.m
% if got error message try increase Trim to 1

clear;
global AP WP D E INTER acc Refforce RefDefl INC nr nwin HINIT
INC = 1; % 1 percent moving window
nwin = 3; % smoothing PP averaging over 3
Trim = 0.8; %tricate 0.8 strain
HS = 0.524; %CM CRS1531

AREA = 9.94; %cm^2; area of sample
HINIT = 1.27; %cm; height of sample
%==========Apparatue Compressibility Parameter===============

```

```
%HighTemp CRS cell
AP = 7.9; %cm^2; area of piston from measured
WP = 2.26; %kg; weight of piston from area correction HighTemp
D = 0.00022;
E = 0.470114;
INTER = 0;
acc = 0;
fri = 4.5; %kg piston friction
sload = 1.8; % seating load before pressure up in kg
Refforce = sload + WP;
RefDefl = D*Refforce^E+INTER;

%=================== get data ========================
prompt = 'Enter file name:';
str = input(prompt,'s');
V=dlmread(str);

nr = size(V,1); % number of rows
time = V(:,1);% sec
disp = V(:,2);% cm
load = V(:,3)-fri;% kg
CP = V(:,4);% ksc
PP = V(:,5);% ksc

PPavg = smooth(PP); %average the pore pressure
CPavg = smooth(CP); %average the cell pressure
PP = PPavg;
CP = CPavg;

%==================STRESS& STRAIN==========================
```

```
for i = 1: nr
    nforce(i,1) = load(i,1)-CP(i,1)*AP + WP;% correction for CP
    adefl(i,1) = AppComp(nforce(i,1)); %deflection of the device
    tdefl(i,1) = adefl(i,1)- RefDefl;
    strain(i,1) = (disp(i,1)  - tdefl(i,1)) /HINIT *100 ;% in %
    stress(i,1) = nforce(i,1)/AREA; %vertical total stress

    e(i,1) = (HINIT - strain(i,1)*HINIT/100-HS)/HS; %void ratio
    U(i,1) = PP(i,1) -CP(i,1); % excess base pore pressure
        if U(i,1) < 0
           U(i,1) = 0 ; % if there is negative excess pore pressure
        end
    ES(i,1) = stress(i,1) - (2/3)*U(i,1); % effective stress
end

%========DETERMIN BEGINNING AND ENDING POINTS===============
StrainMin = min(strain);
BEGIN = sum(strain-StrainMin<Trim);
StrainMax = max(strain);
ND = sum((StrainMax-strain)>Trim);
% this section determines the begin data and end data of regression
   analysis


window = ones(nr,2);
ws = 8; % half of the window size
for i = BEGIN : ND

     STRT(i,1) = i - ws;
     if STRT(i,1) <1
```

```
77          STRT(i,1) = 1;
78      end
79
80      FINISH(i,1) = i+ ws;
81      if FINISH(i,1) > nr
82          FINISH(i,1) = nr;
83      end
84      window(i,1:2) = horzcat(STRT(i,1), FINISH(i,1));
85  end
86  % ======================= checks ============================
87  Sl = stress(BEGIN,1);
88  UL = U(BEGIN,1);
89  F = ((stress-Sl)-(U-UL))./(stress-Sl); % should be bigger than 0.4 for
90                                         % steady state
91  % ===================Perm Calculation================
92  H1 = (100-strain)/100*HINIT; % the sample height
93  [K,CV] = Perm1(window,time,strain,stress,U,e,H1); % no regression
94  [KReg,CVREG] = PermReg(window,time,strain,stress,U,e,H1); % with
        regression
95  R = horzcat(time,strain,stress,PP,CP,ES,e,U,K,CV,tdefl);
96  ESMPA = ES*0.09807; % vertical effective stress in MPa
97
98  %======================PLOTTING================================
99  figure;
100 sz = 20; % size of marker
101 scatter(ESMPA,e,sz,'.')
102 set(gca,'xscale','log')
103 xlabel('Vertical Effective Stress, \sigma_v '' MPa')
104 ylabel('Void ratio')
105 grid on
```

```
106
107 figure;
108 scatter(e,K,10,'.');
109 set(gca,'yscale','log')
110 xlabel('Void Ratio')
111 ylabel('Permeability, cm/s')
112 grid on
113 hold on
114 scatter(e,KReg,10,'*');
115
116 %save('CRS_Combined','TCRS010_100MPa','-append') % add new data to MAT
      file
```

Listing B.2: Smooth Function

```
1  function y = smooth(x)
2  global nwin nr
3   deln = (nwin -1)/2;
4   y = nan(nr,1);
5      for i = 1+deln : nr -deln
6          sumx = 0;
7          for j = i -deln : i+deln
8              sumx = sumx + x(j,1);
9          end
10         y(i,1) = sumx/nwin;
11     end
12     y(1,1) = x(1,1);
13     y(nr,1) = x(nr,1);
14 end
```

Listing B.3: Permeability Function

```
function  [K,CV] = Perm1(window,time,strain,stress,U,e,H1)
    global HINIT nr
    dt = nan(nr,1);
    dt = time(window(:,2))-time(window(:,1)); %in sec

    dstrain = nan(nr,1);
    dstrain = strain(window(:,2))-strain(window(:,1));%in %

    dstress = nan(nr,1);
    dstress = stress(window(:,2)) - stress(window(:,1));

    rate = dstrain./dt;

    rate(dt==0) = 0;

    K11 = rate./U;
    K12 = K11.*H1;
    K12(isnan(K11)|isinf(K11)) = 0;

    K = K12*HINIT/2/100/1000; % in cm/s

    mv = (rate.*dt)./dstress;
    CV = K./mv*100*1000;
    CV(mv==0) = 0;
end
```

Listing B.4: Permeability Function with Regression

```
function [K,Cv] = PermReg(window,time,strain,stress,U,e,H1)
    global HINIT nr
    K = 0;
    Cv = 0;

    sumTi = zeros(nr,1);
    for i = 1:nr
        TiZone(i,1:17) = time(window(i,1):window(i,2))';
        StrainZone(i,1:17)= strain(window(i,1):window(i,2))';
        StressZone(i,1:17)= stress(window(i,1):window(i,2))';
    end

    sumTi = sum(TiZone,2); % sum the secs in each window
    sumStrain = sum(StrainZone,2);
    sumStress = sum(StressZone,2);

    sumTi2 = sum(TiZone.*TiZone,2);
    sumTiStrain = sum(TiZone.*StrainZone,2);
    sumTiStress = sum(TiZone.*StressZone,2);

    avgTi = mean(TiZone,2);
    avgStrain = mean(StrainZone,2);
    avgStress = mean(StressZone,2);

    BETAE = (sumTiStrain - 17*avgTi.*avgStrain)./(sumTi2-17*avgTi.^2);
    %BETAVS = (SUMTIVSI - WR*AVGTI*AVGVSI)/(SUMTI2-WR*AVGTI^2);

    K11 = BETAE./U;
    K12 = K11.*H1;
```

```
30      K12(isnan(K11)|isinf(K11)) = 0;
31
32      K = K12*HINIT/2/100/1000; % in cm/s
33      CV=0;   % CV in regression work doesn't really work
34
35
36  end
```